

ANALYSIS OF DIELECTRIC INTEGRATED GUIDE BASED STRUCTURES FOR MILLIMETER WAVE AND OPTICAL FREQUENCY

A DISSERTATION

*Submitted in partial fulfillment of the
requirements for the award of the degree*

of

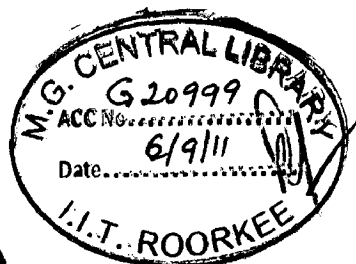
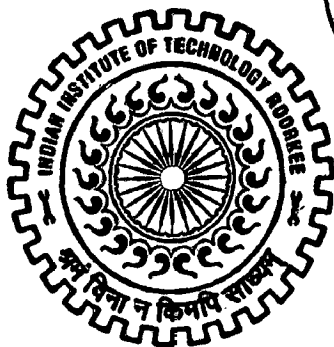
MASTER OF TECHNOLOGY

in

ELECTRONICS AND COMMUNICATION ENGINEERING
(With Specialization in RF and Microwave Engineering)

By

FAIZ AHMED SIDDIQUI



DEPARTMENT OF ELECTRONICS AND COMPUTER ENGINEERING
INDIAN INSTITUTE OF TECHNOLOGY ROORKEE
ROORKEE - 247 667 (INDIA)

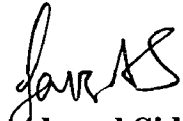
JUNE, 2011

Candidate's Declaration

I hereby declare that the work, which is being presented in the dissertation entitled, "*Analysis of Dielectric Integrated Guide Based Structures for Millimeter Wave and Optical Frequency*", and submitted for partial fulfillment of the requirements for the award of degree of *Master of Technology* in *RF & Microwave Engineering*, submitted in the Department of Electronics and Computer Engineering, *Indian Institute of Technology*, Roorkee (INDIA), is an authentic record of my own work carried out under the supervision of **Dr. N. P. Pathak**, Assistant Professor, Department of Electronics and Computer Engineering, Indian Institute of Technology, Roorkee.

I have not submitted the matter embodied in this dissertation for the award of any other qualification.

Date: 30th day of June in the year 2011.


(Faiz Ahmed Siddiqui)

Place: Roorkee

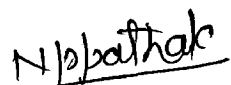
Enrol. No: 09533004

Supervisor's Certificate

This is to certify that dissertation entitled, "*Analysis of Dielectric Integrated Guide Based Structures for Millimeter Wave and Optical Frequency*", which has been submitted by Faiz Ahmed Siddiqui is record of his own work carried out by him under my supervision. I also certify that the above statement made by the candidates is correct to the best of my knowledge and belief.

Date: 30th day of June in the year 2011.

Place: Roorkee


(Dr. N.P. PATHAK)
Assistant Professor
E&CE Department
IIT – Roorkee
Uttaranchal – 247667

Acknowledgements

It is my pleasure to acknowledge those who supported me during my stay at IIT Roorkee.

To get started, first vote of thanks goes to my advisor Dr. N. P. Pathak for giving me the chance to work in my field of interest and constant support throughout my dissertation work. His enthusiasm in the colourful optics field has made difficult looking results, easy. His keen interest for analyzing our results helped me in gaining technical insight into the processes and implementing the changes as per the discussion. I express my deepest gratitude to him for his valuable guidance, support and motivation in my work.

Next, thanks to our Head of the Department, Electronics and Computer Engineering, Prof. S.N. Sinha for having some of the basic discussions with him and thereby gaining answers for some of the twisted questions, which seems to me.

I also want to thank all other respected professors for their technical and non technical guidance during my work.

I thank Mr. S. K. Gaur, Mr. Rajaram and Mr. Giri for their handy support and guidance during my work.

I also thank the whole of the department for arranging the necessary facilities, both technical and household facilities, to safely carry out our dissertation work.

During my stay here I was surround by colleagues from either different or same department. I take this, the only, opportunity to thank them for motivating me when I was in stormy phase of my stay, here. I thank my lab PhD scholars for having some of the intelligent and "beyond scope" discussion and their kind support for completing this report on time. They always motivated me whenever I encountered any technical blockage. I am indebted for their kind assistance in my technical issues and *dedicated hard work* for grooming up this report. I thank my batch mates for giving me the required help in no possible time and having great fun, arranging some of the adventurous trips.

At last, I must thank my family for being supportive and encouraging throughout my stay here.

Faiz Ahmed Siddiqui
Enroll. No: 09533004

This report investigates properties of transmission lines, which are applicable at millimeter wave and optical frequencies. In general, such wave guiding structures consist of a dielectric layer that is sandwiched between metallic plates. Two of the prominent examples include the non-radiative dielectric (NRD) guide and the slot waveguide.

An NRD guide presents various attractive features, like, ease of fabrication, low transmission loss, and suppression of radiation at bends and discontinuities. Hence, it is imperative to implement integrated transition from NRD guide to standard rectangular waveguide, like, WR28. This is because such transitions will be instrumental in successful development of novel front-end components for millimeter-wave applications that are based on NRD guide technology.

Additionally, in optical frequency regime, a metal-dielectric interface supports small propagation lengths and localized effect waves (surface plasmons or surface plasmon polaritons, SPP). Plasmonics is a field of photonics, wherein, the flow of light can be molded using metallic nanostructures. The concepts of plasmonics have widespread potential use in several important technological applications, like, optical microscopy, solar cells, efficient solid state light sources, *etc.*

The current work demonstrates design of an NRD guide-to-WR28 transition, whose characteristics are studied using finite element method (FEM) based solver. The achieved results exhibit 1- to 2-dB insertion loss in the desired band. Moreover, design of stepped impedance resonator (SIR) based band pass filter (BPF) and band stop filter (BSF) operating at 28 GHz are undertaken. The BPF exhibits an insertion loss of around 2.5-dB, while, the BSF presents an approximate pass band return loss of 1-dB.

Furthermore, a slot geometry is examined, modelling its conducting material as drude metal, so as to analyze its effect on propagation characteristics and electromagnetic (EM) fields of the slot structure. 3D EM solvers have been used to obtain field patterns of different propagating modes, their respective propagation constants and guided wavelengths. Besides it, the dispersion diagram and the field plots of the slot waveguide structure are reproduced using finite integration technique (FIT) based solver. The achieved response closely match the results reported in open literatures.

<i>Candidate's Declaration</i>	ii
<i>Acknowledgements</i>	iii
<i>Abstract</i>	iv
Chapter 1 Introduction to Guiding Structures	1
1.1 Evolution of Guiding Structures	1
1.2 NRD Guide Basics	3
1.2.1 Principle of Operation	4
1.2.2 Design Equations for NRD Guide	5
1.2.3 Propagating Modes in NRD Guide	5
1.2.4 Dispersion Bandwidth Characteristics	7
1.2.5 Merits and Demerits of the NRD Guide Technology	7
1.3 NRD Guide Transition - Literature Review	9
1.3.1 NRD Guide Transition to Planar Transmission Media	9
1.3.1.1 Aperture-Coupled Hybrid Integration Scheme	10
1.3.1.2 Co-Layered Hybrid Integration Scheme	11
1.3.1.3 Integration with Suspended Stripline	12
1.3.1.4 Integration with Slotline	13
1.3.2 NRD Guide Transition to 3D Structures - Literature Review	13
1.4 Plasmonics Basics	16
1.4.1 Surface Plasmon-Polaritons (SPP)	16
1.4.2 Surface Plasmon Dispersion	17
1.4.3 Optical Properties of Metals	20
1.5 Plasmonic Slot Waveguide	20
1.5.1 Variants of Plasmonic Slot Waveguide	22
1.5.2 Transmission Model of Surface Plasmon Waveguide (SPWG)	24
1.5.3 Characteristics Impedance Model of SPWG	25
1.5.4 Applications of Plasmonics	25
1.6 Statement of Problem	26
1.7 Organization of this report	27
Chapter 2 NRD Guide Based Millimeter Wave Circuits	29
2.1 Introduction	29
2.1.1 WR28/34-NRD Guide Transition-Geometry of the Setup	29
2.1.2 Simulation setup for WR28/34-NRD guide transition	30
2.1.3 Response of the WR28-NRD Guide Transition	31
2.2 NRD Guide to WR Transition using horn antenna	33
2.2.1 Horn Antenna Design	33
2.2.2 Simulation Setup for NRD Guide to WR Transition using Horn Antenna	35
2.2.3 Response of the NRD Guide to WR Transition using Horn Antenna	35
2.3 Stepped Impedance Resonators (SIR) Basics	36
2.3.1 Characteristics of SIR	37
2.3.1.1 Resonance Condition	38

Table of Contents

2.3.1.2	Spurious Response	38
2.3.1.3	Susceptance Slope Parameter	39
2.3.2	BPF Based on CSIR (Coupled SIR)	39
2.3.3	BSF Based on CSIR	46
2.3.3.1	Spurious Response	46
2.3.3.2	Transmission Pole Response	46
2.3.3.3	Design Procedure of CSIR BSF	47
2.4	Effect of Variation of Spurline Parameters on Filter Response	49
2.5	Conclusion	52
Chapter 3	Slot Plasmonic Waveguide Structures (MIM/MDM)	53
3.1	Introduction	54
3.2	SPP Launching Mechanism	57
3.3	Simulation Results of Plasmonic SWG (SPWG)	57
3.3.1	SPP gap WG excited through I shaped aperture [64]	57
3.3.2	SPP gap WG excited using nano-antenna [66]	61
3.3.3	SPP gap WG excited using broadband pulse[68]	63
3.4	Conclusion	65
Chapter 4	Slot Plasmonic Hybrid Waveguide Structures (M/D1/D2)	67
4.1	Introduction	67
4.2	Simulation results of hybrid slot WG [69]	68
4.3	Simulation results of hybrid WG [69]	72
4.4	Conclusion	76
Chapter 5	Conclusions and Future Scope	77
5.1	Summary and Conclusion of the Work Done	77
5.2	Scope for Further Work	77
	References	78
	Appendix A	83
	Appendix B	87
	Appendix C	88

Chapter 1

Introduction to Guiding Structures

1.1 Evolution of Guiding Structures

The congestion of the RF spectrum due to wireless communications including local area networks (LAN's), and personal communication services (PCS) has generated considerable interest in both microwave and millimeter-wave frequency range. In particular, the millimeter-wave transmission, unlike the microwave characteristics, presents some interesting features for short-haul high speed data links, line-of-sight LAN's, and imaging radar, as well as collision-avoidance sensor applications. These features include frequency reuse, quasi-optical propagation, and high-resolution. However, any successful deployment of a wireless technology at millimeter-wave frequencies that is intended for widespread and extensive commercial applications depends on the availability of a technology having properties such as low cost, compact size, low power consumption, and mechanical rigidity. In addition to these, it is also required that the applied technology offers low-loss signal transmission, which is essential for realizing high Q circuits [1].

Technologies that have been used to date may be divided into two broad classes:

- Planar technology
- Non-Planar technology

The former is often related to the microwave integrated circuit (MIC), miniaturized hybrid microwave integrated circuit (MHMIC), and monolithic microwave integrated circuit (MMIC), while the latter refers more or less to the metallic waveguide, coaxial line, and dielectric waveguide. In view of its advantages and disadvantages, the non-planar technology has been known for its complementariness with respect to its planar counterpart. Obviously, the hybrid scheme based on combined planar and non-planar technology is more appealing. Even though a large class of dielectric waveguides had already been proposed for millimeter-wave and sub-millimeter-wave applications, very little attention was given for the potential integration of a planar structure with a dielectric waveguide. This was probably due to the fact that the fundamental limitation of using a dielectric waveguide lied in its severe radiation loss once circuit bends or discontinuities are encountered, which jeopardized useful

applications of the dielectric waveguide. This perception was held until the invention of a non-radiative dielectric (NRD) waveguide [2].

Stepping further up the RF spectrum ladder we enter a whole new world of excitement and colorfulness where metal stops reflecting and start passing the incident Electro-Magnetic (EM) waves through it. Plasmonics, as researcher call it, is a rapidly evolving subfield of nano-photonics that deals with surface plasmons (SP), which are the collective charge oscillations that occur at the interface between conductive and dielectric materials [3] with EM radiation, Figure 1.01. These collective charge oscillations result in a new mode of EM radiation, part of which is propagating light and another part includes charge-density oscillation. SP have one essential characteristic, which is that the electric field is maximal at the interface along which it propagates and decays away from the interface exponentially into both the conducting and the dielectric media. The localization and the confinement of the field is dependent on the material properties of the conductor and the dielectric layers by which it is bound, and this field profile can be further altered through the imposition of structure on the interface. In the optical range, the field confinement of SP on a metal surface can be considerably less than the wavelength of light in free space at the same frequency.

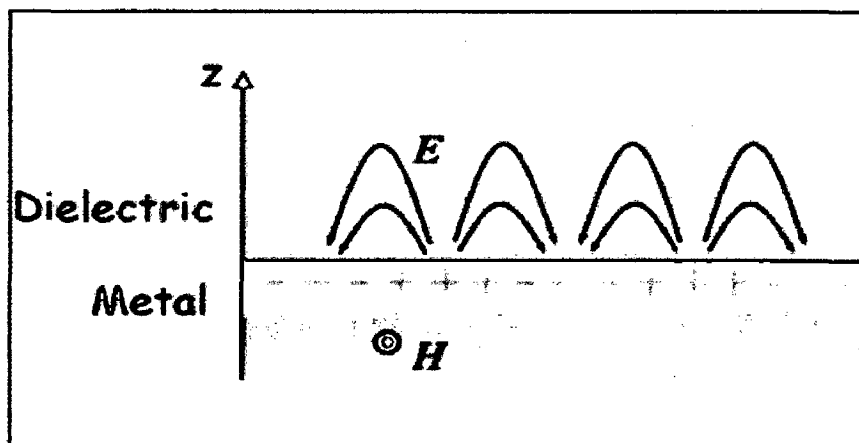


Figure 1.01: Illustrating the plasmon occurrence on interface upon interaction of EM wave and free electrons in metal [4].

The possible applications of plasmonics in any field which would benefit from enhanced control of photons include beam steering to single-molecule bio-detection. In the area of optoelectronics, plasmonics meet demands for optical interconnects which are small

enough to co-exist with nanoscale electronic circuits. Emerging technologies include very small, low-power active devices such as electro-optic or all-optical modulators. Passive plasmonic devices, or “optical antennas,” are being used to enhance the performance of emitters and detectors, and to harvest sunlight for photovoltaic. Resonators made from metal nanostructures can confine concentrated optical energy to tiny regions of space, much smaller than a wavelength of light in free space. Likewise many exotic effects can be achieved with metallic waveguides, such as guiding light at optical frequencies with a tiny, X-ray like wavelength; or even with a negative effective optical index. Even such extraordinary technologies as micro-targeted infrared cancer therapy and “invisibility cloaks” are on the horizon.

Next section discusses the basics, characteristics results and useful formulae pertaining to NRD guide.

1.2 NRD Guide Basics

Non Radiative Dielectric Guide, first designed by Yoneyama and Nishida [5], consists of a rectangular dielectric strip of cross section ($a \times b$) and relative dielectric constant, ϵ_r , which is sandwiched between two parallel metal ground plates, as shown in Figure 1.02. The plates’ separation is less than half the free space wavelength ($\lambda_0/2$) so that the fields are cut-off in the air region. However, the presence of a dielectric strip with proper dielectric constant eliminates the cut-off property and enables electromagnetic waves to propagate freely along the strip whether it be straight or curved.

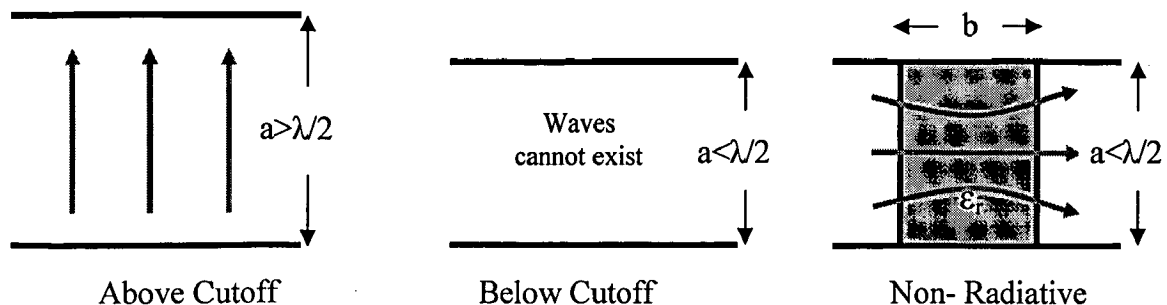


Figure 1.02: Illustrating the NRD guide where 'a' & 'b' are narrow and broad wall dimension, respectively, of a waveguide.

1.2.1 Principle of Operation

Considering the propagation of TE/TM mode in parallel-plate configuration [6] we have

$$k_c d = n\pi \quad (1)$$

where ' $k_c = k_0 \sqrt{\epsilon\mu}$ ' is called cut-off wave number, 'd' is the distance between the plates, 'n' is a numeric constant taking values 0,1,2,3,,,,, k_0 is free space wave number, λ_c and f_c are the cut off wavelength and frequency respectively, ϵ and μ are medium properties.

Also, for air-filled parallel plate configuration we have

$$\lambda_c = 2d \quad (2)$$

$$\text{For propagation} \quad k > k_c \quad (3a)$$

$$f > f_c \quad (3b)$$

$$\lambda < \lambda_c \quad (3c)$$

$$\lambda < 2d \quad (\text{Using (2)}) \quad (3d)$$

$$\text{Re arranging,} \quad d > \lambda/2 \quad (3e)$$

$$\text{And for no propagation,} \quad d < \lambda/2 \quad (3f)$$

Thus, in the air region of the NRD guide Eqn. (3f) should be satisfied, so that loss can be minimized because of cut-off nature of field in air region. But in the dielectric region of the NRD guide Eqn. (3e) holds. Here, guided wavelength (λ_g), in the medium, comes in the equation which is less than the free space wavelength.

$$\text{Since} \quad \lambda_g = \lambda \sqrt{\epsilon_r \mu_r} < \lambda \quad (4a)$$

$$\text{Therefore} \quad d(=\lambda/2) > \lambda_g/2 \quad (\text{Same as (3e)}) \quad (4b)$$

Hence, condition is satisfied for wave propagation.

Any radiated waves, due to circuit discontinuities in the structure and bends along the propagation path, decay outside the strip and are suppressed because of cut-off nature of surrounding air-filled region. Hence, bends and junctions can be easily incorporated into complicated integrated circuits. This is the principle of operation of a non-radiative dielectric waveguide.



1.2.2 Design Equations for NRD Guide

From Eqn. (3f) we can safely take

$$d = 0.45 \lambda = a \text{ (As per Figure 1.02)} \quad (1)$$

And based on dispersion and bandwidth characteristics, Yoneyama [7] has given

$$b(\sqrt{\epsilon_r-1}) = (0.4-0.6)\lambda$$

which is normally accepted as $b(\sqrt{\epsilon_r-1})=0.5\lambda$ (2)

1.2.3 Propagating Modes in NRD Guide

Before discussing the modes in NRD guide, following definition needs to be understood, (assuming wave travelling in 'z' direction):

a) Hybrid modes: Those modes which are combination of pure TE($E_z=0$)/TM($H_z=0$) modes, defined in waveguide (WG) context. It contains both E_z and H_z components and, thereby, one cannot differentiate whether this is pure TE/TM mode.

Whenever in-homogenous medium is present in the transmission line, say partially filled WG, NRD guide, H Guide, etc., modes are defined whose normal component to interface/discontinuity plane is zero, in order to take field discontinuity into account. In such a case pure TE/TM modes cannot satisfy the interface conditions. We have two modes nomenclature in this scenario,

b) LSE/TE/H modes: These modes' E field lies totally in interface/discontinuity plane or there is no variation of E field in normal direction to interface/discontinuity plane. Because of this, they are also called as H modes.

c) LSM/TM/E modes: These' modes H field lies totally in interface/discontinuity plane or there is no variation of H field in normal direction to interface/discontinuity plane. Because of this, they are also called as E modes. Thus, both LSE and LSM mode are hybrid mode.

The NRD guide supports two modes that are non-radiative (Figure 1.03) namely LSE₁₁ mode and LSM₁₁ mode [8]. Since, the H field lines for LSE₁₁ mode forms circle in the NRD ground planes, it induces current in ground planes and thereby a lossy parasitic mode and a undesirable one.

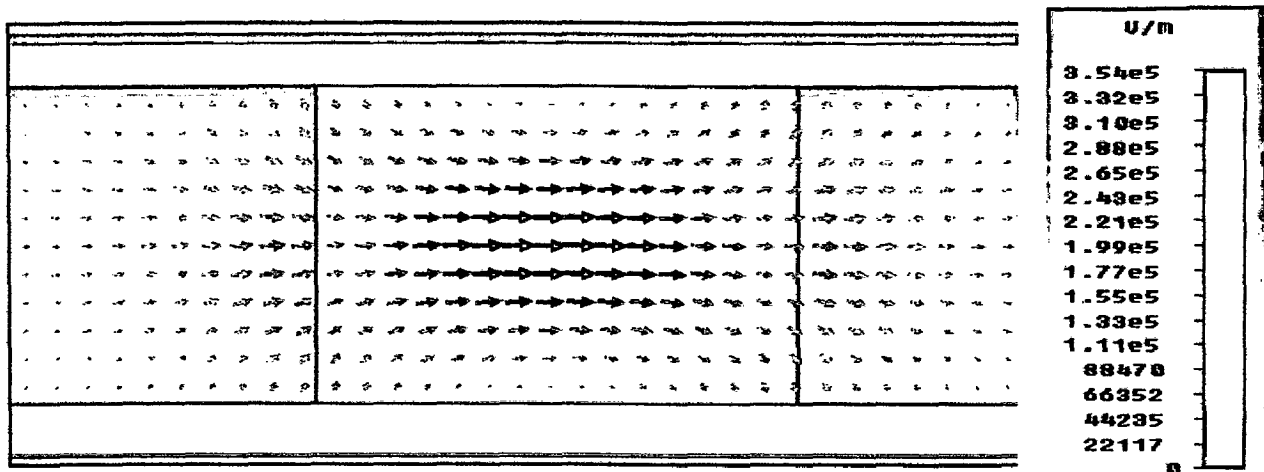


Figure 1.03a: Front view (in the X-Y plane) of the NRD guide, showing the direction of E field (from left to right) of LSM_{11} . (White portion is Dielectric, on sides - Grey portion represent Air region, on top & bottom - Light Grey regions are of ground planes. Modes animation was done through CST-MWSv2010).

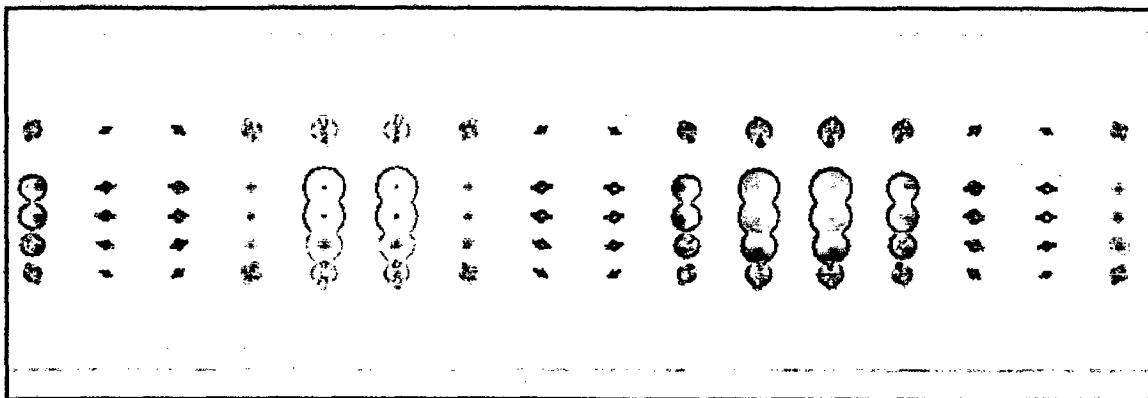


Figure 1.03b: Side view (in the X-Z plane) of the NRD guide, showing the direction of E field (into the plane of the paper) of LSM_{11} .

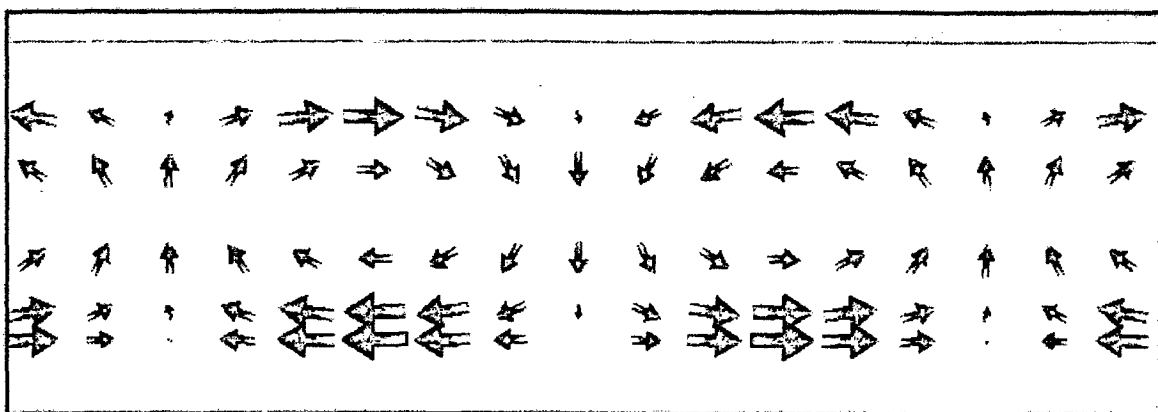


Figure 1.03c: Side view (in the X-Z plane) of the NRD guide, showing the circulation of H field of LSM_{11} .

The H field lines for LSM_{11} mode are mainly parallel to the interface/discontinuity plane, hence, it is a low-loss mode. The NRD Guide excited in the low loss LSM_{11} mode

serves as a basic building block for developing various transceiver circuit elements at millimeter wave frequencies.

To prevent excitation of the orthogonal polarization, a simple mode suppressor can be introduced, such as described in [7] to suppress the undesired mode.

1.2.4 Dispersion Bandwidth Characteristics

The Figure 1.04 below represents the dispersion characteristics for NRD guide dimensions ($a = b = 5\text{mm}$) and Teflon dielectric ($\epsilon_r = 2.04$). Ansoft HFSS [9] tool is used to simulate the design in the Ka-band (26-40 GHz). The dimensions of the NRD guide are determined using the equations mentioned in section 1.2.2. Figure 1.04 shows the two propagating modes in the NRD structure simulated for 28GHz. In the frequency range 20-30GHz, LSE₁₁ mode starts propagating first at a frequency below 21GHz, while LSM₁₁ (desired) mode starts propagating above 24GHz.

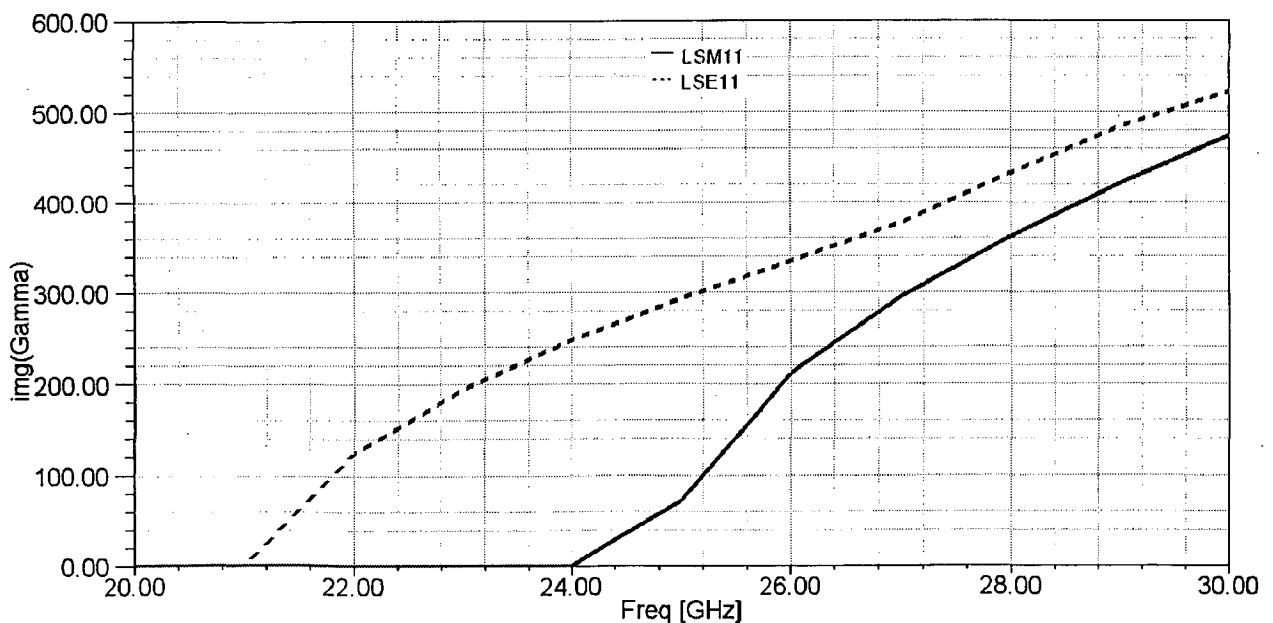


Figure 1.04: Dispersion Curve for the NRD ($\epsilon_r = 2.04$) dimensions $a = b = 5\text{mm}$.

1.2.5 Merits and Demerits of the NRD Guide Technology

The NRD guide based technology becomes attractive for use in a variety of microwave and, in particular millimeter-wave circuits and systems. Since its inception in

1981 [5], this technology has been used in design and fabrication of a large class of integrated circuits and antennas which have demonstrated superior electrical performance at millimeter-wave frequencies. Therefore, the NRD guide technology has received considerable attention in the microwave research community and commercial sectors. Essentially, the NRD guide distinguishes itself from other dielectric waveguides by the fact that its radiation losses due to circuit discontinuities and bends along the propagation path can be almost completely suppressed. Compared to planar structures, the NRD guide offers low transmission loss and low cost. It is able to form an integrated structure of multiple circuits which are sandwiched between two parallel metallic plates. In addition, the NRD guide can be used to design a class of leaky-wave millimeter-wave antennas and unidirectional dielectric radiators (UDR's).

However, the NRD guide like any other dielectric waveguide presents some difficult problems when active device integration is required. It is detrimental to the development of a complete NRD-based functional system, since it always requires an integration or an interconnection of active devices and passive components. Reference [10] gives us an idea of how an active device such as a beam lead diode can be integrated with the NRD guide. Appropriate matching network was achieved using an air gap and a high permittivity dielectric sheet.

Not only is the effective coupling requirement a problem, but also the fundamental limit of the spacing between the two metallic plates poses a threat, thereby, restricting the allowable cross-sectional surface or lateral dimension of the planar mount because the spacing needs to be smaller than half of the free space wavelength. This may lead to some extremely difficult situations when the operating frequency increases, even if only two-terminal devices are considered.

In most practical applications, three terminal active devices, such as, field effect transistors (FETs), high electron mobility transistors (HEMT's) and hetero junction bipolar transistors (HBT's), are essential in the design of oscillators and amplifiers, as well as other active circuits. However, it may prove to be very difficult, or even impossible to integrate these active devices into a planar circuit mount that physically fits within the required spacing of the NRD guide. This is particularly true when packaged devices are used. For both packaged and unpackaged devices, the surface contact between the devices and the NRD-



guides or the matching dielectric sheet is not always easy to achieve and is susceptible to air-gaps. The air-gap under this circumstance may be responsible for potential power leakage, mode conversion, and impedance mismatching. In addition, this integration scheme may be unsuitable for a large-scale batch production, thereby leading to a relatively high cost for commercial applications.

Next section covers the research work done on integrating the NRD guide with the other available transmission media, particularly, planar and waveguide (WG) type transmission lines.

1.3 NRD Guide Transition - Literature Review

This section first reports the NRD guide transition with basic planar transmission line, namely, microstrip, stripline and slot line media. The second section provides details on the NRD guide transition with available standard WG.

1.3.1 NRD Guide Transition to Planar Transmission Media

It has been recognized that planar structures are always suitable for integration with active devices regardless of a two or three terminal topology. The planar circuits may be in the form of multilayered microstrip lines or coplanar waveguides or even slot lines. At millimeter wave frequencies these lines may exhibit a prohibitive transmission loss that presents one of the fundamental limits in the design of circuits and antennas. The NRD Guide structure and performance are known to be complementary with the planar line. Therefore, if coherently designed, one can take advantage of both technologies offering their best electrical performances while the fundamental limits or inherent disadvantages of each technology can be effectively eliminated.

A schematic illustration of the Hybrid planar/NRD guide integration technology, shown in Figure 1.05, was reported in [11]. As was observed earlier, the integration of NRD guide with a planar circuit directly inserted it into an air gap of the NRD guide along the axial propagation direction, which could cause a number of design and integration problems. Therefore, the hybrid integration scheme proposed by Wu and Cassibi [20] is far better in



terms of space requirements, radiation suppression and ease of mechanical fabrication. The hybrid scheme proposed, therein, can be broadly classified into two categories namely;

- a) Aperture-Coupled Hybrid Integration
- b) Co-Layered Hybrid Integration

1.3.1.1 Aperture-Coupled Hybrid Integration Scheme

The aperture-based multilayer technique allows for a great flexibility of hybrid planar/non-planar integration and interconnects without modifying inherent characteristics of the two individual building blocks.

In [12] they modify the structure in Figure 1.05 (c) by, sideways, adding layers of metallic plates, in the air region. This mode suppresser is designed to suppress the remaining higher order spurious modes, especially TE_{20} , TE_{40} by adjusting the length of these metallic plates.

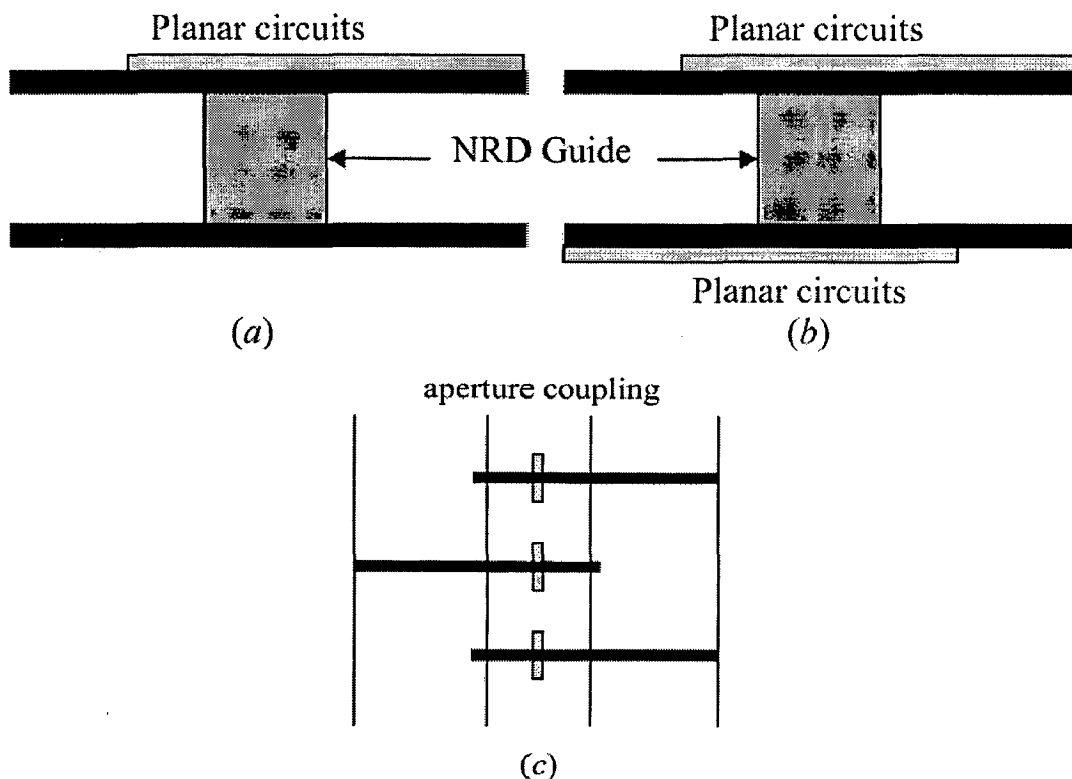


Figure 1.05: (a) Cross-section of a unilateral aperture microstrip-line to NRD guide coupling scheme. (b) Cross-section of a bilateral aperture microstrip-line to NRD guide coupling scheme. (c) Longitudinal sectional view of multiple aperture microstrip-line to NRD guide coupling scheme.

1.3.1.2 Co-Layered Hybrid Integration Scheme

In a co-layered topology, the planar circuits are in direct physical contact with the NRD guide, thus, yielding a strong electromagnetic coupling between the two dissimilar structures. This strong coupling is very helpful in generating a broadband and flat frequency response of signal transmission because potential parasitic effects relative to resonance problem may be avoided in the transition design.

Interestingly, the CPW (co-planar waveguide) and the slot line can directly be designed as part of the planar ground plane of the NRD guide as can be seen in Figure 1.06 [13]. Hence, no additional layer is required as in the case of aperture-coupling scheme. They can be free from any back side metallization, and a thick dielectric substrate can also be used. In a similar way to the aperture-coupled topologies, the co-layered CPW and the slot line can be realized on both ground planes of the NRD guide, thus, making a very compact integration of planar and non-planar structures. This suggests that this type of co-layered circuits is compatible with uniplanar design techniques. In this co-layer arrangement, both electric and magnetic coupling are possible for the transition design.

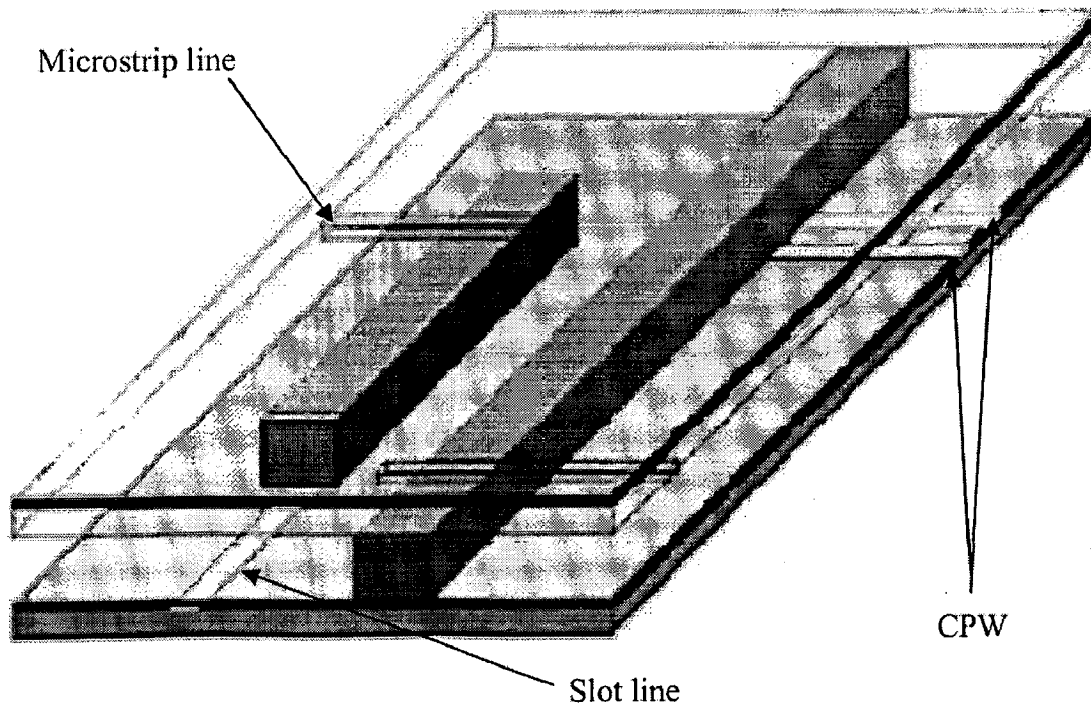


Figure 1.06: Co-Layered CPW/Slot line/Microstrip to NRD scheme [13].



1.3.1.3 Integration with Suspended Stripline

The Suspended Strip Line (SSL) or the Shielded Suspended Strip Line (SSSL) is another transmission medium reported for millimeter wave integrated circuits [14]. It overcomes the disadvantage of maintaining tight dimensional tolerances, as in rectangular waveguide. The main advantages of the suspended strip line are low loss, ease of fabrication, single mode propagation from DC to millimeter wave frequencies, less dispersion, and easy integration with other planar and non-planar transmission lines. Hence, the low loss, low production cost and ease of integration are the main factors that make the NRD guide – SSL integration promising for wireless communication applications at millimeter-wave frequencies.

For integrating the SSL to the NRD guide, either of the two topologies discussed can be used. The concept of probe-type of transition between stripline and NRD guide was first proposed in 1990 [15] and a working model with suitable variations have been reported in [16]. The coupling mechanism basically involves field matching of the dominant LSM mode of NRD guide and Quasi-TEM mode of stripline, the fields of which are shown in Figure 1.07 below.

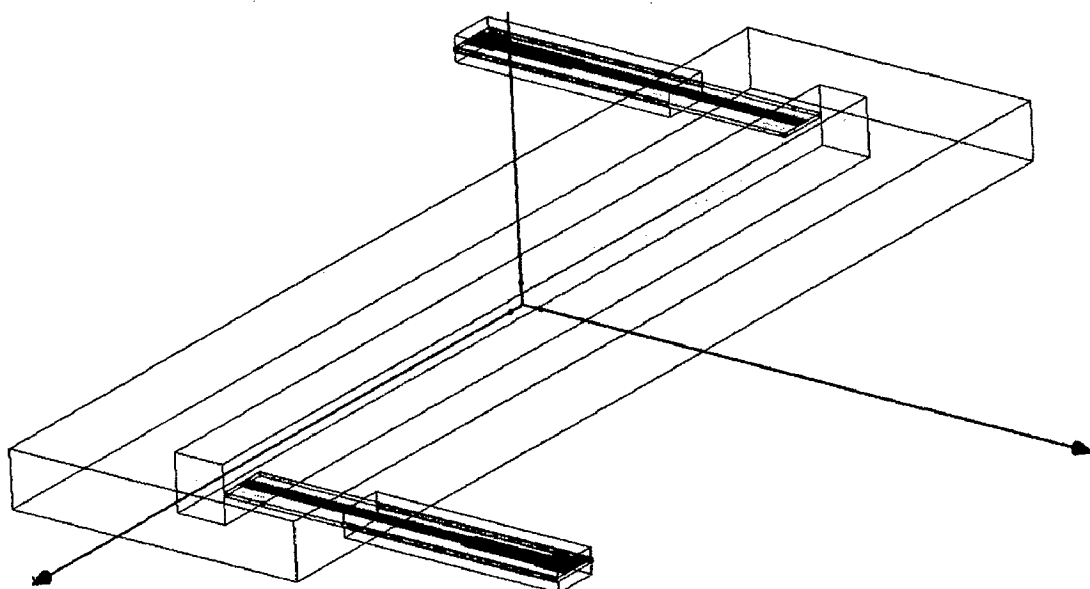


Figure 1.07: SSSL-NRD guide transition. Air gap has been extended beyond the dielectric strip for explanation purpose. Purple color geometry is the trace metal of the SSSL. Top and bottom ground planes of NRD guide are hidden, in order to have better view of the transition. Design was implemented using HFSS V13 from Ansoft.

1.3.1.4 Integration with Slotline

The slot line structure consists of a dielectric substrate metalized on one side only. The metallization has a completely separate narrow hybrid mode of the quasi TE type that propagates along the slot. This structure cannot support Quasi-TEM mode of other strip transmission lines. Slot line mode has no cut-off frequency and the main energy concentration is in the slot, or close to it. Figure 1.08 shows field lines for a slot line mode.

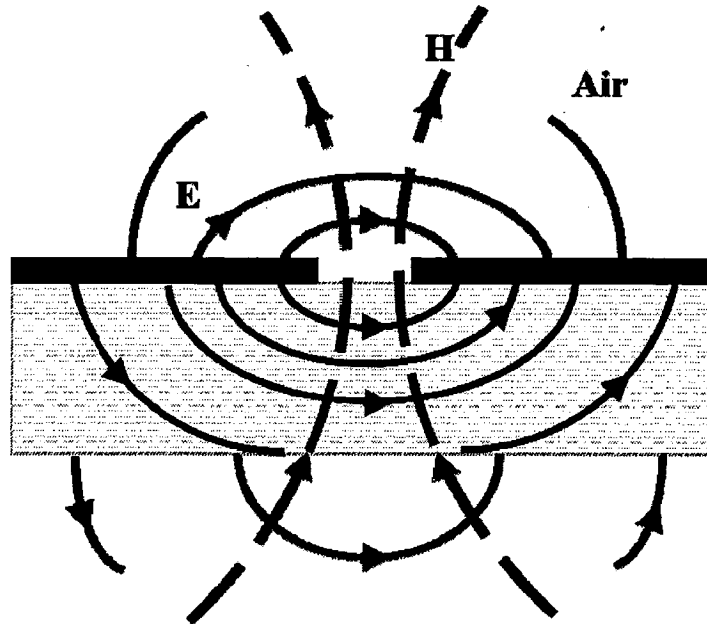


Figure 1.08: Field lines for Slot line mode.

The integration mechanism of NRD guide to slot line is possible by placing the slot line at the center of the NRD guide such that the E field lines of the slot line mode and the dominant LSM mode of the NRD guide become parallel to each other [17].

1.3.2 NRD Guide Transition to 3D Structures - Literature Review

This section discusses the first main topic of this dissertation, viz., 3D transition, or to be precise, rectangular WG (WR) transition to NRD guide, operable at Local Multi-point Distribution System (LMDS) band/28GHz. Thus, NRD guide was designed with center frequency of 28 GHz, The material taken was teflon ($\epsilon_r=2.04$). Our desired frequency range of operation is Ka band (26-40 GHz). In this range of operation, two standard WRs can be used for transition, namely WR28 and WR34 [10]. Their respective details will be provided in the next chapter.

A review on work done so far in 3D transition to NRD guide is first provided. Most of the transitions discussed here are having some commonality. Like, almost all the reported geometries are having 'transition interface' with the NRD guide at the front/back side of it, with an exception [18], in which WR is used to transfer power via dielectric strip by drilling the WR sized slots in the ground plane.

Second group of transitions are those in which dielectric strip extends into the 3D structure having E/E-H plane taper in the transition region between 3D structure and NRD guide, with an exception [19] that does not include 'any plane' taper. In fact, tapers are neglected in order to easy the fabrication. As can be seen from Figure 1.06 the E field has been matched between waveguide (TE_{10} mode) and NRD guide (LSM_{11} mode).

In [20], they introduce a change in the set up of [19] and implement single plane tapering of the dielectric strip, fed by WR 28. It has used set of impedance matching layers in NRD guide itself, Figure 1.09.

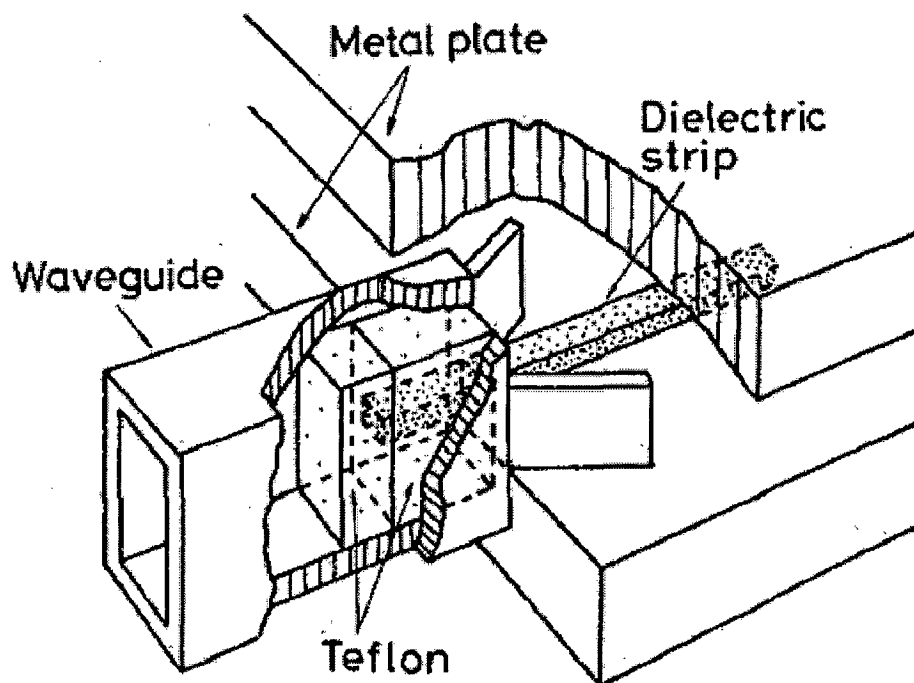


Figure 1.09: Structure of transition used in [19].

Yet another approach employing 3D structure as horn antenna and tapering the dielectric strip is detailed in [21-23]. In [21], first they fix the length of the taper section to

about $5\lambda_g$, then, flare length, plane and angle are chosen based on experimental study on the transition loss introduced by horn antenna. On the basis of this study, the flare angle in the E-plane was fixed at 31 degrees having a length of twice the free space wavelength. Later on they used this transition to feed the dielectric rod antenna. In this also, the E field has been matched between waveguide and NRD guide.

Malherbe [22] reports a composite transition. In that, the first part is a transition between standard rectangular waveguide and a reduced-width, dielectric-filled metal waveguide. The second part is a transition between the reduced width guide and the NRD, where the width is now kept constant at the plate separation. Here also, E field matching has been implemented.

Yoneyama and Nishida [23] present a different transition from [21]. It consists of horn flared in the E-plane and tapered in the H-plane as shown in Figure 1.10.

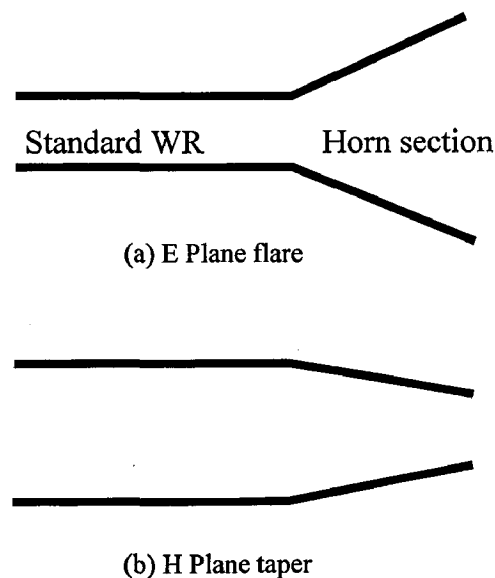


Figure 1.10: Structure of transition used in [23] (a) Top view and (b) Side view of the transition used.

Next section details the plasmonics basics, different media available for plasmon propagation, basics characteristics graphs relating to its propagation and optical properties of metals.

1.4 Plasmonics Basics

Miniaturization of photonic devices such as waveguides and cavities for guiding and confining electromagnetic energy at visible and near-infrared frequencies towards the sub-100-nm size scale is limited by the well-known diffraction limit of light [24]. This diffraction limit states that it is not possible to focus or confine a three-dimensional light beam to a lateral size smaller than about half its wavelength in the host medium. Applied to optoelectronics, the diffraction limit opposes the creation of dielectric waveguides or fibers that can confine the guided light – the optical “mode” – to a lateral dimension smaller than a couple of hundred nanometers for visible and near-infrared light. Both conventional waveguides and light guides based on dielectric photonic crystals suffer from this fundamental integration limit. In microscopy and biology, the diffraction limit hampers the detection of ultra-small amounts of molecules in cellular concentrations by limiting the focusing power of conventional lenses [3]. Apart from considerable fabrication challenges, further size reduction of nano-electronic circuits will be governed by the constraints imposed by the switch to quantum information processing and ultimately by the physical limits of computation imposed by energy and entropy considerations [25].

In order to break the diffraction limit, clearly a different approach from the simple scaling down of dielectric micro-photonic waveguides and cavities is needed by employing not dielectric but conducting and, thus, metallic materials such as Au and Ag for the creation of functional photonic devices. The ability of plasmonic structures to confine light to volumes significantly smaller than the diffraction limit of light, cater to above said problems.

1.4.1 Surface Plasmon-Polaritons (SPP)

Plasmon is a quasi-particle (*i.e.*, combination of a particle and its influence on the local environment) resulting from quantization (discrete level separation) of plasma oscillations, which are rapid oscillations of the electron density in conducting media such as plasmas or metals. Surface plasmons (SPs) are transverse magnetic (TM) modes that propagate at metal-dielectric interfaces and constitute an electromagnetic field coupled to oscillations of the conduction electrons. Plasmons can couple with a photon to create another quasi-particle called a plasma polariton or plasmon polariton. When these electron density

waves propagate along the surface of a metal they are strongly coupled to oscillating electromagnetic fields (i.e. light) and termed surface plasmon-polaritons (SPPs) [26]. SPPs are electromagnetic excitations that propagate at the interface between a dielectric and a conductor, and are evanescently confined in the perpendicular direction.

The concept that the optical mode diameter of SPPs can be significantly smaller than the wavelength of light, has generated interest photonic devices that can fully exploit the nano-scale control afforded by such nano-metallic structures.

1.4.2 Surface Plasmon Dispersion

The motion of a scalar wave ψ with propagation parameter $k = 2\pi/\lambda$ through any isotropic medium is described by equation $\nabla^2 \psi + k^2 \psi = 0$. If the medium is 'dispersive' such that the dielectric constant exhibits frequency dependence, then k will also have frequency dependence. Dispersion relation for bulk plasmon is given by:

$$k(\omega) = \omega/v = \omega/(c/n) = \omega \sqrt{\epsilon(\omega)}/c \quad (1)$$

$$k(\omega) = (\omega/c) \sqrt{1 - (\omega_p/\omega)^2} \quad (2)$$

where ω_p is called as the plasma frequency and it depends on electron property and constituting material;

$$\omega_p = (ne^2/m\epsilon_0)^{1/2} \quad \text{rad/sec} \quad (3)$$

where n, e & m deals with number, charge and mass of electron(s) and ϵ_0 is free space permittivity. As $\omega \gg \omega_p$, $k(\omega)$ approaches $k_0 = \omega/c$ asymptotically. The E -field oscillation frequency becomes so high that the electron motion can no longer follow it, and the electron plasma medium becomes essentially transparent. As ω approaches ω_p , $k(\omega)$ approaches zero, and the wavelength of propagation approaches infinity. The electrons throughout the medium oscillate collectively at the plasmon frequency. At frequencies $\omega < \omega_p$, $k(\omega)$ becomes pure imaginary and the wave ψ_{0e}^{ikx} becomes evanescent. The wave decays exponentially into the medium and penetrates only to the propagation depth $\delta = k^{-1}$ [26].

In addition to plasmon waves propagating in the electron gas volume, they can also exist at the surface between the plasma and a dielectric. One can obtain the dispersion relations for these surface waves by writing the relevant Maxwell's equations and the continuity conditions for E - M field incident on the surface. TM (transverse magnetic)

polarization is assumed because surface waves with TE (transverse electric) cannot exist. The dispersion relation of SPPs propagating at the interface between the two half spaces is:

$$k(\omega) = (\omega/c) * \sqrt{(\epsilon_d \epsilon_m) / (\epsilon_d + \epsilon_m)} \quad (4)$$

The propagation distance of the mode along the surface in the x direction, δ_{sp} is determined by the imaginary component of the x-direction wave vector k_{sp} :

$$\delta_{sp} = 1/2 * \text{img}((k_{sp})) \quad (5)$$

in which k_{sp} is a function of the metal and dielectric permittivity's as in Eqn. 3.

The decay length of the SP electric field in to the dielectric in the (normal to the surface) L_{sp} is given by the inverse of the purely evanescent surface normal wave vector k_z .

$$L_{sp} = 1/|k_z| \quad (6)$$

Figure 1.11 (a), (b), and (c) illustrate the above 3 quantities, namely, surface plasmon wave vector, propagation length and field confinement with respect to frequency of operation.

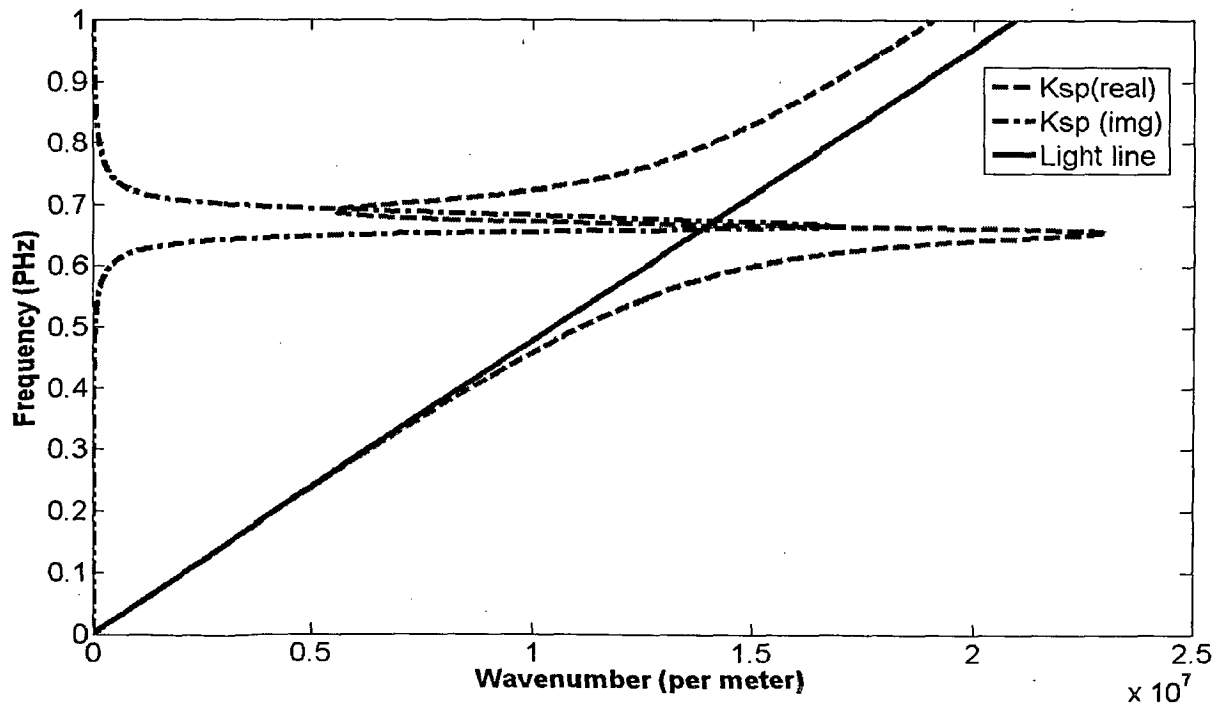


Figure 1.11 (a): Frequency-dependent properties of a surface plasmon on a gold-air interface-In-plane wavevector k_{sp} .

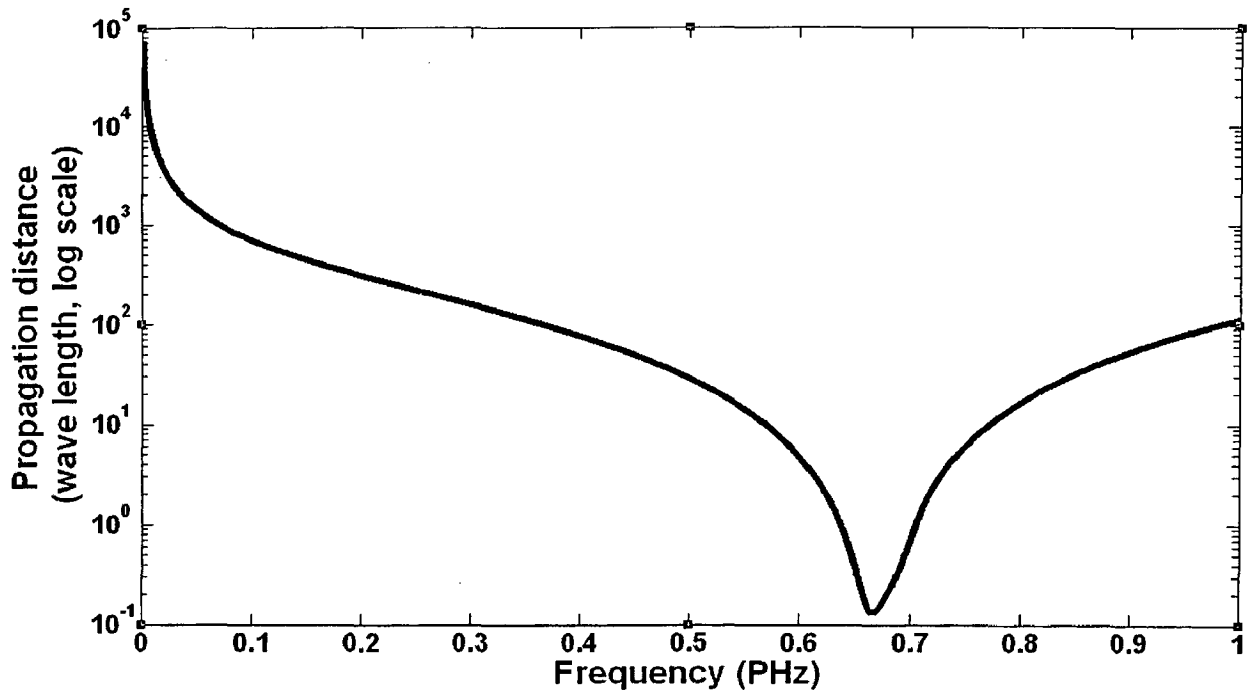


Figure 1.11 (b): Frequency-dependent properties of a surface plasmon on a gold-air interface-Normalised propagation length δ_{sp}/λ .

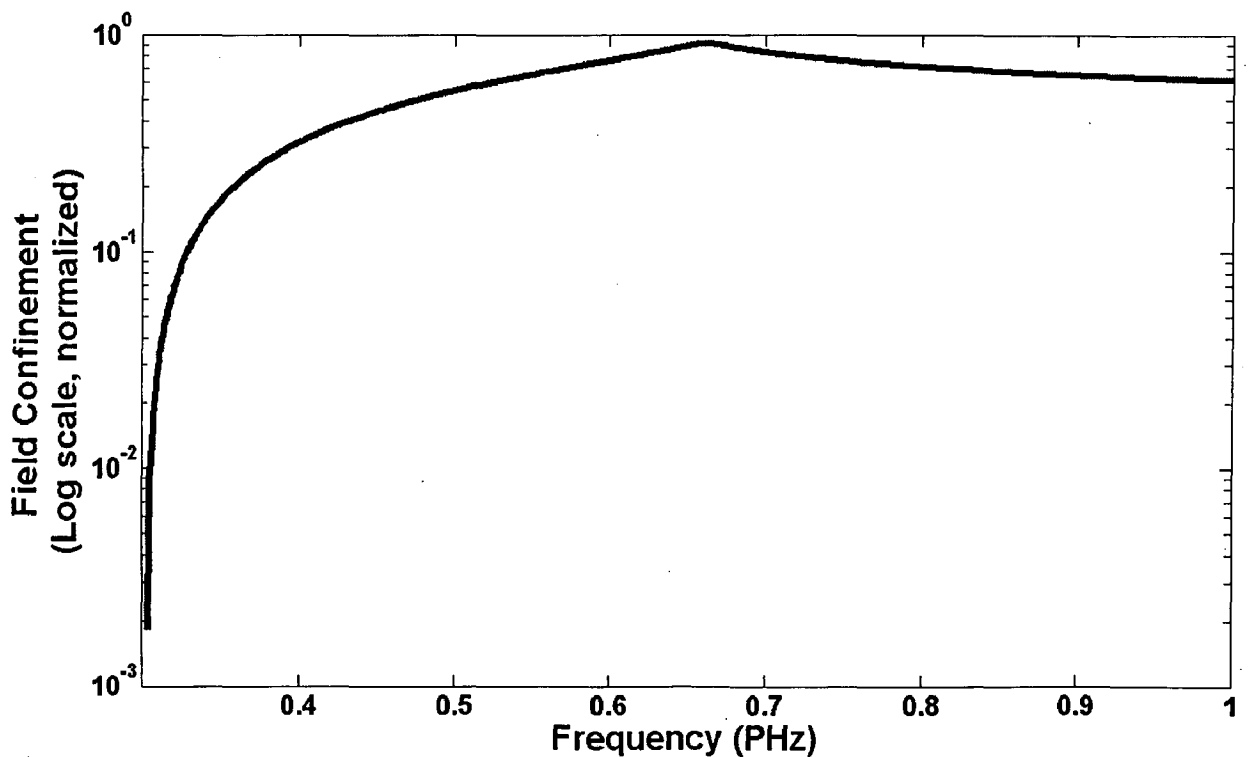


Figure 1.11 (c): Frequency-dependent properties of a surface plasmon on a gold-air interface-Normalised field confinement $(\lambda-L_{sp})/\lambda$.

This characteristic trade-off between localization and loss is typical for plasmonics. The field confinement below the diffraction limit of half the wavelength in the dielectric can

be achieved close to ω_{sp} . In the metal itself, the fields fall off over distances on the order of 20 nm over a wide frequency range spanning from visible to infrared [26].

1.4.3 Optical Properties of Metals

The response of a material to incident light is expressed as the complex refractive index $N = n+ik$, or as the complex dielectric function $\epsilon = \epsilon' + i\epsilon''$. The optical properties of many materials are approximately independent of frequency, at least over a given region of interest in the spectrum. For example, for a transparent dielectric such as glass (SiO_2) $\epsilon_r = 2.5$ throughout the visible range.

The dielectric properties of metals vary strongly as a function of optical frequency. Also, optical properties of some metals are influenced by free electrons and can be modeled quite well by using only the Drude or zeroth-order term of the Lorentz Drude (LD) multi-oscillator model [27], which is given by:

$$\epsilon(\omega) = 1 - \frac{\omega_p^2}{\omega^2 + i\gamma\omega} \quad \text{where} \quad \omega_p^2 = \frac{ne^2}{\epsilon_0 m} \quad (1)$$

ω_p is the bulk plasma frequency of the free electron gas and γ is called free electron collision frequency. The applicability of the Drude model can be extended by adding two additional fitting parameters, ϵ_{static} and ϵ_{high}

$$\epsilon_{\text{ExtendedDrude}}(\omega) = \epsilon_{\text{high}} - ((\epsilon_{\text{static}} - \epsilon_{\text{high}}) * \omega_p^2 / (\omega^2 + i\omega\gamma)) \quad (2)$$

Drude parameters for Ag and Au, valid for various frequency bands, are tabulated in the Appendix, C. These parameter values have been used in the simulations, presented in this report. There are plethora of literatures [28]-[32] giving different models to mimic the behavior of metals at Tera/peta Hertz, tabulated data for the various parameter for metals, equations, and graphs to illustrate metal's optical properties.

1.5 Plasmonic Slot Waveguide

The electromagnetic response of metals in the infrared and the visible spectrum is characterized by a largely imaginary index of refraction enabling the definition of waveguides with sub diffraction scale optical propagation. There is a basic trade-off in all



plasmon waveguide geometries between mode size and propagation loss. One can have a low propagation loss at the expense of a large mode size, such as in the work of Nikolajsen, *et.al.*, who reported propagation losses of 6 dB/cm for 20nm slabs of gold, but with a 12 μm mode diameter [33]. At the other extreme, Takahara, *et. al.*, predicted guiding in 20 nm diameter silver nanowires, with a mode field diameter of about 10 nm, but with theoretical propagation losses of 3 dB/410 nm [34]. Though this loss is acceptable for nano-scale photonic circuitry, large scale integration with such losses is not feasible. Plasmon based-waveguides are not the only way by which light can be guided on small scales. In particular, dielectric ridge waveguides of Silicon in Silicon-On-Insulator (SOI) exhibit low propagation loss of 6-7 dB/cm. Though the mode size is fundamentally diffraction limited, 90% of the optical energy is contained in a 1.5 square micron region, in such waveguides as detailed below. Due to the low achievable loss, SOI waveguides show a promising path for chip-scale device integration [35]. There are many structures (simulated/fabricated) reported which employ SOI for launching the beam into the plasmon guiding media, which will be detailed in upcoming chapters.

Plasmonic waveguides possess highly confined modes, thereby, allowing one to increase the level of circuit integration. Different plasmonic waveguide structures like strips [36], nano-particle chains, nanowires, grooves, wedges and gaps have been developed and investigated. Among various structures, the gap plasmon waveguide (GPW) is particularly interesting, because its modes are extremely small and its fabrication process is comparably simple [37]. In addition, the metallic sidewalls of the waveguide provide strong lateral confinement which enables low-loss light propagation through sharp bends, allowing very compact plasmonic devices to be realized [38].

Recently, it has been shown that the excitation of long-range SPP modes along metal strips with sub wavelength cross-section fulfills this purpose. Therefore, the SPP strip is less a waveguide but more an optical analogy of the transmission line common to microwave and radio frequency spectrum, even though only a single conductor is present. A detailed study of the strip SPP transmission line was presented by Berini [39] who modelled straight metal strips with rectangular cross-section by means of the semi-analytical method of lines.

An alternative approach to achieve high field confinement is based on the excitation of surface plasmon polaritons (SPPs) in metal/dielectric waveguide structures. SPPs are surface localized light waves at dielectric-metal interfaces which are coupled to free electron oscillations in the metal. However, high propagation losses are typically associated with SPPs due to the losses in the metal, and a fundamental trade off must be achieved between field localization (SPP mode extension) and propagation losses.

It has been noticed that the dielectric filling of a metal slot waveguide dramatically improves the field localization of guided SPP waves. However, it is also found that the increased field localization in dielectric-filled metal slots is necessarily accompanied by an increase in the propagation losses. So, this structure has an inherent trade-off related to the use of metal-dielectric structures. A schematic diagram for the proposed partially filled metal slot-waveguide structure is shown in Figure 1.12. The structure is composed of a thin-film metal slab deposited on a substrate, with a small trench (the slot region) etched and partially filled with a high-index dielectric medium.

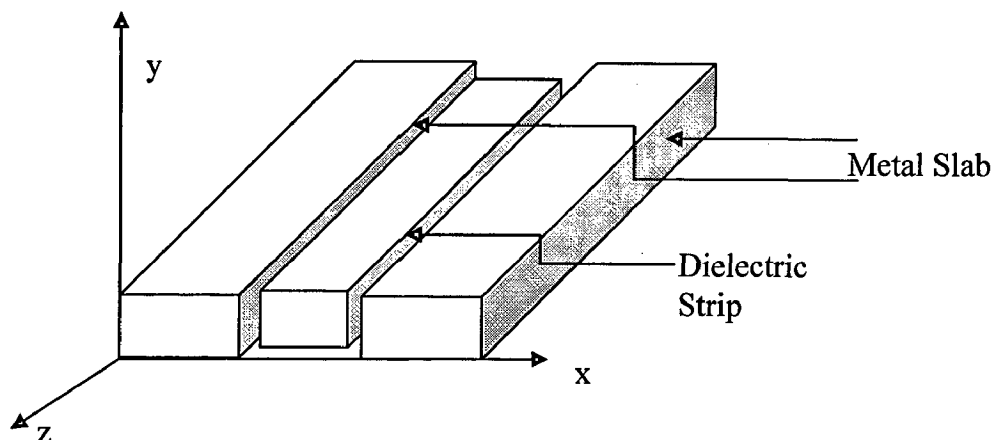


Figure 1.12: Schematic diagram of the dielectric filling metal slot waveguide.

1.5.1 Variants of Plasmonic Slot Waveguide

In order to improve field localization while keeping propagation loss low, the concept of partial dielectric filling of metal slot waveguides (partially filled metal slots) is used. Two partially filled metal slot configurations were discussed: horizontal partial dielectric filling (HPDF) and vertical partial dielectric filling (VPDF) waveguide structures [40].

We now consider a symmetric plasmonic slot waveguide, Figure 1.13(a) structure is composed of a slot in a thin metallic film embedded in an infinite homogeneous dielectric. The fundamental mode supported by the reference plasmonic slot waveguide is, therefore, a bound mode. Since, the slot dimensions are much smaller than the wavelength in the frequency range of interest, therefore, this waveguide does not support any higher order propagating bound modes. The propagation length decreases as the wavelength decreases. This is consistent with the behaviour of plasmonic structures in general, since, the fraction of the modal power in the metal increases at shorter wavelengths [41].

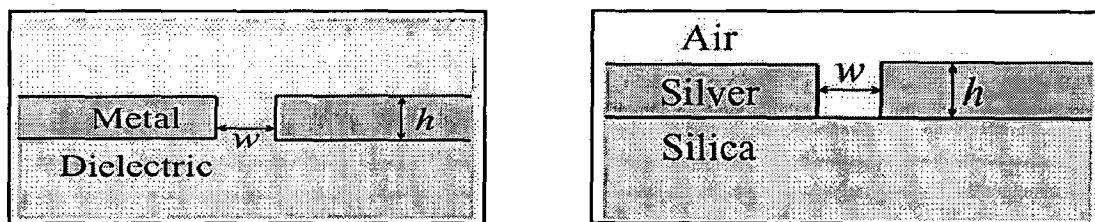


Figure 1.13: Variant slot plasmonic waveguide (a) Symmetric, (b) Asymmetric [41].

Consider the counter part of symmetric type, *i.e.*, asymmetric plasmonic slot waveguide structure, Figure 1.13(b), in which the surrounding dielectric media above and below the metal film are different. More specifically, we consider a waveguide that consists of an air slot of width w in a metallic film of thickness h deposited on silica. Unlike the symmetric case, the fundamental propagating mode is not always bound in the asymmetric case.

Another variant called 3-D plasmonic strip waveguide Figure 1.14, which is analogous to the microstrip waveguide used at microwave frequencies. This structure

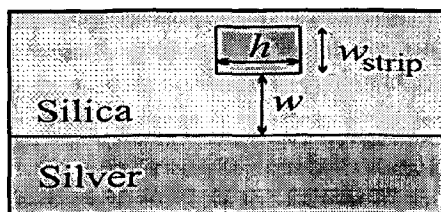


Figure 1.14: Cross section of plasmonics strip waveguide [41].

supports a highly confined mode in the region between the metal strip and the metallic substrate. This design is similar to that reported in [36] and [39]. [42] also brief the above discussed structures along with its field configuration but there they discussed with different geometry, taking co-axial geometry.

In particular, metal slot plasmonic waveguides were shown to support guided modes with high confinement at infrared wavelengths. Such structures seem promising for guiding into sub-wavelength nano-scale photo detectors, as they support a high integration density. In

design of optoelectronic circuits based on this geometry, it is desirable to calculate the transmission and reflection properties when waveguides with different parameters are connected together. Thus, different modelling strategies are employed in order to model it correctly and gain full insight into the optoelectronic circuits. Here, we will briefly touch upon two modelling scheme, first transmission line model followed by the characteristic impedance model.

1.5.2 Transmission Model of Surface Plasmon Waveguide (SPWG)

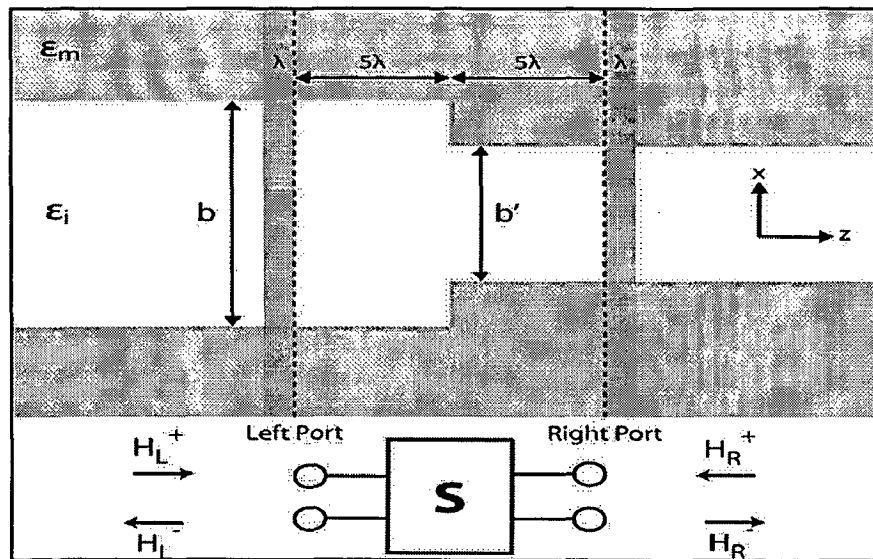
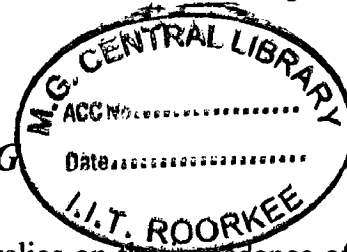


Figure 1.15: Description of the modeling geometry. Dashed lines represent the location of the left and the right ports of the overall scattering matrix $[S]$ that describes this junction (schematically shown in the bottom). Gray areas on the left and the right of the ports are the regions in the simulation space used to extract the reflection coefficients S_{11} and S_{22} . Top and bottom consist of metallic layer ϵ_m sandwiching dielectric layer ϵ_i [43].

Consider the MIM (metal-insulator-metal) waveguides, Figure 1.15, consisting of two layers of metal separated by an insulating dielectric layer. When there is only one propagating mode, far away from the waveguide junction, the fields can be written in terms of that main mode of the system since all higher order modes will have an exponential decay much faster compared to the main propagating mode. Under such circumstances, the effects of the waveguide junction on the propagating modes can be described using the single-mode scattering matrix (S). The elements of the scattering matrix S_{11} , S_{12} , S_{21} , and S_{22} are complex numbers that describe the phase and the magnitude of the reflection and the transmission of the main modes. Thus, in general, there are eight independent real numbers in S , including

the magnitude and the phase information. However, under certain conditions the number of independent parameters can be reduced. In the vicinity of the waveguide junction, higher order modes will be excited. We initially chose the left and the right ports of our junction sufficiently away, in this case 5λ , from the physical junction, where the amplitudes of the higher order modes are negligible [43].

1.5.3 Characteristics Impedance Model of SPWG



Kocabas [44] uses transfer matrix approach that relies on the impedance of the mode to describe the behaviour of the fields as they propagate through a series of different waveguides. This model is analogous to the mode-matching approach in microwaves where multiple modes may be considered. However, in the case of the slot waveguide, Figure 1.13(a), there exists a range of parameters where the waveguide supports only one bound propagating mode. For such structures, it is possible to use a transfer matrix to relate the coefficients of the forward and the backward versions of the propagating mode in a linear fashion, along with the transmission and the reflection coefficients at each of the discontinuities along the propagation direction. By knowing the propagation constants of a given waveguide section, the transmission properties of an arbitrary waveguide can be calculated.

1.5.4 Applications of Plasmonics

The possible applications of plasmonics abound in any field which would benefit from enhanced control of photons; from beam steering to single-molecule bio-detection. In the area of optoelectronics, plasmonics meet demands for optical interconnects which are small enough to co-exist with nano-scale electronic circuits. Emerging technologies include very small, low-power active devices such as electro optic or all-optical modulators. Passive plasmonic devices, or “optical antennas,” are being used to enhance the performance of emitters and detectors, and to harvest sunlight for photovoltaic. Even such extraordinary technologies as micro-targeted infrared cancer therapy and “invisibility cloaks” are on the horizon.



In the areas of life sciences, drug discovery, medical diagnostics, environmental monitoring, food safety, as well as protection against biological and chemical warfare there is an increasing demand for biochemical sensors. Such sensors should be highly sensitive, label free, compact, and easy to use. As attractive alternatives to several technologies employing nano-wire and nano-pore conductance measurements, nano-wire crossbar arrays, nano-particle probes, and nano-mechanical resonators, optical waveguides are a promising technology to fulfil these requirements. Optical-waveguide-based approaches work by sensing the presence of analytes as effective refractive index (RI) changes displayed by the guided mode and, thereby, avoiding prior fluorescent or radioactive labelling. The sensitivity of an optical waveguide sensor relies on the amount of light in the medium to be sensed. Recently, the slot waveguide was proposed as a guiding structure capable of high sensitivity in biochemical sensing applications [45]. Besides, colour filtering is currently one of many areas where passive photonic and plasmonic devices are being explored for spectral imaging applications.

Having discussed the start up and necessary basics relating to NRD guide transition and plasmonics slot waveguide, we are now ready to detail out the objective of this report.

1.6 Statement of Problem

Objective of this thesis is to analyze dielectric guide structures useful at millimeter wave and optical frequencies with the help of commercially available 3D electromagnetic (EM) simulators. In particular, objective includes:

- 1) Simulation of WR-28/34 to NRD guide transition operable at 28 GHz (LMDS Band).
- 2) Simulation of horn antenna to tapered NRD guide transition centered around 28 GHz.

Along with this, design of two planar filter circuits is also studied. This requires:

- 1) Simulation of Coupled Stepped Impedance Resonator (CSIR) based Band Pass Filter (BPF) with Bandwidth (BW) of 2 GHz centered around 28 GHz.
- 2) Simulation of CSIR based Band Stop Filter (BSF) with BW of 2 GHz centered around 28 GHz.



Moreover, the second type of work includes simulation of IR and visible frequencies structures, called plasmonic structures. It covers:

- 1) Simulation of NRD guide at Terahertz, thereby verifying [46].
- 2) Simulation of slot waveguide type structure or Metal-Dielectric/Insulator-Metal (MIM/MDM) geometry at Tera/Peta-Hertz.

The two main transmission media, namely NRD guide and plasmonic interface, on which this report is based, its chapter wise breakup is detailed in next section.

1.7 Organization of this report

This report has been divided in following chapters:

Chapter 1 describes the fundamentals of NRD guide plasmonic slot waveguide. It is followed by review of the work done on NRD guide transitions and plasmonic slot waveguide structures.

Chapter 2 discusses the simulation results of NRD guide transition and millimeter wave circuits, mainly band-pass filter (BPF) and band-stop filter (BSF).

Chapters 3 and 4 attempt to reproduce the results that are reported in the plasmonic literature for slot wave guide geometry, specifically, Metal Dielectric/Insulator Metal (MIM/MDM) and (Dielectric1/ Dielectric2/Metal)D1/D2/M geometry.

Finally, *Chapter 5* recaps the results, discusses on the work done and suggests scope for improvement on the designs, done in this dissertation.



Chapter 2

NRD Guide Based Millimeter Wave Circuits

2.1 Introduction

This chapter discuss two different designs of NRD guide transition, one of them a novel transition at LMDS band, using WR28/34 and the other one is implementation of [25] at LMDS frequency band. Apart from this, design of mmw based passive circuits-band pass filter and band stop filter is also discussed.

2.1 WR28/34-NRD Guide Transition

2.1.1 Geometry of the Setup

The geometry of the standard WR to NRD guide transition is shown in Figure 2.01 (Top View). This transition is based on matching the magnetic field in both the regions, *i.e.*, in WR28 and NRD guide. In this view metallic ground planes, which are covering top and bottom of the guide, except at the WR locations, are not shown so that the variables can be defined which, in turn, help in understanding the geometry and setting up the simulations.

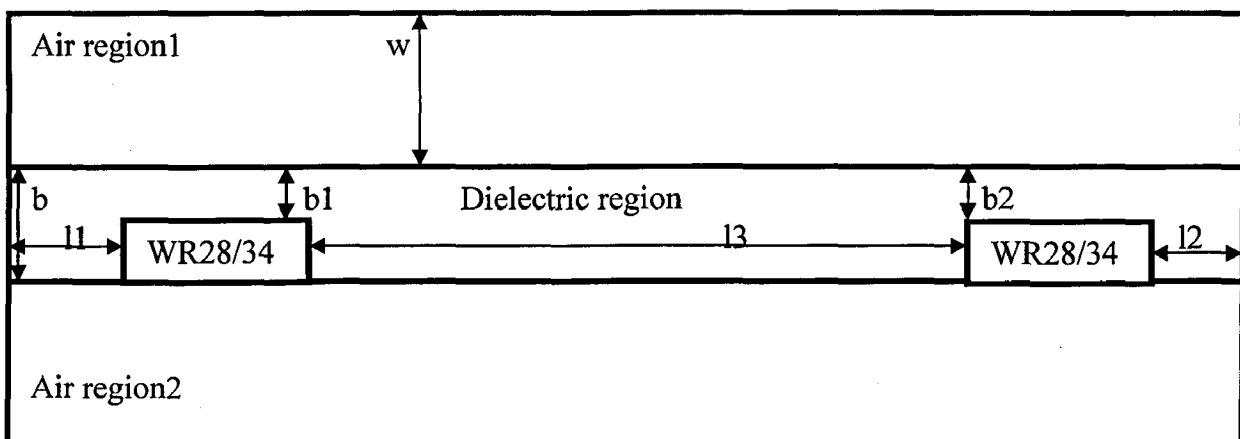


Figure 2.01: Top view of the standard WR to NRD guide transition, for defining the optimization parameters during simulations.

Two WRs are placed on top (say) of the NRD guide for illustration purpose, they can also be placed antipodal, one WR on each ground plate. Their respective dimensions can be obtained from [11] by inspecting the desired range of frequency. Say for our case, operation

in Ka band (26-40 GHz), the center frequency (f_c) 28GHz requires standard WR28 or WR34 whose details from [11] are given in Table 1.

Table 1: WR28 & WR34 Specifications [11]

Standard WR	Inside Dimensions (mms) a*b	Cut Off frequency (in GHz)	Recommended Frequency Range for TE ₁₀ mode (in GHz)
28	7.11*3.555	21.097	26.4-40.0
34	8.64*4.32	17.361	21.7-33.0

NRD guide dimension can be calculated from the formulae given in section 1.2.2, for given material constant and cut-off frequency, f_c . In present case, it is $a = b = 5\text{mm}$, almost and $\epsilon_r = 2.04$. Remaining variables (l_1, l_2, l_3, b_1, b_2) which can be seen in Figure 2.01 are used in optimization of the structure during simulation or in fact these variables define the optimum position of the WRs so that large pass band or low insertion loss for very large bandwidth can be achieved.

2.1.2 Simulation setup for WR28/34-NRD guide transition

The transition which will be discussed next is simulated using finite element method (FEM) based algorithm. Commercially, FEM is implemented by Ansoft's High Frequency Structure Simulator (HFSSv13) tool. The values of variables (defined in Figure 2.01), which are obtained after simulating and optimizing the structure in Figure 2.02 are given in next section. During simulation setup, make the afore-mentioned variables as HFSS design variables and then mark them for optimization.

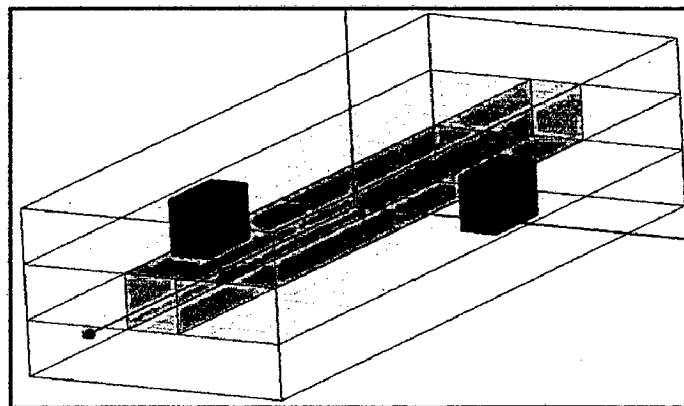


Figure 2.02: Ansoft HFSSv13 set up for simulating the structure in Figure 2.01. (Light green box is dielectric slab placed between air regions 1 and 2, purple boxes are WR's cut in the ground planes).

Following are the steps which are followed during optimization of the transition, WR-NRD Guide, on HFSS:

- a) Initially place the WR symmetrically, about X axis.
- b) Keep l1 and l2 values to $\lambda_g/4$ so that the waves from the input WR and from the NRD guide end cancel out because of 180 degree phase difference. Then, in subsequent simulation setup keep incrementing l1/l2/both l1&l2 by $\lambda_g/4$.
- c) We can even run the simulations by placing WRs antipodal and follow the above steps.
- d) Variables, b1 and b2, can be used to fine tune the response. But this is not always correct.
- e) Maintain l3 to a minimum value of 2 or 3 times λ_g so that the evanescent modes can die out completely. Results worsen once WRs reach too close.
- f) The length of the air region, on either side, from the dielectric air interface should be greater the one free space wavelength, in this case it is 10.7 mm (=w, in Figure 2.01). Figure 2.03 shows that increasing w, greater than $1 \lambda_0$, reduces the cut-off frequency.

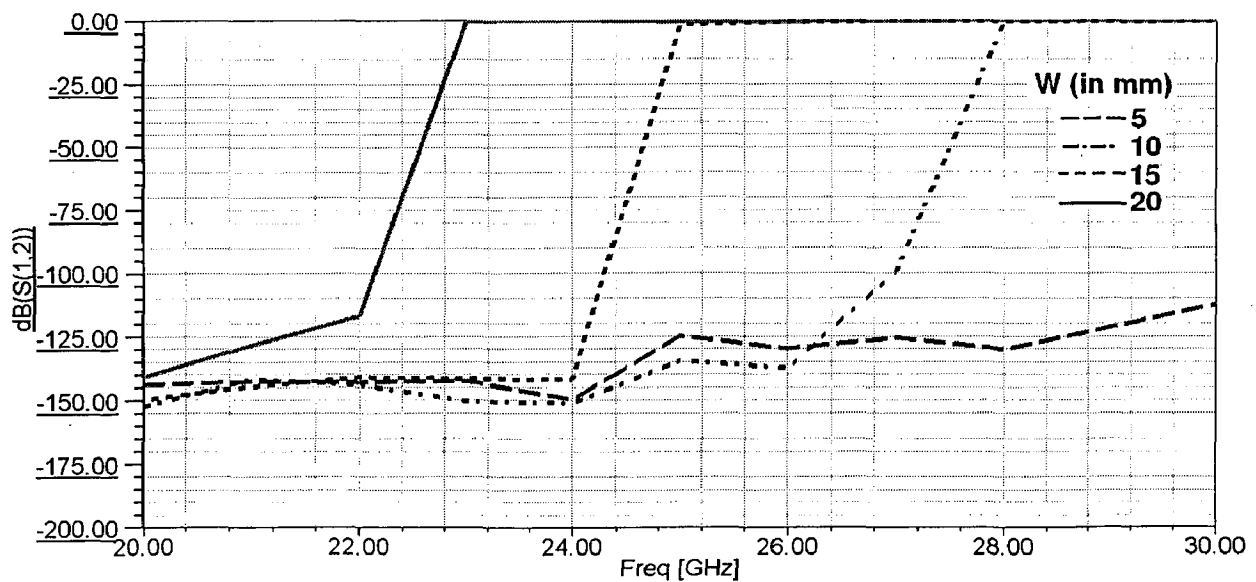


Figure 2.03: Effect of w, in Figure 2.01, on insertion loss.

2.1.3 Response of the WR28-NRD Guide Transition

Figure 2.04 shows the simulated response for transition in Figure 2.02, after following the steps given in previous section. The optimization variables defined in Figure 2.01 are

specified with HFSS CreateBox command. The final physical values relating to transition, in terms of position of WRs, are given below (all dimensions in mm):

- NRD-Strip Dimensions: 5*5*70 (a*b*l)
- Ground plane Dimensions:5*20*70 (t*w*l)

where 't' is the thickness of the ground and 'l' is length of the NRD guide. Table 2 below gives the simulated position and sizes of the WR28.

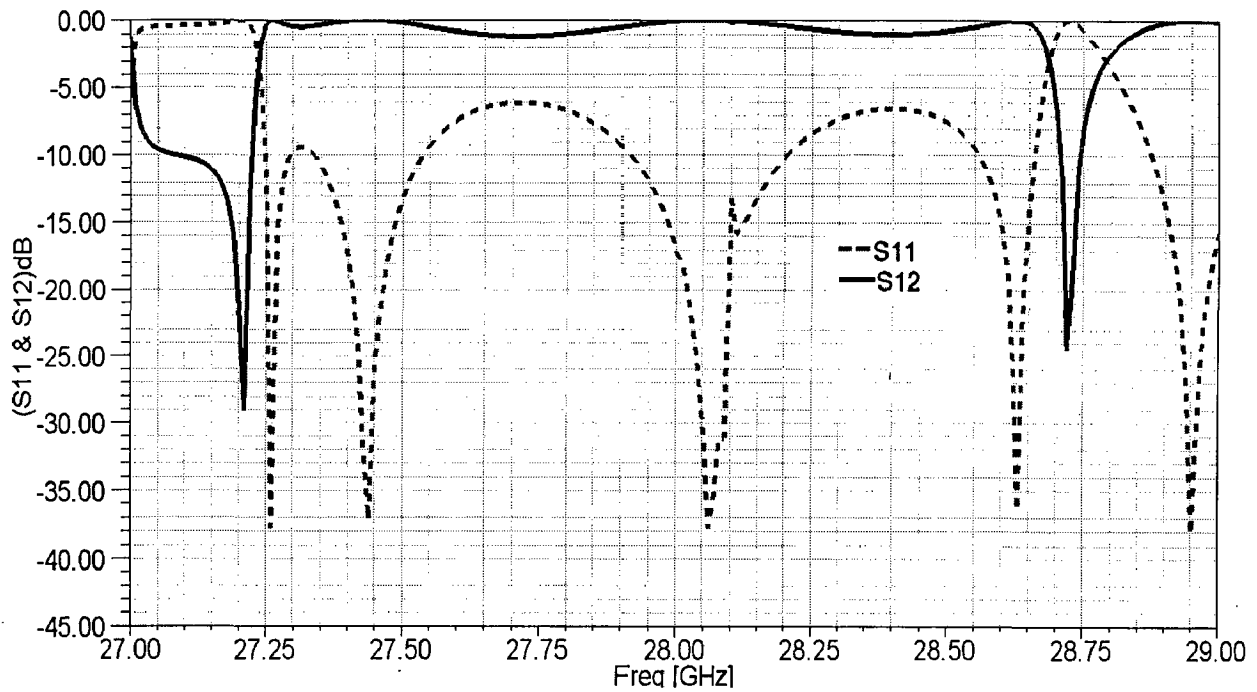


Figure 2.04: S_{11} and S_{12} response for the design of Figure 2.02.

Table 2: HFSS CreatBox command values for WR28, used in the simulation of design, given in Figure 2.02.

WR28	Position	XSize	YSize	ZSize
1	20.9,-1.78,2.5	7.11	3.56	5
2	-20.9,-1.78,-2.5	-7.11	3.56	-5

Although we got desired response, close to 1-GHz BW around 28 GHz, from 27.25 GHz to 28.75 GHz, but the insertion loss (IL) was not constant in the BW. At some regions of the desired BW, say at 27.75 and 28.4 GHz, the IL value was around 1-2 dB.

2.2 NRD Guide to WR Transition using horn antenna

This transition has been simulated in order to overcome the larger IL in the WR28-NRD guide transition and to attain the larger bandwidth (BW) range of testing. This transition geometry is based on [23]. Brief discussion of this type of transition is provided in section 1.3. This section covers the design of horn antenna along with simulation results and discussion on the simulated structure.

2.2.1 Horn Antenna Design

Horn antennas are extremely popular in the microwave region above about 1GHz. Horns provide high gain, low VSWR, relatively wide BW, low weight and are rather easy to construct. Vast amount of literature is available [53], [54] for design, for different specifications and types of horn antenna. Illiout [54] also gives handy 'Horn antenna' scale, from which optimum gain can be obtained by either checking aperture width, length or even height.

However, in the current problem, we need a horn antenna, whose flare is in E plane and taper in H plane. Thus, only two parameters are left to be optimized and that is length and width of the flare section. Horn is fed either by WR28 or WR34. Further, direct application of the design equations, doesn't fulfill our requirement. Even customized tool like Ansoft-Antenna kit [48] and Antenna Magus [49] are not efficient in giving the required physical dimensions, *i.e.*, flare length and flare width. In fact, these tools provide accurate results for known and standard antennas and not for the customized antennas, like in current scenario. Figure 2.06 gives the return loss of the customized horn antenna used in this transition. Although the return loss is not acceptable but due to the taper section of the dielectric slab, there is an efficient transfer of power from the feeding WR to NRD guide. The taper length is almost same as that of the flare section and, therefore, taper's tip reaches the feeding WR and EM fields from the feeding WR confront minimal reflection at the tapered surface, thus, efficient power coupling take place to NRD guide from WR.

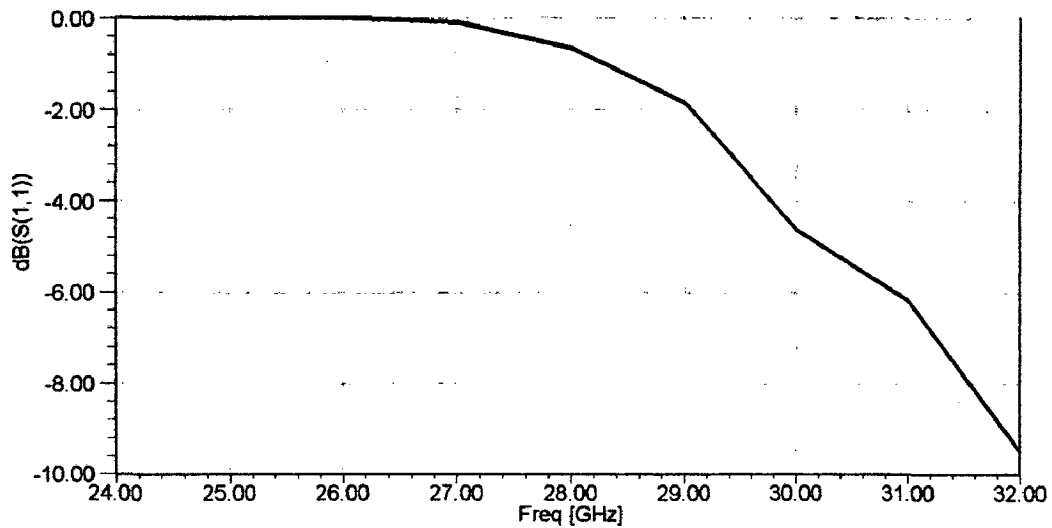


Figure 2.06 Return loss of the horn antenna used for tapered dielectric NRD guide transition.

Next simulate the overall transition was carried out by having random choice of these physical dimensions and employing E plane taper of dielectric strip extending in the flare section of the horn antenna. Some of the simulations used both E-H plane taper of the dielectric strip as shown below, Figure 2.07. Simulation is also carried out by changing the feeding WR between WR28 or WR34. In all these simulations, the results were almost same, minor variation noticed in BW or in IL.

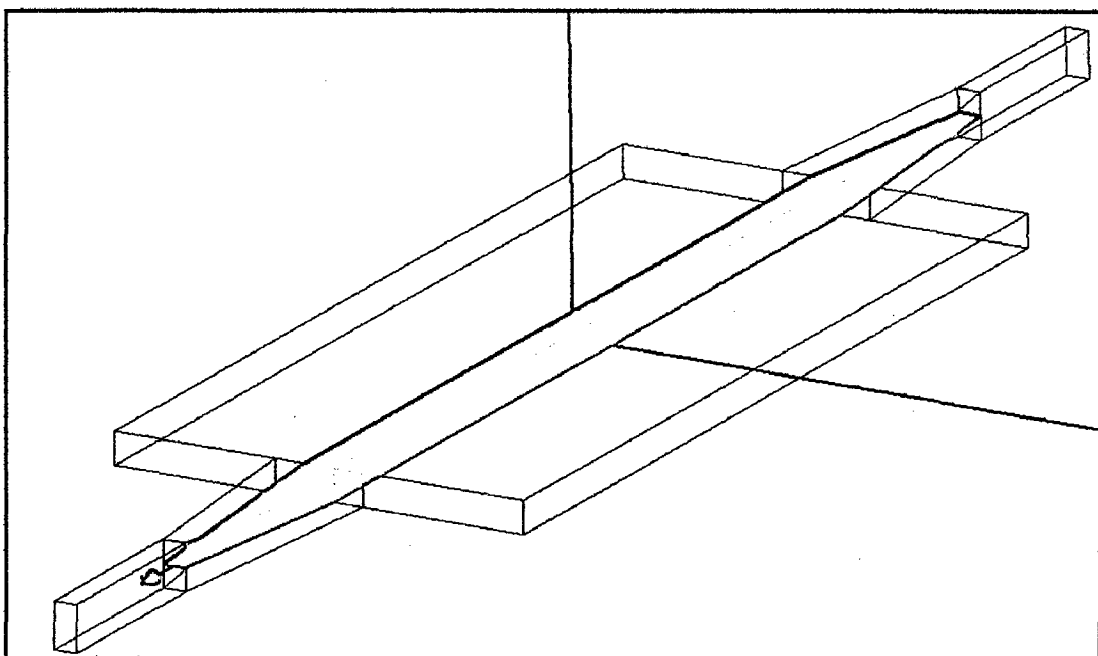


Figure 2.07: Horn antenna-NRD guide transition with E-H plane taper of dielectric strip.

2.2.2 Simulation Setup for NRD Guide to WR Transition using Horn Antenna

Table 3 gives the simulated physical value for the design in Figure 2.07. Horn is fed by WR28. In the table, under taper details, 'end_wd' is along Y axis and 'end_ht' along Z axis. The randomly chosen values are under flare details. One can try some other values too!!!!

Table 3: Physical values of various dimensions in figure 2.15.

Dielectric strip(ht*wd*len)	Total metal width(5mm thick)	Taper details				Flare details	
		Plane	len	end_wd	end_ht	len	wd
5*5*140	65	EH	40	3.4	0.2	40	14

2.2.3 Response of the NRD Guide to WR Transition using Horn Antenna

Figure 2.08 shows the simulated response of the horn antenna-NRD guide transition. It can be inferred from this response that the transition exhibits very wide band response from (sharp cut off at) 25 GHz to 50 GHz, total BW of 25 GHz. Throughout the BW, the return loss is greater than 10dB, insertion loss is close to 1dB till 45 GHz after which it gradually increases and after 50 GHz it mixes with return loss. Cut off can be seen at 25 GHz, frequency at which LSM₁₁ starts propagating.

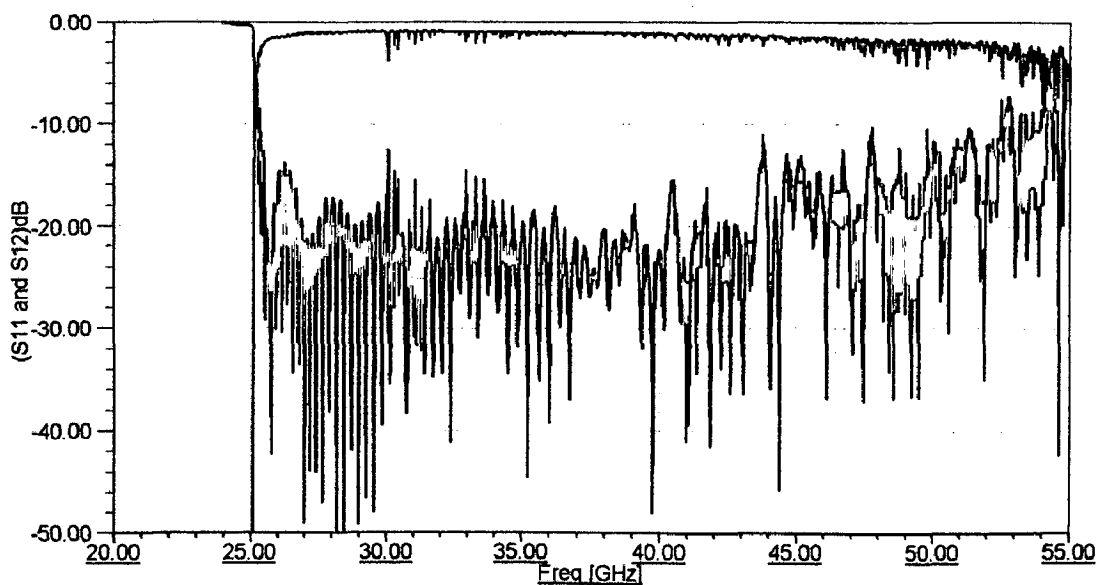


Figure 2.08: S₁₁ and S₁₂ response for the proposed transition shown in Figure 2.07.

Having discussed the NRD guide transition to standard WR either by using vertical WG or horn antenna we now move on to discuss the passive circuits design, in particular, BPF and BSF. Design topology used here is based on SIR and spurline. We first brief the basics, unique properties and useful results of SIR and then elaborate the design steps for filter design. Whereas for spurline design, its parameter effects on filter response is obtained by performing the parameteric variation using the 3D EM solvers.

2.3 Stepped Impedance Resonators (SIR) Basics

Before exploring SIR, we will try to understand UIR (Uniform Impedance Resonators). A strip conductor of uniform width and an overall length equivalent to half wavelength, formed on a dielectric substrate. This structure can be expressed in electrical parameters as a transmission line possessing uniform characteristic impedance with an electrical length of θ radians. Such transmission line resonator will be referred to as uniform impedance resonator (UIR) [55]. In practical design, however, such resonators have a number of disadvantages, such as limited design parameters due to their simple design. Moreover, they exhibit spurious responses at integer multiples of the fundamental resonance frequency. Yamashita [55] illustrates that it is unnecessary to obtain uniform characteristics impedance of a transmission line resonator and that resonator circuit performance can be realized through non-uniform impedance resonators (Stepped impedance resonator: SIR). This is the basic structure and concept of the SIR.

Typical features of an SIR include:

1. A wide degree of freedom in structure and design.
2. A wide range of applicable frequency through use of various types of transmission lines and/or dielectric materials.
3. Derivation of a generalized concept for transmission line resonators including UIR.
4. Development of an expanded concept for non-uniform impedance resonators adopting advanced transmission line structures and composite materials.



The SIR is a TEM or Quasi TEM mode resonator composed of more than two transmission lines with different characteristic impedances. Figure 2.09 shows typical examples of its structural variation, where figure (a) and (b) are examples of $\lambda_g/4$ and $\lambda_g/2$ resonators, respectively.

An electrical parameter which characterizes the SIR is the ratio of the two transmission line impedances Z_1 and Z_2 and this impedance ratio is defined as $R_z = Z_2 / Z_1$. Using this ratio, SIR resonator length and corresponding spurious (unwanted) resonance frequencies can be adjusted.

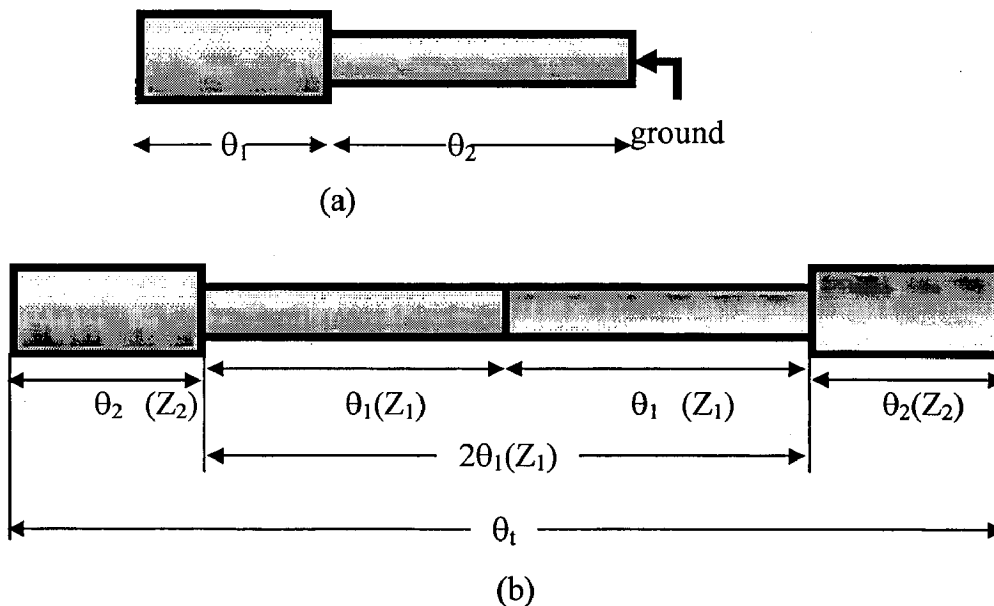


Figure 2.09: Basic types of SIR (a) Quarter wavelength, Single open ended type-Fundamental structural element of any SIR (b) Half wavelength, Double open ended type.

2.3.1 Characteristics of SIR

In this section we will discuss resonance, spurious response and susceptance slope properties of SIR structure.

2.3.1.1 Resonance Condition

The input impedance and the admittance are defined as Z_i and $Y_i (=1/Z_i)$, respectively. When ignoring the influence of step discontinuity and edge capacitance at the open end, Y_i can be expressed as follows, as seen from the open end for Figure 2.09:

$$Y_i = j2Y_2(R_z \tan\theta_1 + \tan\theta_2)(R_z - \tan\theta_1 \tan\theta_2) / (R_z(1 - \tan^2\theta_1)(1 - \tan^2\theta_2) - 2(1 - R_z^2) \tan\theta_1 \tan\theta_2) \quad (1)$$

Resonance conditions are obtained by taking $Y_i=0$, which gives

$$R_z = Z_2/Z_1 = \tan\theta_1 \tan\theta_2 \quad (2)$$

Eqn (2) is common for all SIR structures. In case $\theta_1 = \theta_2 = \theta_0$, resonance conditions are expressed as

$$\theta_0 = \tan^{-1} \sqrt{R_z} \quad (3)$$

2.3.1.2 Spurious Response

Spurious responses of a $\lambda_g/2$ type SIR become more critical compared with $\lambda_g/4$ type SIR [56]. This requires the designer to consider the spurious responses of higher resonance modes which otherwise would be neglected for $\lambda_g/4$ type SIR. By expressing the spurious resonance frequencies as f_{SB1} , f_{SB2} , f_{SB3} and corresponding θ 's as θ_{SB1} , θ_{SB2} , θ_{SB3} we obtain from (1), for the case of $\theta_1 = \theta_2 = \theta_0$,

$$Y_i = j2Y_2(R_z+1)(R_z - \tan^2\theta_0) \tan\theta_0 / (R_z(1 - \tan^2\theta_0)(1 - \tan^2\theta_0) - 2(1 - R_z^2) \tan^2\theta_0) \quad (4a)$$

$$= j2Y_2(R_z+1)(R_z - \tan^2\theta_0) \tan\theta_0 / (R_z - 2(1 + R_z - R_z^2) \tan\theta_0 + R_z \tan^4\theta_0) \quad (4b)$$

Now, by equating (4) to zero, we get

$$\theta_{SB1} = \pi/2, \quad (\text{By making denominator to infinity}) \quad (5a)$$

$$\theta_{SB2} = \tan^{-1}(-\sqrt{R_z}) = \pi - \theta_0, \quad (\text{By equating "R}_z - \tan^2\theta_0" \text{ argument to zero}) \quad (5b)$$

$$\theta_{SB3}=\pi \quad (\text{By equating "tan}\theta_0\text{" argument to zero}) \quad (5c)$$

From these we have,

$$f_{SB1}/f_0 = \theta_{SB1}/\theta_0 = \pi/(2 \tan^{-1}(\sqrt{R_z})), \quad (6a)$$

$$f_{SB2}/f_0 = \theta_{SB2}/\theta_0 = 2(f_{SB1}/f_0) - 1, \quad (6b)$$

$$f_{SB3}/f_0 = \theta_{SB3}/\theta_0 = 2(f_{SB1}/f_0) \quad (6c)$$

Generally, the fundamental and the spurious frequencies should be as far apart as possible.

2.3.1.3 Susceptance Slope Parameter

Another important property of any resonator is slope parameter [57]. For any resonator involving a shunt-type resonator, the susceptance slope parameter can be expressed as

$$b = \omega_0/2(dB/d\omega) \text{ at } \omega = \omega_0 \quad (7)$$

where B is the susceptance of the resonator. For the SIR considered here Eqn (7) becomes

$$b = \theta_0/2(dB/d\theta) \text{ at } \theta = \theta_0 \quad (8)$$

Using 4(b), Eqn 8 becomes $b = 2\theta_0 Y_2$ (9)

2.3.2 BPF Based on CSIR (Coupled SIR)

Any design based on SIR will definitely have the coupled input and output sections for the energy transfer. So is the case of band pass filter implemented here; it consists of coupled line section in order to tune the response of the BPF. Following are the specifications of CSIR Based BPF:

Center frequency = 28 GHz,

3dB Pass band BW = 0.5 GHz,

Pass band ripple/Attenuation in pass band = 0.01 dB,

System impedance = 50 Ω ,

Stop band BW = 4 GHz,

Stop band attenuation/Attenuation at stop band frequencies = 45 dB,

Spurious frequency multiplier = 2.5 (This gives spurious response as the product of the center frequency and the spurious frequency multiplier)

Design equations for BPF are modeled in Mathworks MATLAB v7 [49] and given in the Appendix A. It follows the procedure given in [55], but we have to be careful when using it for any other transmission line other than stripline. Procedure given in [55] is applicable to stripline technology, in the sense that it will provide the final physical parameters in terms of length, spacing and width, which will be used in the simulations for verifying its response.

But when this procedure or Matlab code is used for transmission lines other than stripline, say microstrip technology, then we have to discard the final physical parameters of the procedure/code and safely note down the Z_{0e} and Z_{0o} values for each section in the filter design. Use these value in Agilent ADS 2008 tool's [50] Line Calc application (Figure 2.10) to get final physical parameters in terms of length, spacing and width, to be used in the simulations. In ADS Line Calc application, select the component type as coupled microstrip line and punch in the impedance values from the procedure/code.

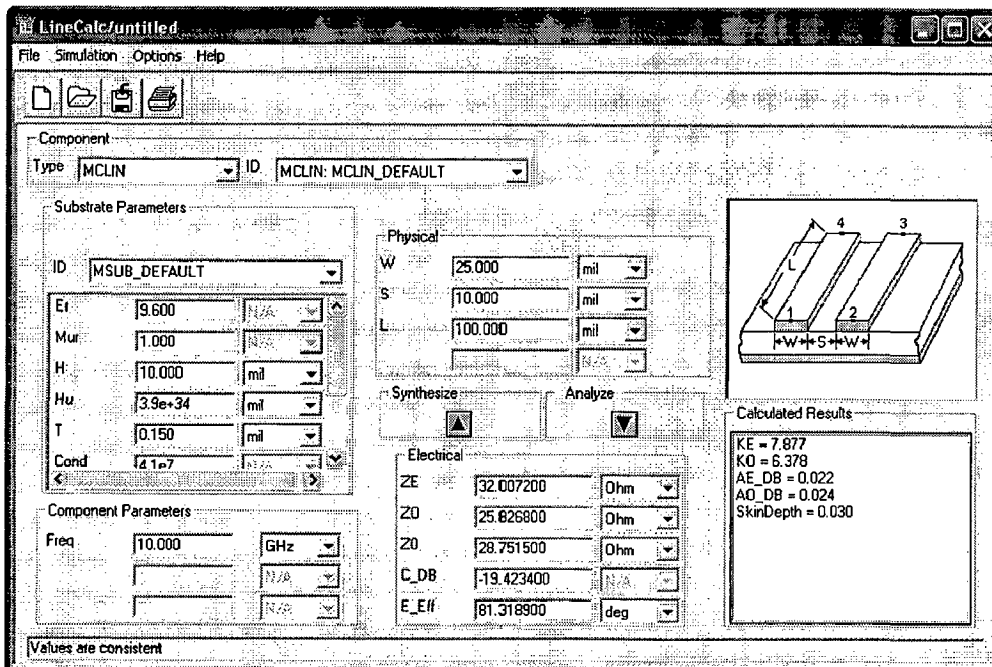


Figure 2.10: Agilent ADS 2008 Line Calc application- An illustration.



The MATLAB v7 [49] code can be divided in following stages, although the final output of the code in our case gives only the even and the odd mode impedances. These stages are the internal demarcations of the code for easy readability.

Stage 1: Pre-computational parameters.

This stage includes:

- (i) Transformation of the specified frequency to prototype LPF [52].
- (ii) Finding the Order/Number of SIR stages in the filter design.
- (iii) Finding the Chebyshev response parameters for filter designs.

Stage 2: Computation of g parameter values.

This stage calculates the g parameter (inductance-capacitance) values using the insertion loss method [52].

Stage 3: Computation of SIR design's required parameter.

This stages includes

- (i) Relative Bandwidth calculation W_{rel} .

Relative Bandwidth=2*pass band BW/center frequency

- (ii) Insertion loss calculation at the center frequency.

$L_0 = (4.343/Relative\ Bandwidth) * \text{Summation of all } g \text{ parameters excluding the first and the last } g \text{ parameter}$

- (iii) Impedance ratio calculation using Eqn 6(a) for the given spurious frequency multiplier in the specification.

- (iv) Finding the impedance values (Z_1, Z_2) for individual SIR's (based on the order calculated above) from the above impedance ratio, assuming impedance of the end section to be same as that of the system impedance.

$$R_z = Z_2/Z_1 \quad (1a)$$

$$Z_1 = Z_2(=System\ impedance)/R_z \quad (1b)$$

- (v) Finding the electrical length parameter (θ_0) from the impedance ratio.

$$\theta_0 = \tan^{-1} \sqrt{R_z} \quad (2)$$

(vi) Finding the susceptance slope parameter for the filter, using Eqn (9)

$$b_0 = 2\theta_0 Y_2 \quad (3)$$

Stage 4: Calculation of inverter parameter.

The admittance inverter parameters $J_{j,j+1}$ are given by following formulae

$$J_{01} = \sqrt{(Y_0 b_0 W_{rel} / g_0 g_1)} \quad (4a)$$

$$J_{nn+1} = \sqrt{(Y_0 b_0 W_{rel} / g_n g_{n+1})} \quad (4b)$$

$$J_{jj+1} = W_{rel} * \sqrt{(b_j b_{j+1} / g_0 g_1)} \text{ for SIR sections } j=1 \text{ to } (\text{order}-1). \text{ Here } b_j = b_{j+1} = b_0. \quad (4c)$$

Stage 5: Calculation of even and odd mode impedances.

This snippet makes use of below formulae to find Z_{0e} and Z_{0o} .

$$Z_{0e} = Z_0 * (1 + J * Z_0 * \operatorname{cosec}(\theta_0) + (J * Z_0)^2) / (1 - (J * Z_0 * \cot(\theta_0))^2) \quad (5a)$$

$$Z_{0o} = Z_0 * (1 - J * Z_0 * \operatorname{cosec}(\theta_0) + (J * Z_0)^2) / (1 - (J * Z_0 * \cot(\theta_0))^2) \quad (5b)$$

As mentioned above, if this code used for technology other than stripline, then we have to calculate only the even and the odd impedances and make use of ADS Line Calc utility. For the completeness sake, the last and final stage is explained below, which is important only for the stripline design.

Stage 6: Calculation of physical parameters of the design.

This stage finds:

- (i) the length of each section using $\theta_0 = \beta_g l$ and including the effect of the fringing effect due to discontinuity.
- (ii) the width of single and coupled section line and spacing of coupled section line using following formulae;

$$\text{for single section line} \quad Z_0 = 30 * \pi / (\sqrt{\epsilon_r} ((W/H) + 2 \ln 2 / \pi)) \quad (6a)$$

for coupled section line

$$Z_{0e} = 30 * \pi / \sqrt{\epsilon_r} ((W/H) + \ln 2 / \pi + \ln(1 + \tanh(\pi S / 2H)) / \pi) \quad (6b)$$

$$Z_{0o} = 30 * \pi / \sqrt{\epsilon_r} * (\ln(2/\pi) + \ln(1 + \coth(\pi S/2H))) / \pi \quad (6c)$$

where W and S are the width and the spacing of coupled line section.

The Matlab code takes the above said specifications as the input and provide us the even and the odd mode impedances (or physical parameters in the case of stripline technology). Table 4 gives the even and the odd mode impedances for 5 coupled line sections in an 4th order filter.

Table 4: Output of MATLAB code for CSIR based BPF, for specified requirements.

Mode Impedances	Coupled sections for order 4 filter				
	1	2	3	4	5
Even	85	55	53	55	85
Odd	36	46	47	46	36

After synthesizing the physical parameters from ADS Line Calc, we created a 2D model of the CSIR based BPF. Results of the design are then improved through manual tuning and ADS optimization algorithms. Some of the algorithms which have been used were Random, Gradient Minimax, Simulated Annealing and Genetic. In most of the simulations, Gradient Minimax was used.

Final layout is shown in Figure 2.11 and its reflected and transmitted power response in Figure 2.12. CSIR based BPF was fabricated, as shown in Figure 2.13, in order to have feel about the level of miniaturization, reached, at milli-meter wave frequencies. Certain fabrication errors were found due to very small dimensions. Here, the substrate used is having dielectric constant of 2.2 and thickness of 10 mil (or 0.254 mm).

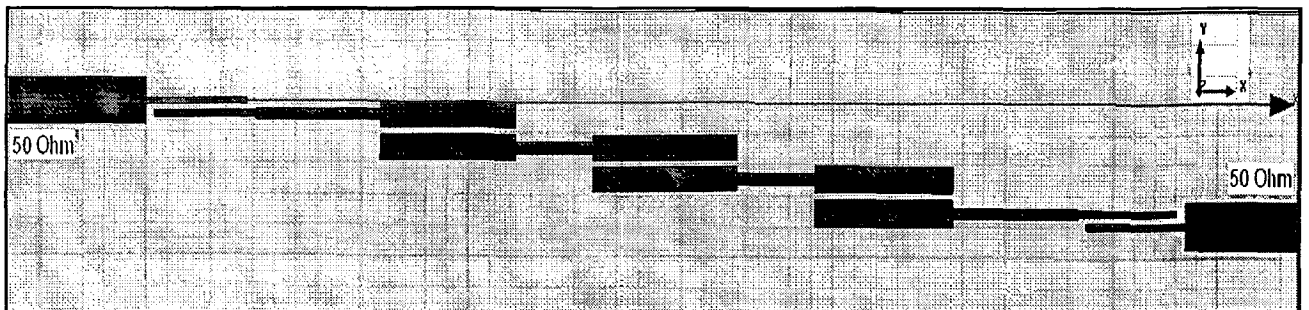


Figure 2.11: CSIR BPF for 28 GHz with 3dB BW of 3.4 GHz.

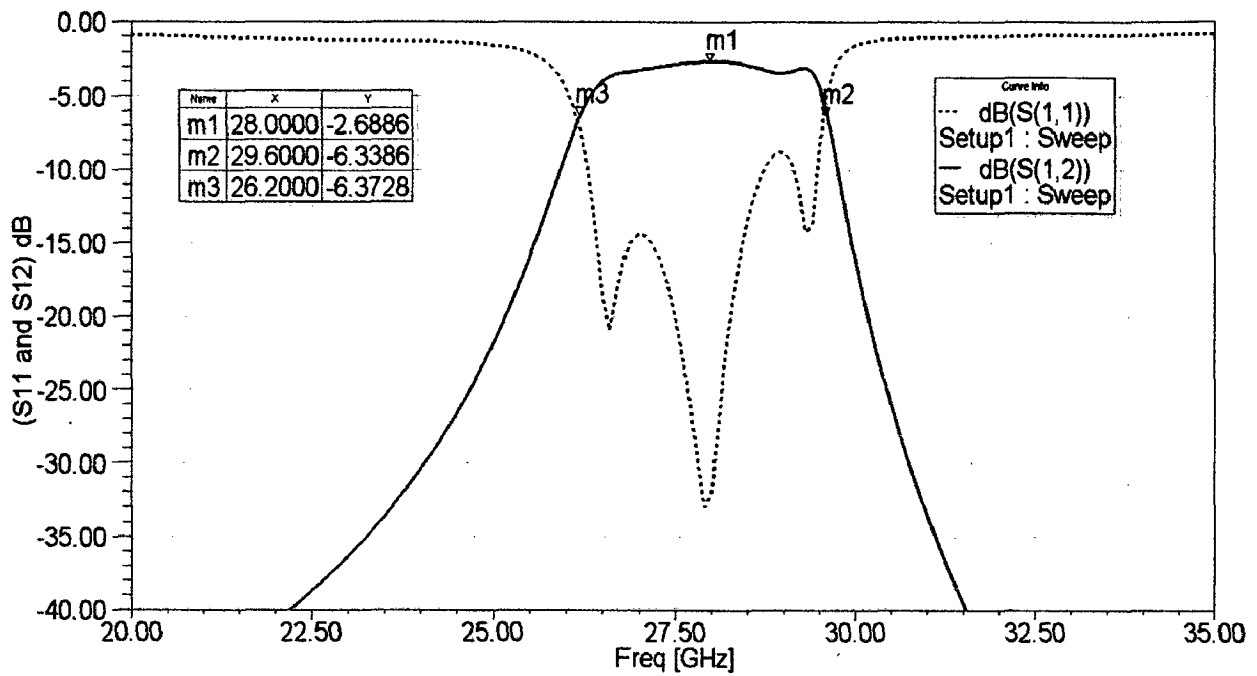


Figure 2.12: S_{11} & S_{12} response of CSIR BPF in Figure 2.11.

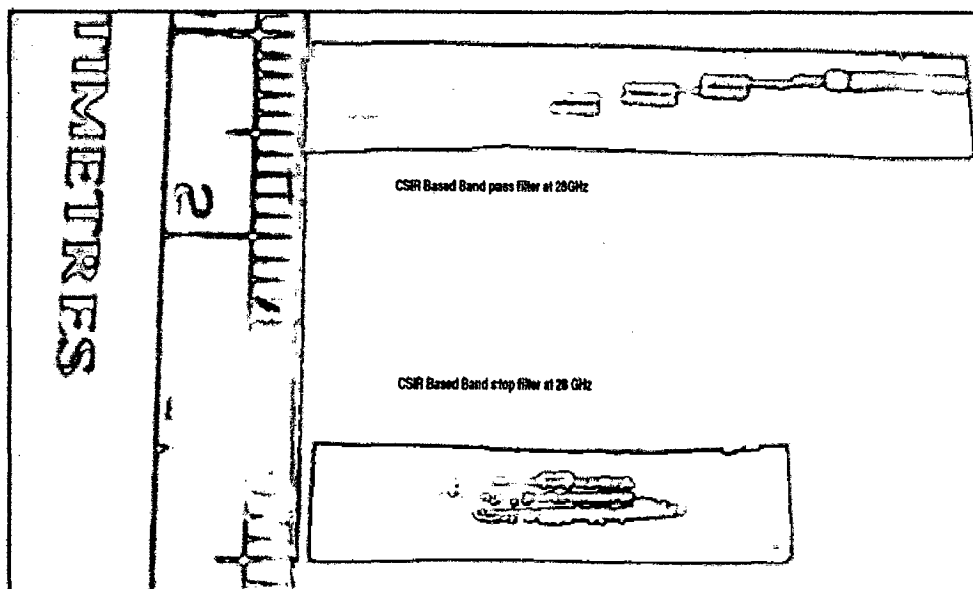


Figure 2.13: Fabricated CSIR based BPF and BSF using wet etching technology.

Figure 2.14 shows the spurious frequency response of BPF. One can see that spurious frequency is far away from the fundamental one because of the impedance ratio (R_z) of 2.5 which we have specified in the requirements of the BPF. Thus, it illustrates the flexibility of the SIR to position the spurious frequency, as mentioned in the beginning of this chapter.

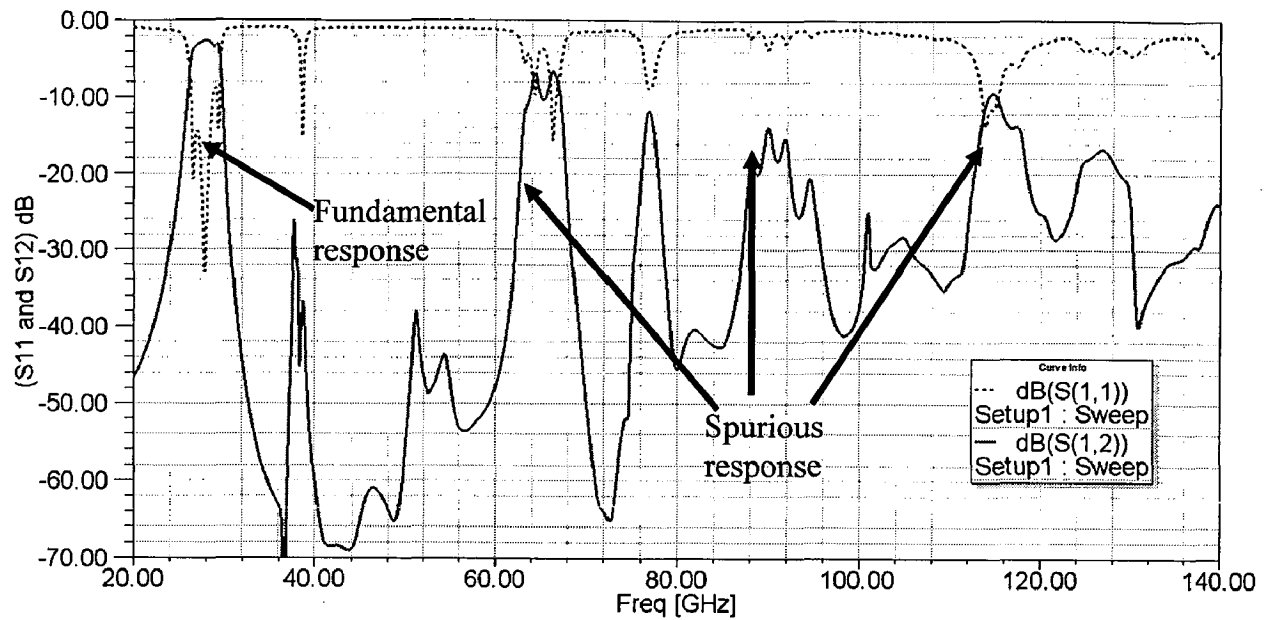


Figure 2.14: Spurious frequency response of CSIR based BPF.

Figure 2.15 is the simulation result of group delay of the filter which is less than 0.75ns in the entire pass band. Within the pass band (3dB BW from 26.2 to 29.6 from Figure 2.14) the predicted group delay is less than 0.33ns with the maximum variation of about 0.4ns, thereby, implying good linearity of this proposed BPF.

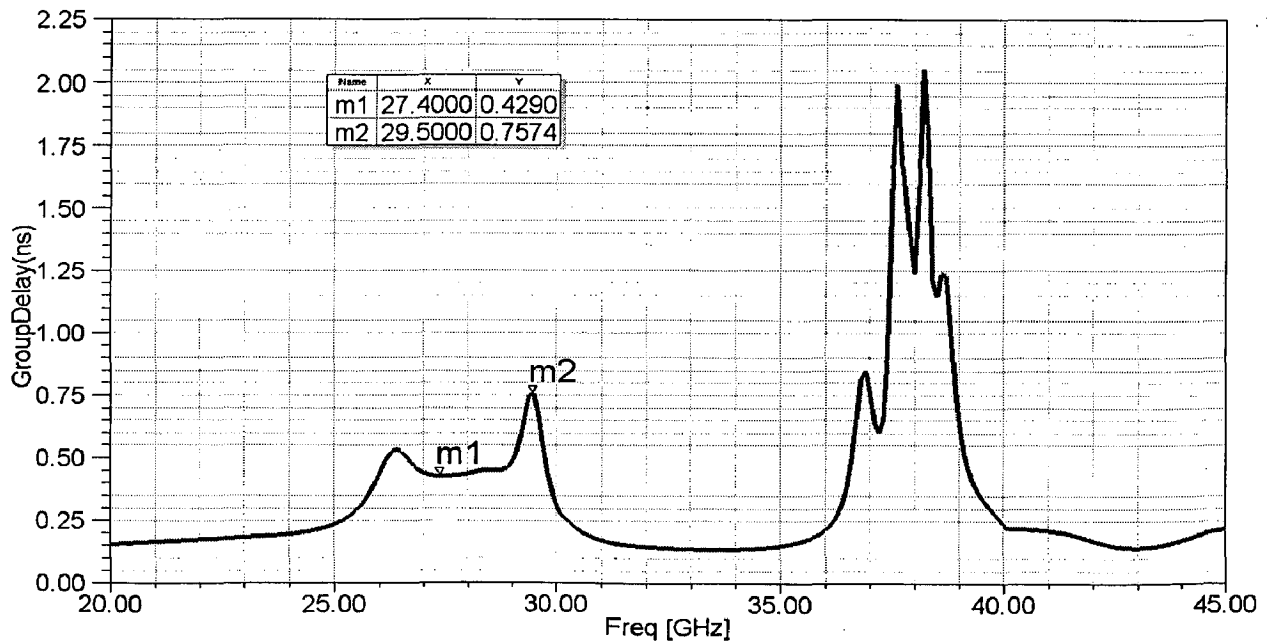


Figure 2.15: Group delay response of CSIR based BPF.

2.3.3 BSF Based on CSIR

Before analyzing the simulated results of BSF, we will brief about the basics required for the design of CSIR based BSF.

The input impedance of SIR from Figure 2.09(b) can be written as

$$Z_i = jZ_1 \frac{(1 + R_z + R_z^2) \tan \theta_0 - R_z}{\tan \theta_0 (2R_z + R_z^2 - \tan^2 \theta_0)} \quad (1)$$

As said previously, the resonance condition can be obtained by setting $Z_i = 0$. Using this, the electrical length θ_0 at the fundamental frequency f_0 can be determined by setting numerator to zero. Therefore, one gets:

$$\theta_0 = \tan^{-1} \sqrt{K / (1 + R_z + R_z^2)} \quad (2)$$

2.3.3.1 Spurious Response

Following the same process as in BPF, spurious resonance frequency in BSF is obtained by setting condition on RHS of (1) such that $Z_i = 0$. We have then,

$$\theta_{s1} = \pi/2 \quad (\text{By setting numerator to zero in (1)}) \quad (3)$$

$$\theta_{s2} = \pi - \theta_0 \quad (4)$$

Eqn. (4) is due to the fact that it cannot be same as θ_0 as it is a fundamental response. Therefore $\theta_{s2} + \theta_0 = \pi$, and hence, we have

$$f_{s1}/f_0 = \theta_{s1}/\theta_0 \quad (5)$$

$$f_{s2}/f_0 = \theta_{s2}/\theta_0 \quad (6)$$

2.3.3.2 Transmission Pole Response

In contrast to the spurious resonance for $Z_i = 0$, the SIR produces transmission poles ($S_{11} = 0$) when $Z_i = \infty$. By applying the condition $Z_i = \infty$, the electrical length θ_{pn} ($n = 1, 2, 3, \dots$) at the transmission pole frequency f_{pn} ($n = 1, 2, 3, \dots$) can be also derived from Eqn (1). This is done by imposing the term $2R_z + R_z^2 - \tan^2 \theta$. For f_{p1} and f_{p2} , we obtain

$$\theta_{p1} = \tan^{-1} \sqrt{2R_z + R_z^2} \quad (7)$$

$$\theta_{p2} = \pi - \theta_{p1} \quad (8)$$

Therefore,

$$f_{p1}/f_0 = \theta_{p1}/\theta_0 \quad (9)$$

$$f_{p2}/f_0 = \theta_{p2}/\theta_0 \quad (10)$$

2.3.3.3 Design Procedure of CSIR BSF

The design of BSF is based on [58]. The analysis done in this paper is complementary to that done in [55], for the implied reasons.

We have started with initial guess (based on some equations) and later on improved upon these physical values using ADS post processing facility [32] as stated above. For the design shown in Figure 2.16, for both the first and the third SIR sections, we assume Z_2 (from Figure 2.09) as 80 ohms and Z_1 as 20 ohms so that the R_z is 4. And for the middle section, we have chosen the values same as in [58], *i.e.*, $Z_{2m} = 55\Omega$ and $Z_{1m} = 45\Omega$. With these initial start up values, design has been simulated and later on improved upon these physical values using ADS post processing facility [50] as stated above.

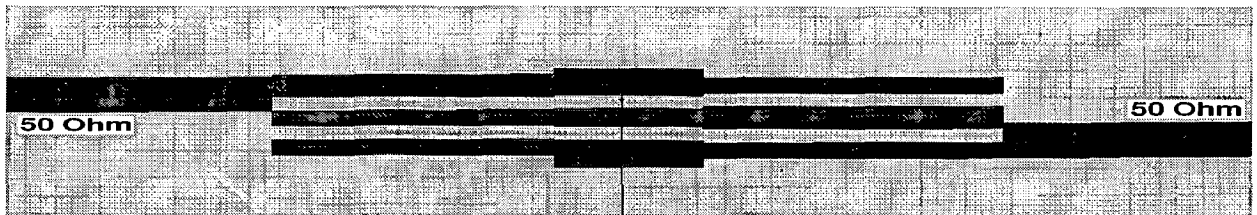


Figure 2.16: CSIR BSF for 28 GHz with 3dB BW of 3.5 GHz.

Final layout is shown in figure 2.16 and its S-parameter response in Figure 2.17. We are able to obtain a flat rejection BW of the order 3.5 GHz. CSIR based BSF is been fabricated with fabrication error due to very small dimensions, but shown here (Figure 2.13)

in order to have feel about the level of miniaturization, reached, at milli-meter wave frequencies.

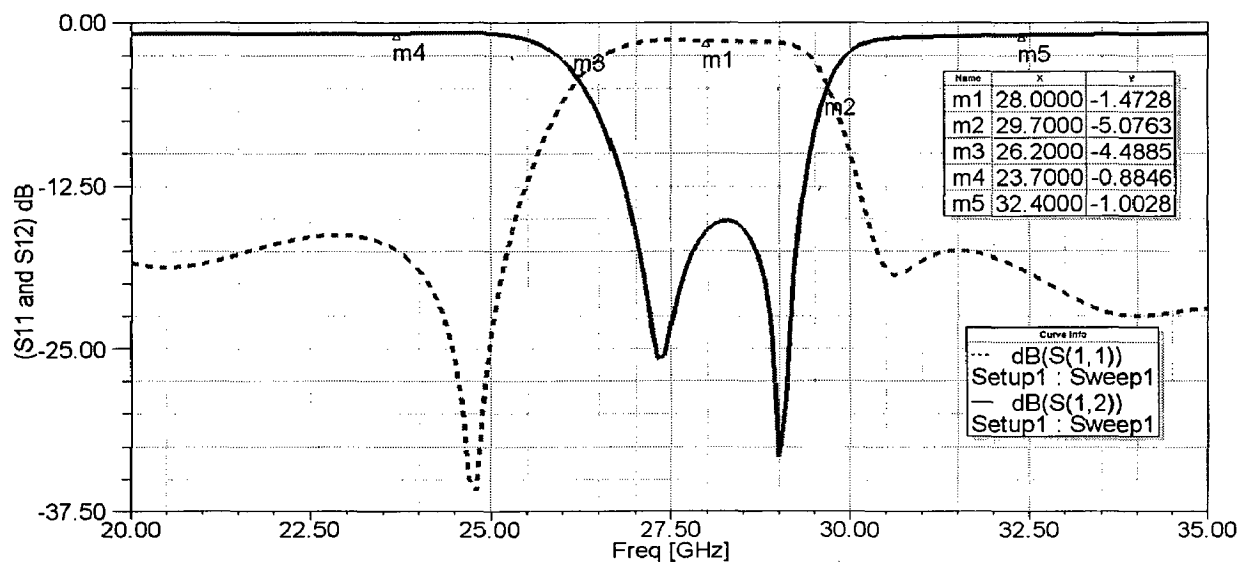


Figure 2.17: S_{11} and S_{12} response of CSIR BSF in Figure 2.16.

Figure 2.18 shows the spurious frequency response of BSF. One can see that spurious frequency is far away from the fundamental one because of the impedance ratio (R_z) being 4 which we have assumed in the requirements of the BPF. Thus, it illustrates the flexibility of SIR to position the spurious frequency, as mentioned in the beginning of this chapter.

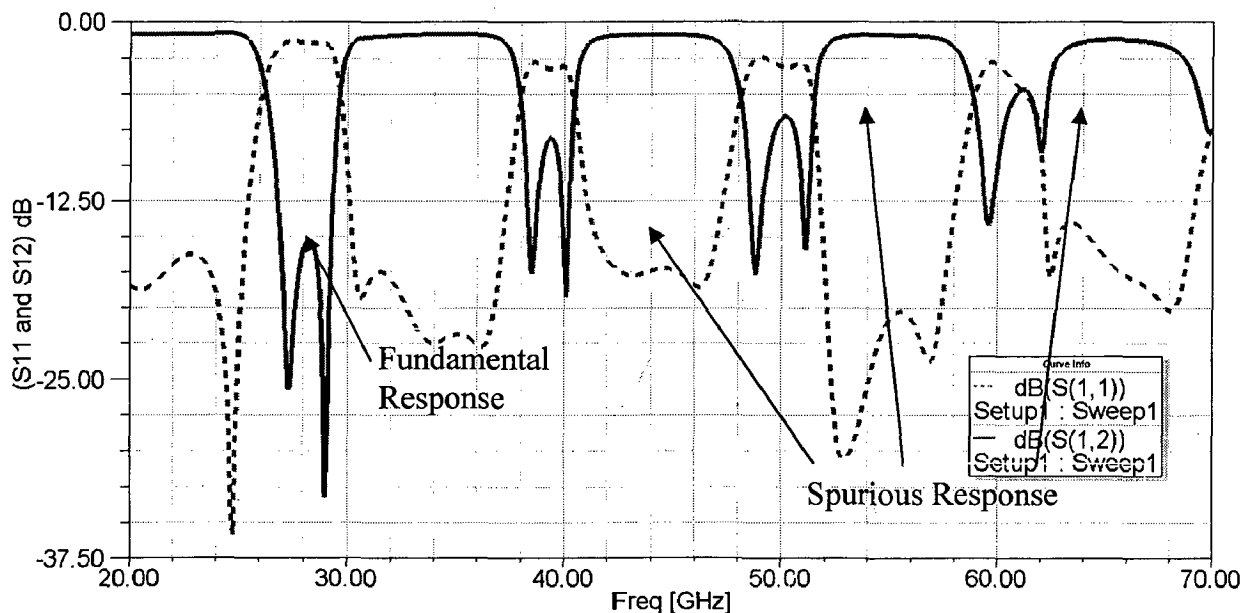


Figure 2.18: Spurious frequency response of CSIR BSF in Figure 2.16.

Figure 2.19 is the simulation of the group delay of the filter which shows a sharp fall at our center frequency of 28 GHz. Group delay is less than 0.3-0.4 ns in the entire pass band.

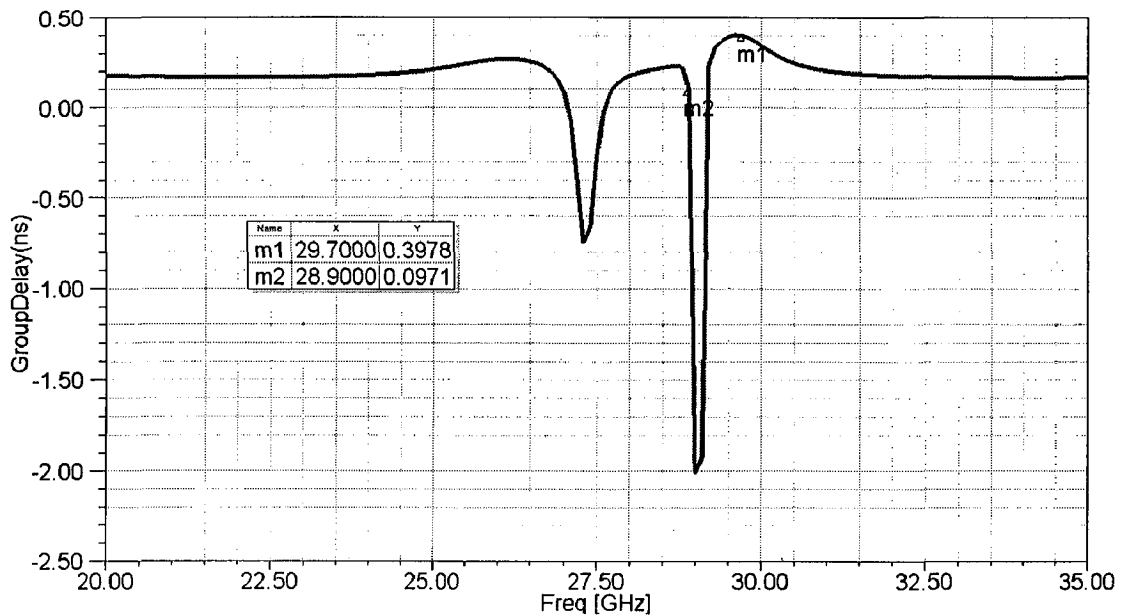


Figure 2.19: Group delay response of CSIR BSF in Figure 2.16

2.4 Effect of variation of spurline parameters on filter response

Spurline is commonly based on microstrip transmission lines with band-stop (notch) characteristics. It is very convenient for dense integrated circuits because of their inherently compact design and ease of integration. Generally, spurline is a simple defected structure, which is realized by etching one L-shape slot on top microstrip line. Without any stubs and etched processing on backside ground plane, it can provide excellent band gap characteristics and can be applied in antenna and filter designs [59]. Basic literature on spurline design is given in [60-61]. Figure 2.20 shows two spurs made (or two slots have been cut) in microstrip technology along with various dimensions that have been locally designated (not given in any literature).

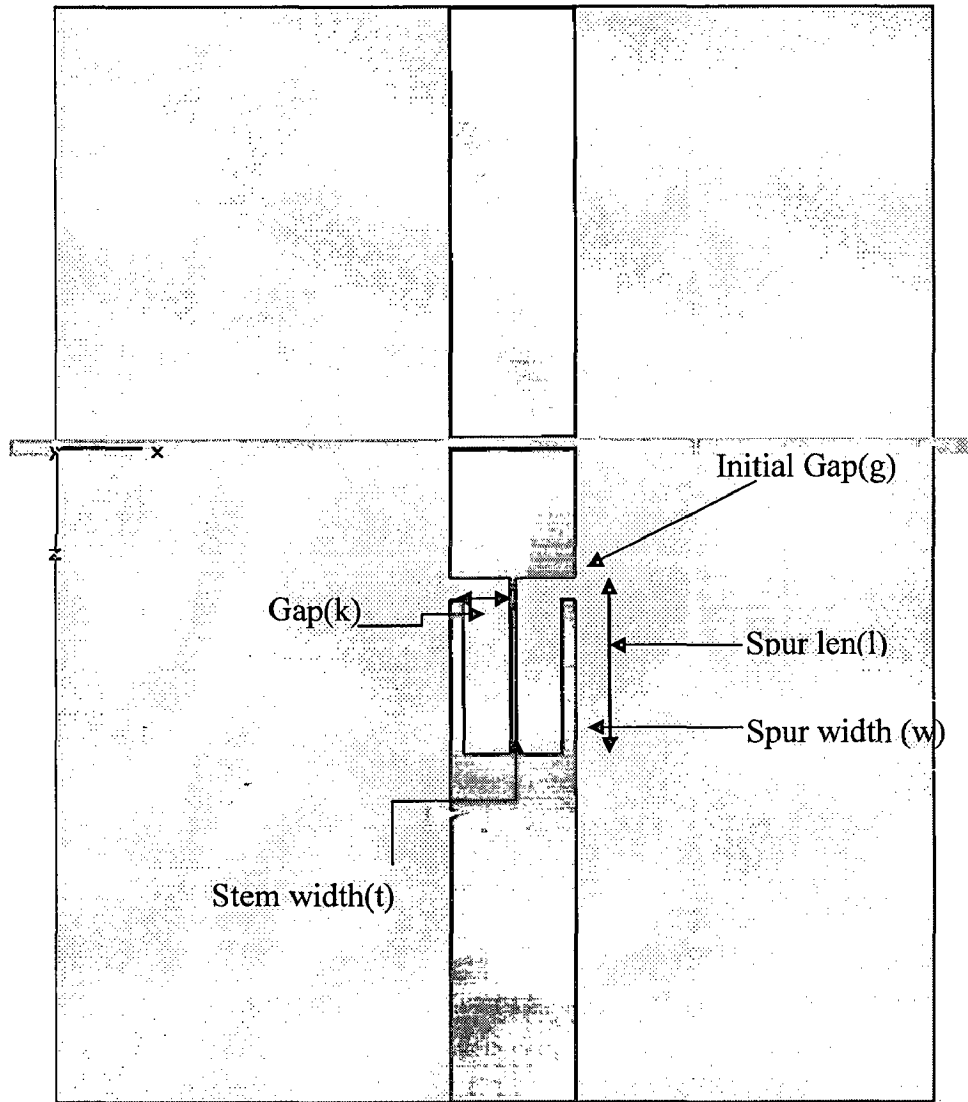


Figure 2.20: Dual spurline with various variables defined for qualitative analysis in table 4. (Pink color is for metallic trace and yellow color is for the substrate)

Table 5 discusses the effect on center frequency (f_c) by varying the dimension shown in Figure 2.20. Various graphs substantiating the results/effects on f_c , in Table 5, are plotted in Figures from 2.21 to 2.25.

Table 5: Depicting the qualitative model of spurline design.

Dimensions varied	Effect on f_c	Other comments
Varying the spur length	Varies the f_c	
Varying the spur width, keeping gap width constant	f_c remains constant	
Varying the position of spur	f_c remains constant	
Varying the gap width, keeping spur width constant	f_c remains constant	3dB BW decreases or response drops as it increases
Varying the stem width	f_c (for each spur) remains constant	

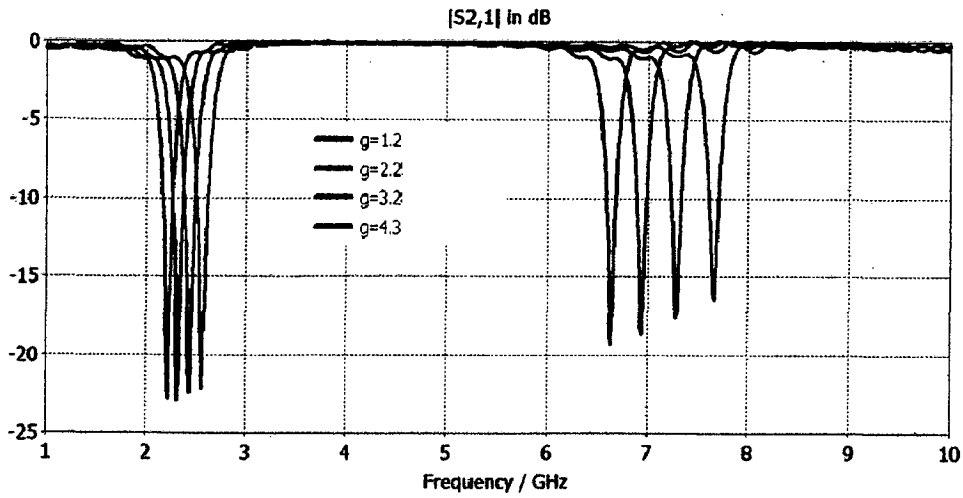


Figure 2.21: Variation in S_{21} with initial gap width/ spur length.

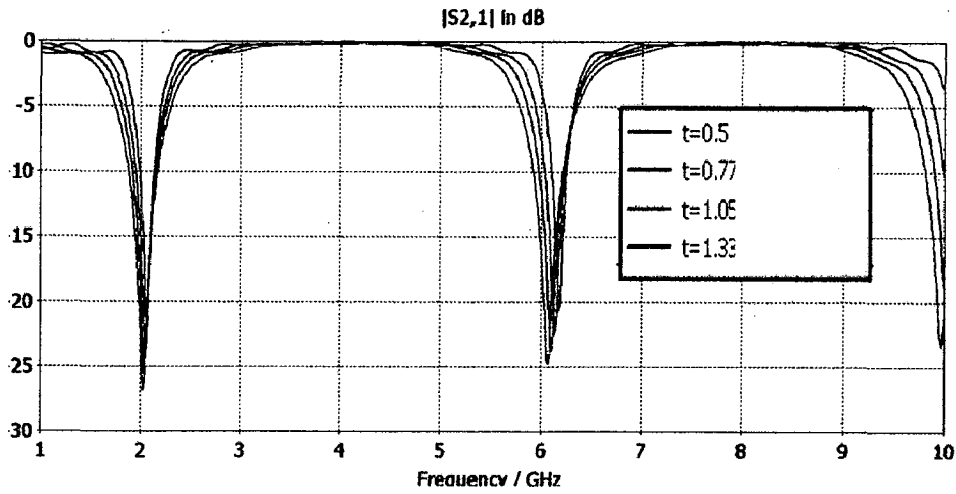


Figure 2.22: Variation in S_{21} with spur width, keeping gap width constant.

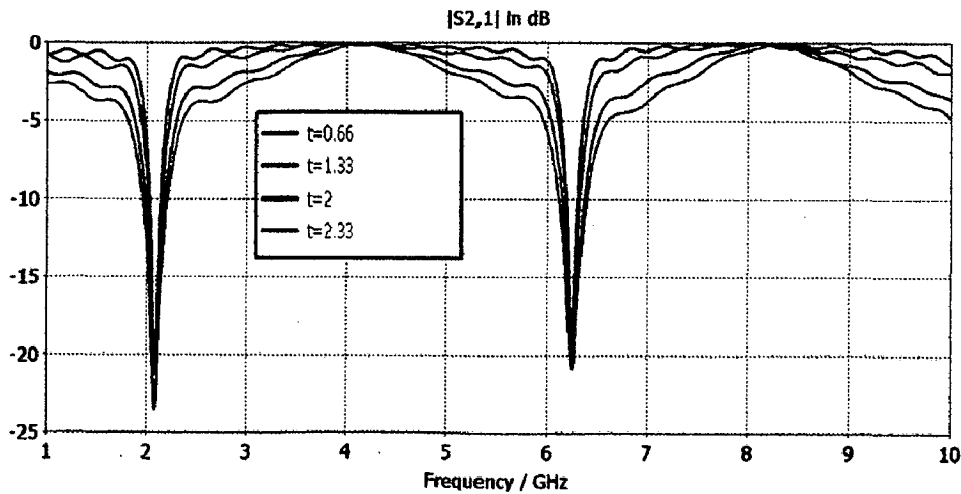


Figure 2.23: Variation in S_{21} with position of spur, keeping spur and gap width constant.



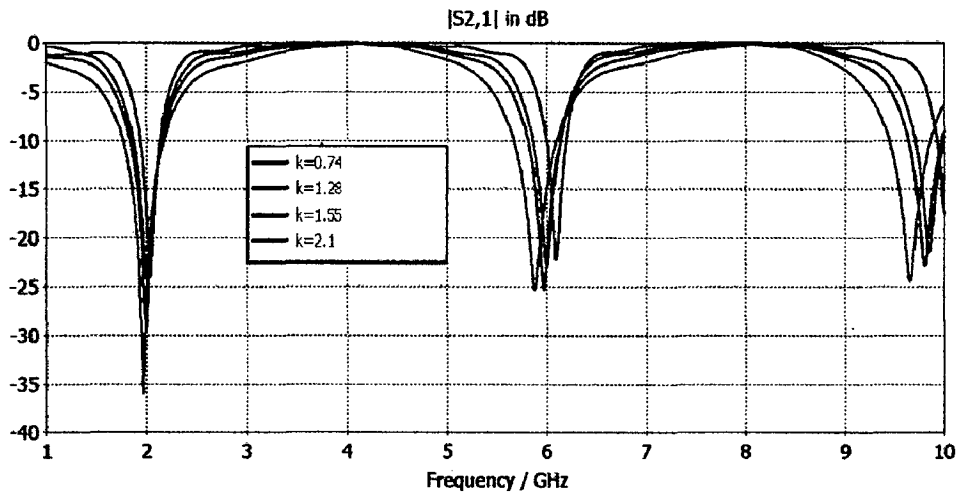


Figure 2.24: Variation in S_{21} with gap width, keeping spur width constant

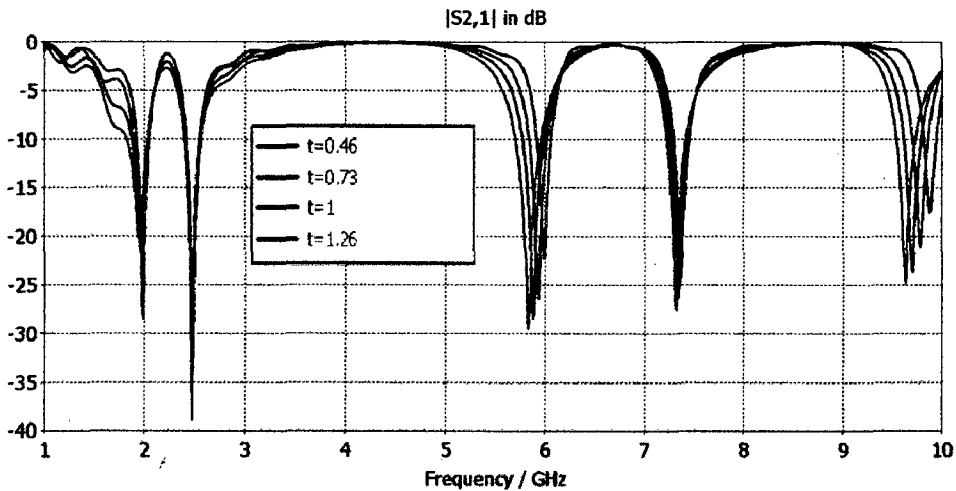


Figure 2.25: Variation in S_{21} with stem width between 2 spurs.

2.5 Conclusion

This chapter has discussed the simulation of NRD guide to WR transition on commercially available EM solver. NRD to WR H plane transition is providing small BW around 28 GHz while NRD to WR horn transition is giving around 25 GHz BW by employing the E plane taper. Then design of BPF and BSF is discussed in SIR and spurline design. SIR based both the filters are giving more than 3 GHz required BW centered around 28 GHz. In the end, effects of different parameters of spurline design on the filter response is studied.

Chapter 3

Slot Plasmonic Waveguide Structures (MIM/MDM)

3.1 Introduction

This chapter focuses on the plasmonics simulations, where in the results and conclusion which have been reported in the literature or which is discussed in chapter 1 is reproduced and compared. These simulations help in understanding the different solver and their settings used for such high frequency applications. Also, it cross verifies our understanding/ concepts related to this colorful field. Most of the papers which are reproduced in this chapter are either fabricated ones or based on pure simulations and they discuss or examine the properties [62] which is briefly touched upon in chapter 1. These properties mainly include dispersion curves, propagation length along the slot, propagation loss and electric field magnitude or intensity plot of SPP propagation.

During these simulations we have used 2 commercial available full wave/3D solvers namely, FEM based HFSSv13 and FIT based CST-MWSv2010. These solvers are used on the basis of reported literature on it and the quantity of results which can be reproduced. Say for example, all simulations using HFSS provide only the field magnitude or intensity plot, and to reproduce other 2D results one has to need more expertise in tool. But simulations dealing with CST-MWS, they are providing the above said *bunch* of results, fairly simple. So the simulations done on CST are giving us more technical insight into the phenomenon of SP than FEM counterpart.

Before cross verifying the simulated results, one needs to solve, simple yet twisted, problem of launching the beam which can excite the SPP in the slot structure. This chapter begins with gathering info on SPP launcher mechanism and then discusses the simulated results.

3.2 SPP launching mechanism

In order to consider integration of subwavelength devices as constituents of dense subwavelength photonic networks, we must find strategies for efficient (low loss) coupling light/exciting beam into guiding structure. The simulated MIM stack consists of a silicon (Si) core (Green in colour), with thin layer of silicon oxide on one side (Red in colour) and clad on both sides of silver(Ag), (Dark Yellow in colour). The simulation is 2D with PML boundaries. Material data is generated using the extended Drude model for the dispersive dielectric of Ag, and is given in Appendix B. The following coupling geometries [63] which are reported in the literature;

- a) Slit coupling: In this a deep cut is made from clad, oxide and half of silicon layer and Gaussian beam is irradiated in this cut, shown in red cross arrows Figure 3.01(a).

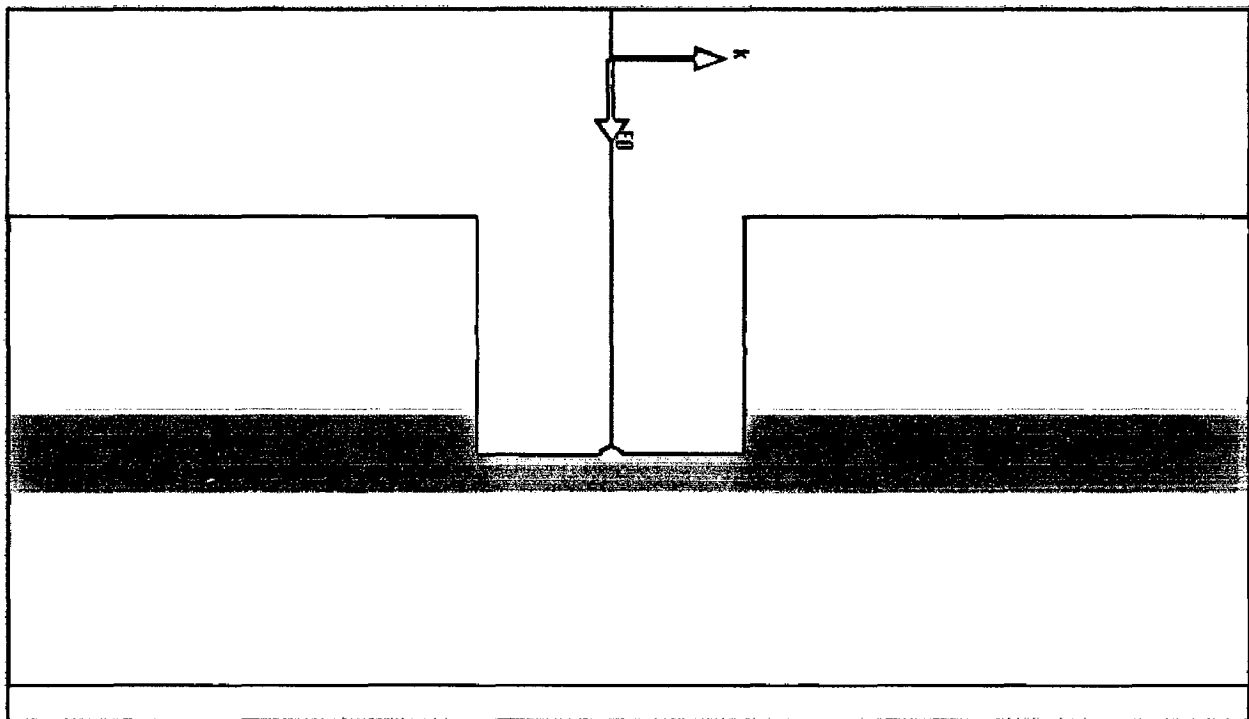


Figure 3.01 (a) Slit layout

- b) Endfire coupling: Source plane is a Gaussian beam incident normal to the end facet of a truncated MIM Figure 3.01(b).

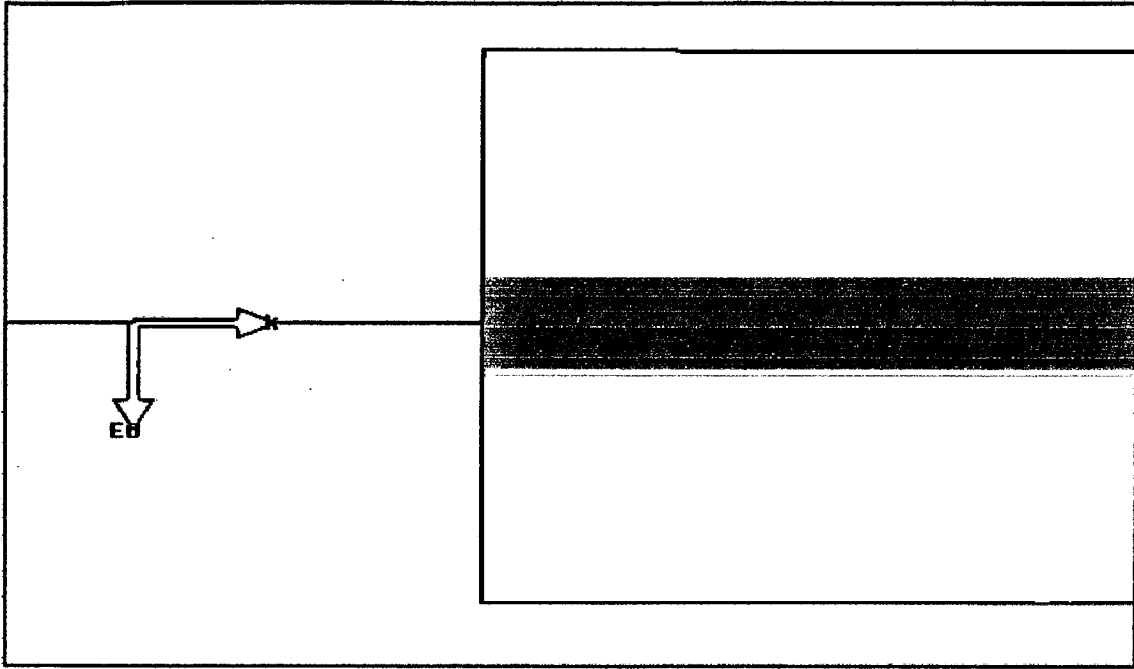


Figure 3.01 (b) Endfire layout

- c) Thin waveguide layout: In this core layer extend far beyond the other 2 layers and irradiated with Gaussian beam as shown, Figure 3.01(c).

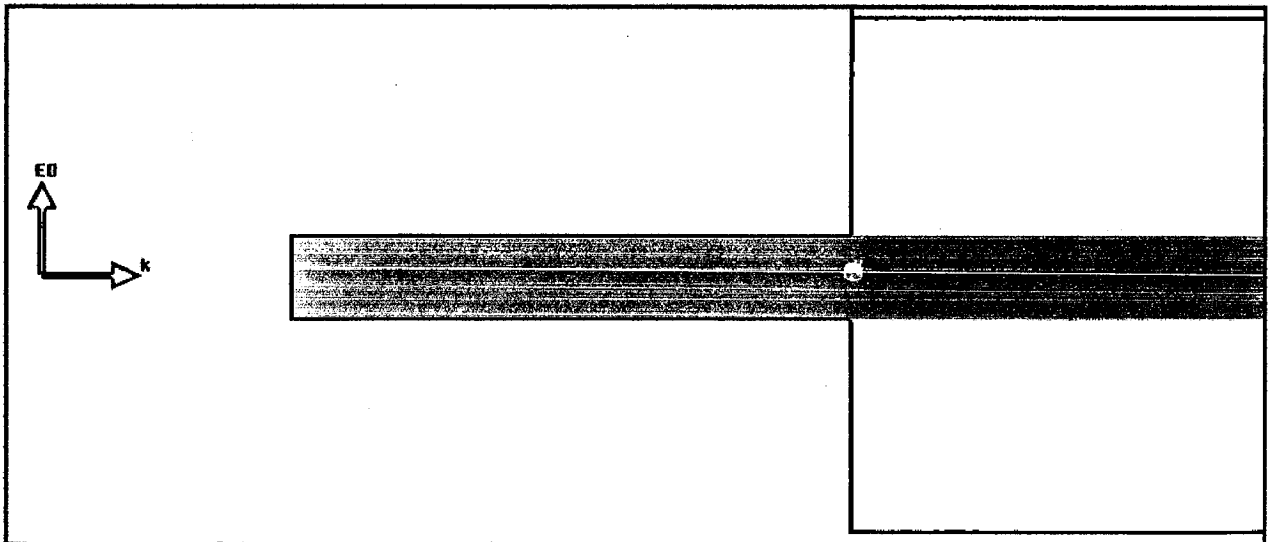
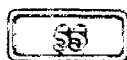


Figure 3.01 (c) Thin waveguide layout

- d) Tapered waveguide layout: In this core layer not only extend far beyond the other 2 layers but also increases exponentially as moves away from reaming layers, which gives it a taper geometry. But the region surrounding the tapered-core layer is air. It is illuminated in the same way as shown in Figure 3.01 (c).



- e) Metal clad tapered coupling: This structure is same as that of tapered waveguide layout, described above, with an exception that the region surrounding the tapered-core layer is only clad layer.
- f) I shaped aperture [64]: In this paper they have drilled a I shaped slot in the launching metallic plane (of certain thickness) and the slot WG structure is excited by the Gaussian beam via I shaped aperture. This structure will be discussed in the next coming sections.
- g) In [65] they use circular and elliptical structures in metallic films or plasmonic lenses, that excite as well as focus the EM energy of SPPs.
- h) In [66], Wen, uses nano-antenna of T shape consisting of narrow slot (which ultimately connected to slot WG) to excite and propagate the SPPs through the slot via nano-antenna. In another paper [67], they have used tapered silicon (Si) layer to excite the slot WG structure. And based on this launching mechanism they have fabricated nano-scale splitter and coupler. Both of these paper have been fabricated and tested.

Having described the launching mechanism of Gaussian beam or plane wave, next section elaborate on the simulated results of the designs reported in the literature. Most of the papers reported in literature uses FDFD or FDTD, which are customized MATLAB [49] code, as they are well suited for material dispersion and arbitrary shaped inclusion. Very few paper uses Ansoft HFSS or CST-MWS or Comsol MP which also an FEM based commercial tool. In the next section we will be discussing or cross verifying the HFSS simulated designs with that reported in literature. For cross verification of the simulated results, we will first understand the geometry and results which is given in the literature, and then the simulated design and results will analyzed. This type of layout will be followed in next section.

3.3 Simulation results of plasmonic SWG (SPWG)

3.3.1 SPP gap WG excited through I shaped aperture [64]

In [64], design in Figure 3.02 (a) is used and various field patterns in top view (Figure 3.02 (b)), side view (Figure 3.02 (c)) and front view(Figure 3.03) is shown. In this design, gap size is $\lambda/6 * \lambda/6$.

Reported Design

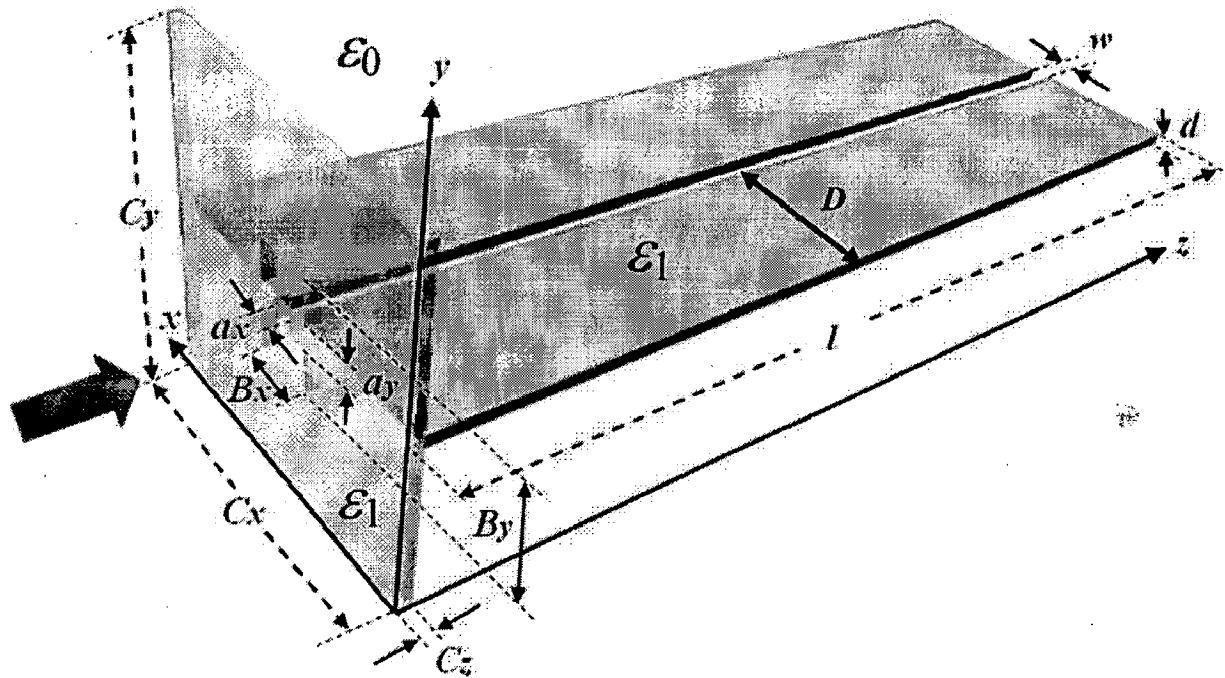


Figure 3.02(a): Geometry of the problem used in the simulation.

Reported Results

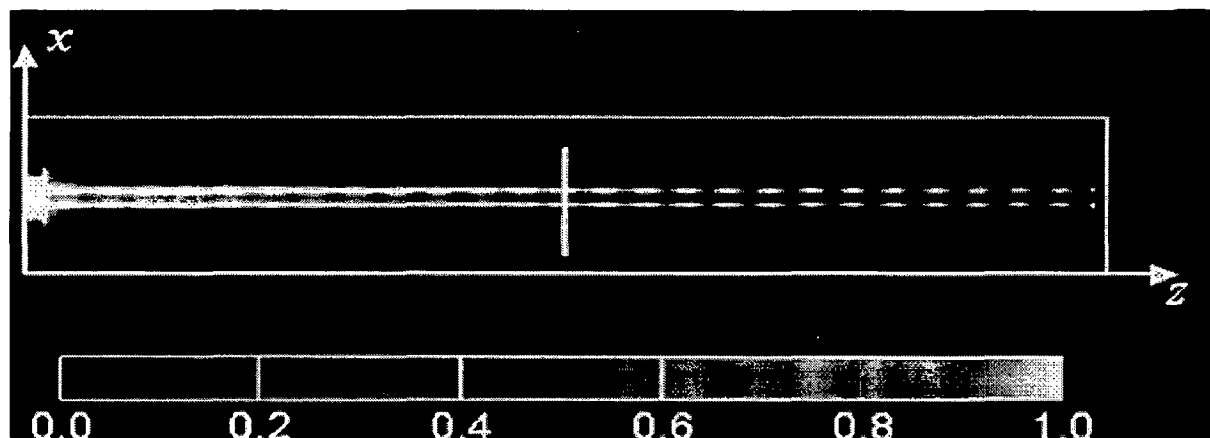


Figure 3.02(b): Optical intensity $|E|^2$ on a plane parallel to the x - z plane

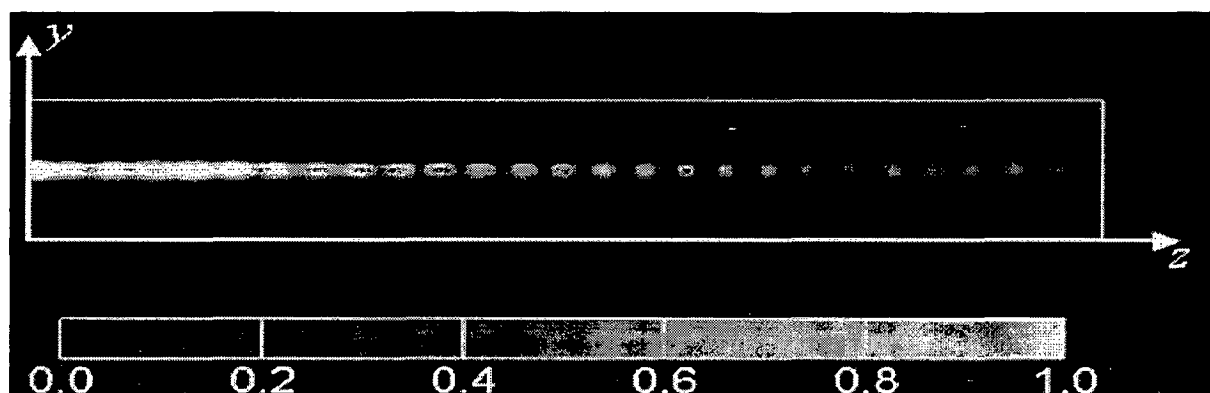


Figure 3.02(c): Optical intensity $|E|^2$ on a plane, which includes center axis of the waveguide and is parallel the y - z plane

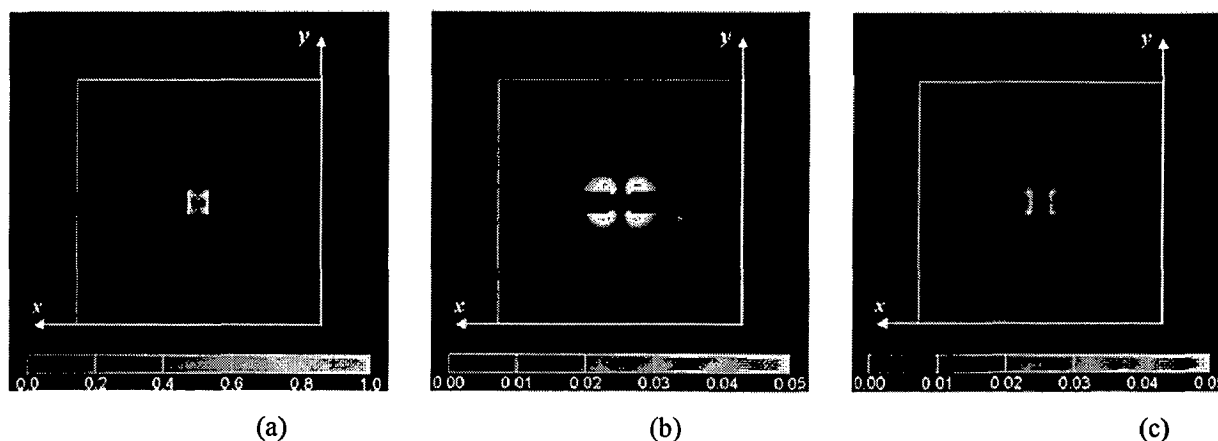


Figure 3.03: Optical intensities of (a) $|E_x|^2$, (b) $|E_y|^2$ and (c) $|E_z|^2$ on a plane parallel to the x - y plane indicated by a white line in Figure 3.02(a). Notice that the normalized intensity scales are (a) 0.0–1.0, (b) 0.0–0.05 and (c) 0.0–0.05.

Simulated Design

Based on the geometry of [64], Figure 3.04 (a) is simulated and perspective (Figure 3.04 (b)) and front view (Figure 3.04 (c)) of the results is shown. In Figure 3.04 (b), based on the E field scale given, the electric field exist up to 1-2 μm or SPP propagation length is 1-2 μm . While in Figure 3.04 (c), we can observe that the field exist outside the gap region too, although the its strength between 0.6-0.9 V/m.

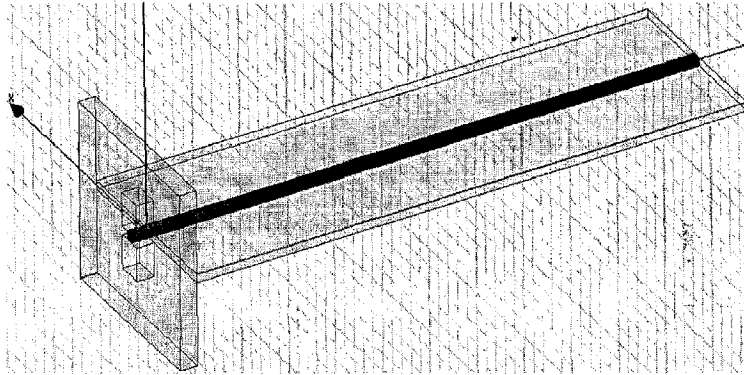


Figure 3.04(a) Reported design [64] is simulated using HFSS.



Simulated Results

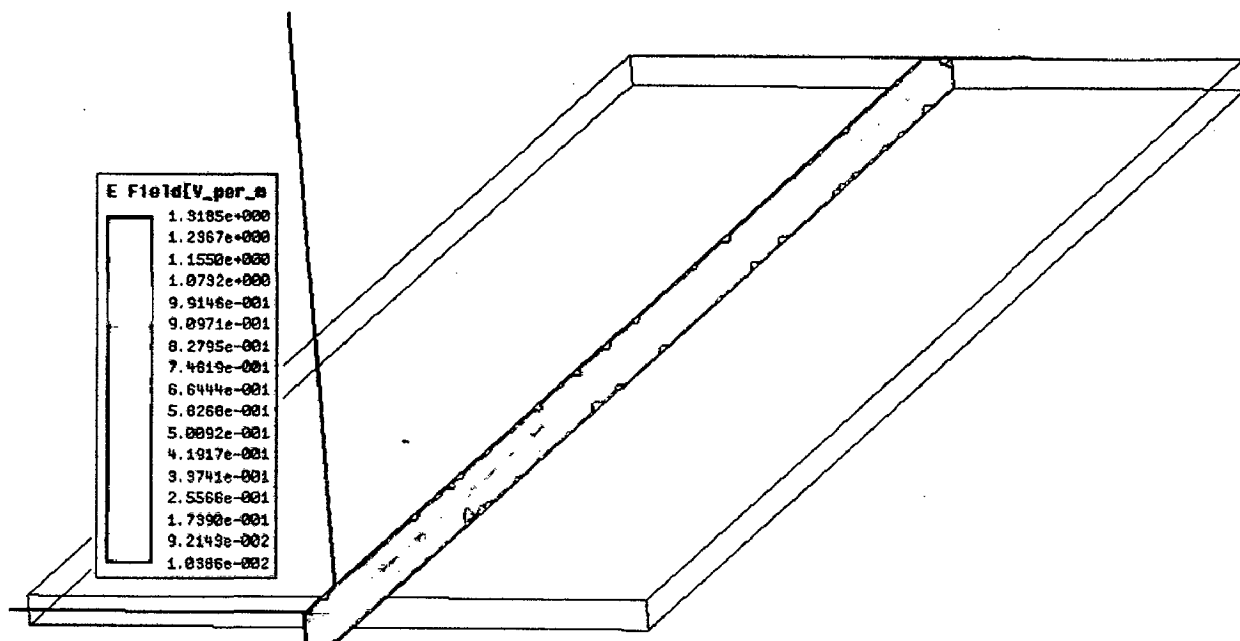


Figure 3.04(b) Perspective view of the design in Figure 3.04 (a)

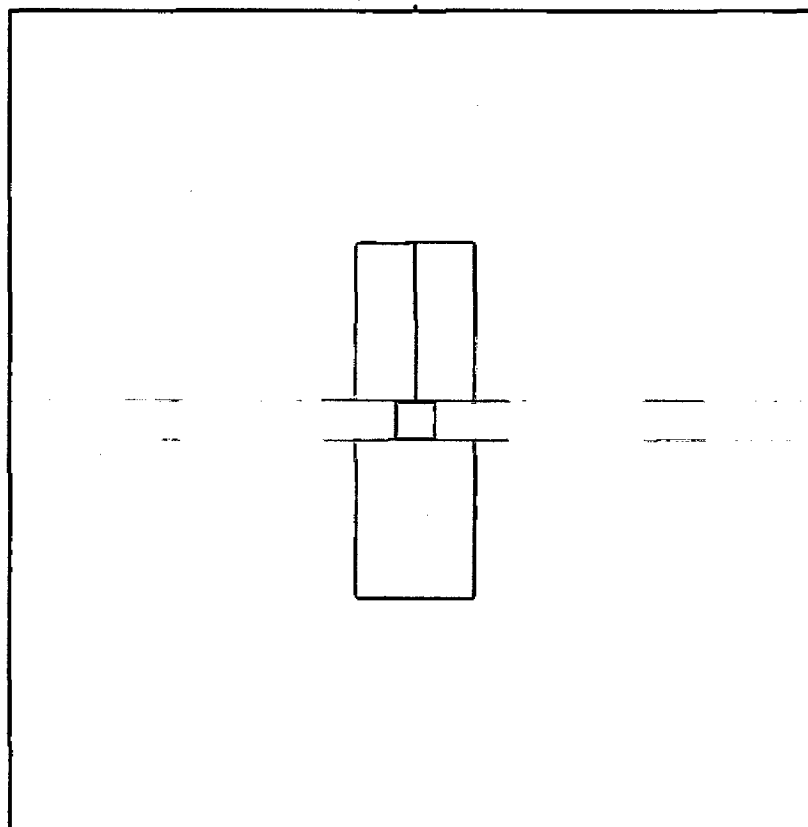


Figure 3.04(c) Front view of the design in Figure 3.04 (a)

3.3.2 SPP gap WG excited using nano-antenna [66]

In [66], design in Figure 3.02 (a) is used and various field patterns in top view (Figure 3.02 (b)), side view (Figure 3.02 (c)) and front view (Figure 3.03) is shown. In this design, gap width is $\lambda/50$ and gap height is $\lambda/10$.

Reported Design and Results

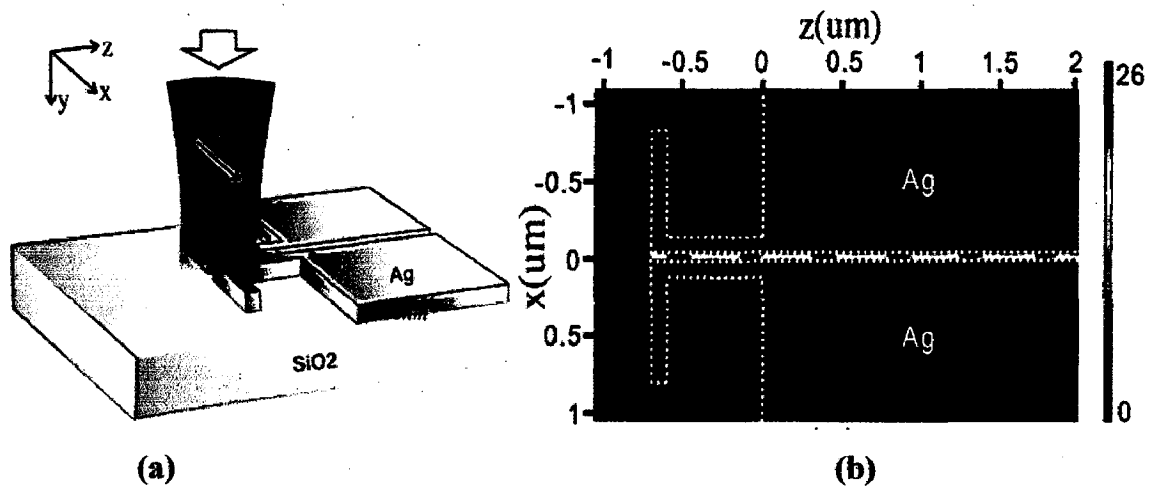


Figure 3.05 (a): The incident beam is focused from air to the center of the antenna, which feeds the GPW (b) The field distributions $|E|$ on the xz plane ($y = 0$)

Simulated Design

Based on the geometry of [66], Figure 3.06 (a) is simulated and top (Figure 3.06 (b)) and perspective view (Figure 3.06 (c)) of the results is shown. In Figure 3.06 (b), based on the E field scale given, the electric field is excited in the slot, from the nano-antenna. While Figure 3.06 (c), exhibit the localization phenomenon of the excited SPPs, in the sense, they decay out exponentially along the slot length.

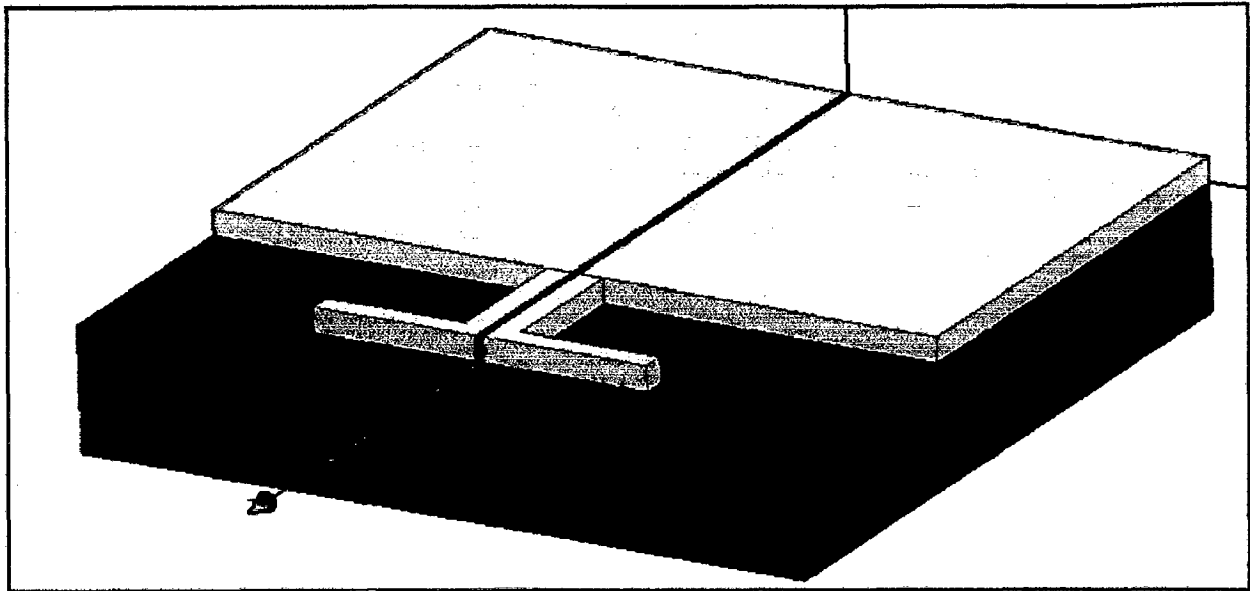


Figure 3.06 (a): Reported design [66] is simulated using HFSS

Simulated Results

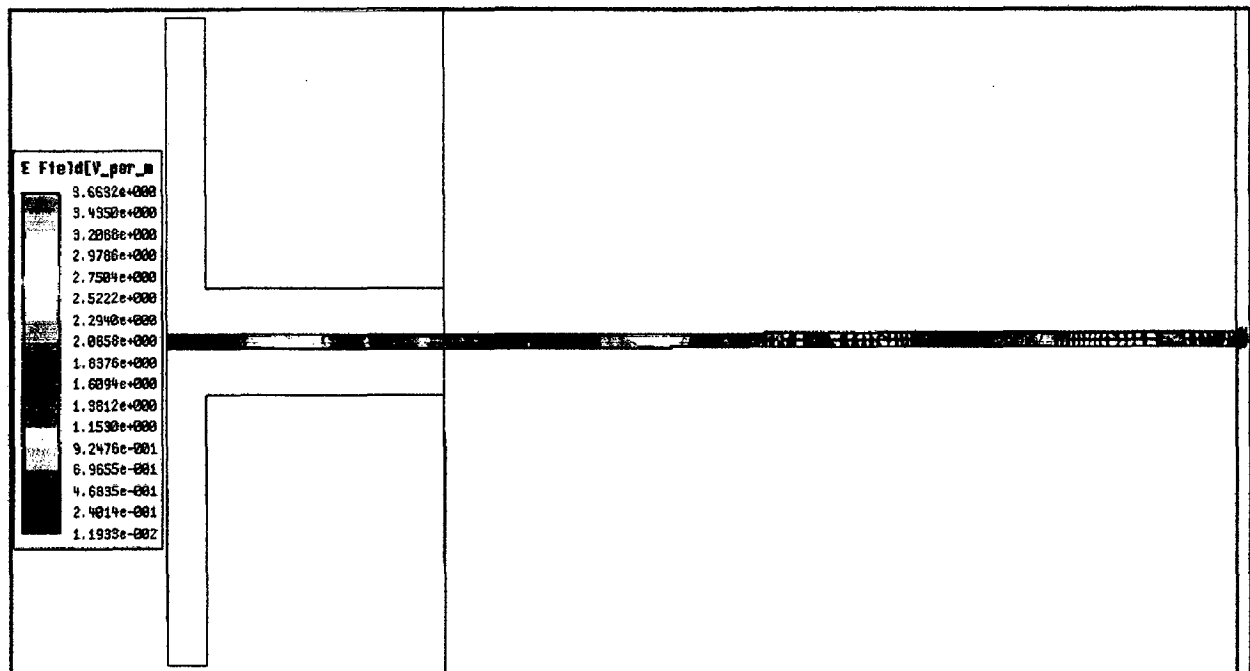


Figure 3.06(b) Top view of the design in Figure 3.06 (a)

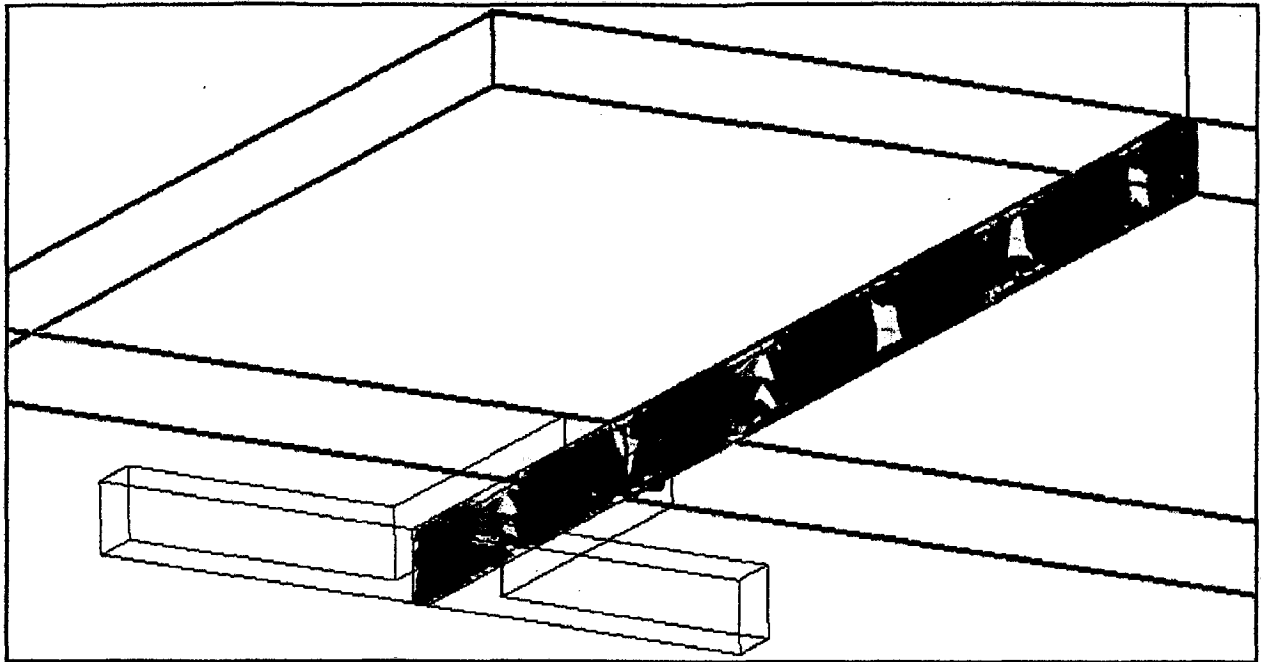


Figure 3.06(c) Perspective view of the design in Figure 3.06 (a)

3.3.3 SPP gap WG excited using broadband pulse[68]

In [68], design in Figure 3.07 (a) is used and field patterns in front view (Figure 3.07 (b)) is shown. In this design, gap width is $\lambda/300$ to $\lambda/50$ and gap height is $\lambda/30$.

Reported Design

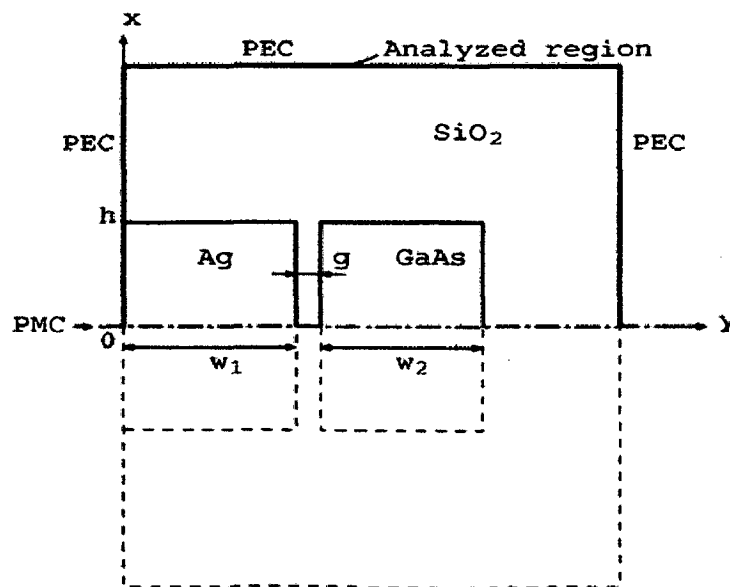


Figure 3.07(a) Calculation configuration/domain using a symmetry boundary condition.

Reported Results

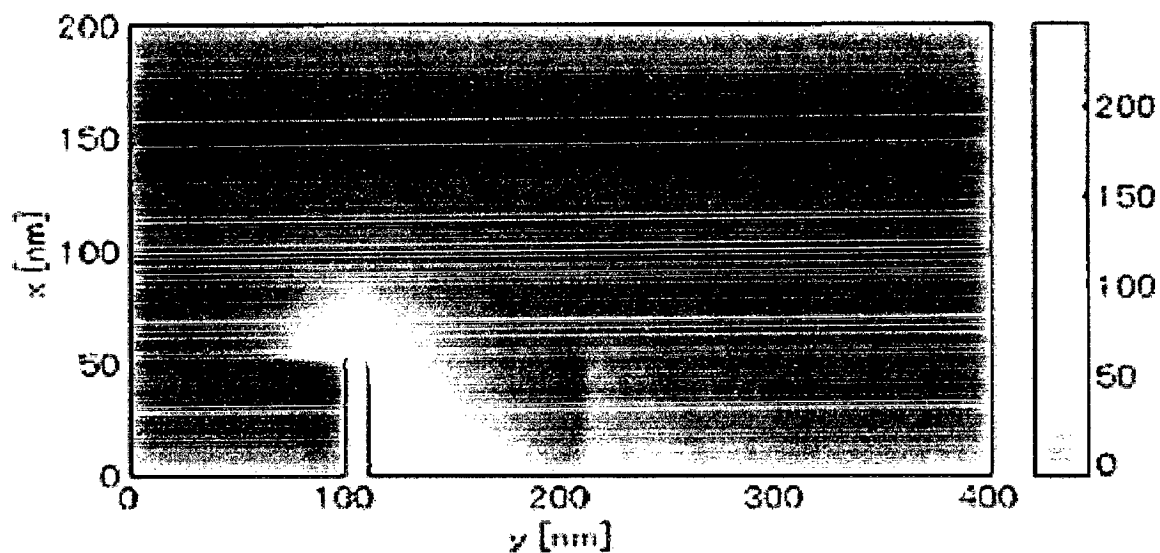


Figure 3.07(b) Distributions of normalized intensity.

Simulated Design

Based on the geometry of [68], Figure 3.08 (a) is simulated and perspective view (Figure 3.06 (b)) of the results is shown. In Figure 3.08 (b), based on the E field scale given, the electric field is excited in the slot. Prominent repetition of electric field can be observed. Excited SPPs exhibit the localization phenomenon.

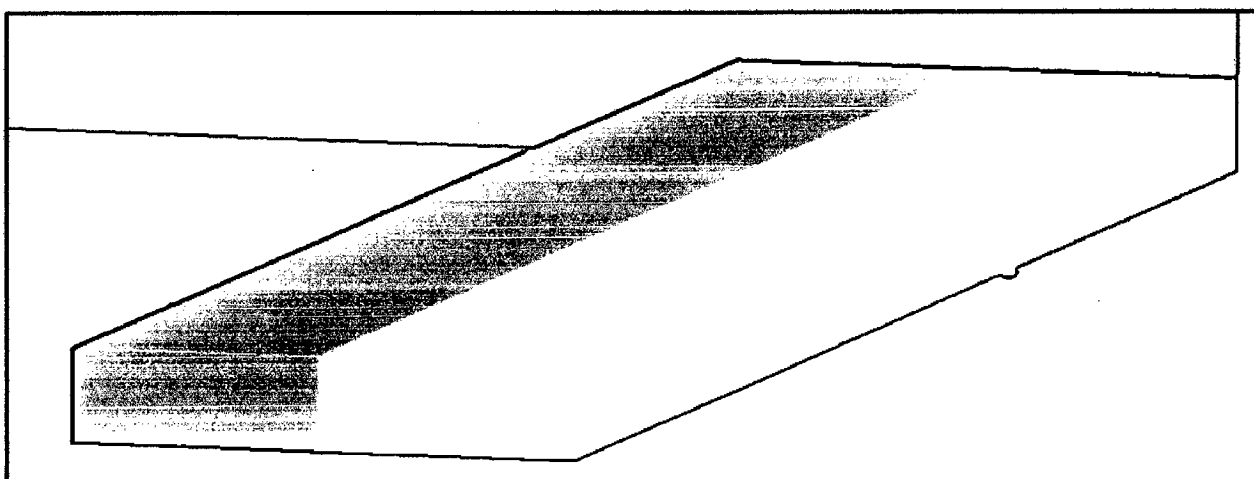


Figure 3.08(a) Reported design [68] is simulated using HFSS, Drude Ag is in dark blue color and Lossless dielectric is in dark purple color separated by thin clad layer.

Simulated Results

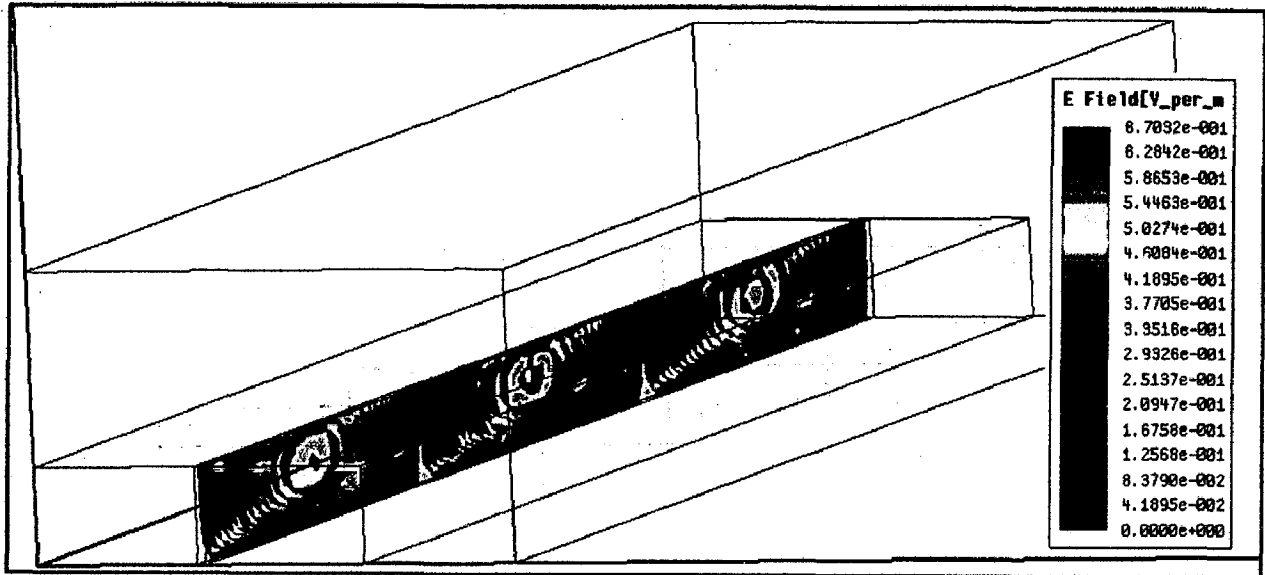


Figure 3.08(b) Perspective view of the design in Figure 3.08 (a)

3.4 Conclusion

In this chapter various plasmonics simulation, pertaining to MIM geometry, is reproduced and respective field configuration is cross verified with that given in the literature. In the next chapter, we discuss a novel configuration of MIM geometry, where there is only one 'drude modeled' metal layer, followed by air gap/slot, further followed by high dielectric index material. Such geometry is termed as metal/dielectric1/dielectric2 (M/D1/D2) or hybrid plasmonics structure.

Chapter 4

Slot Plasmonic hybrid Waveguide Structures (M/D1/D2)

4.1 Introduction

The different arrangements proposed in this chapter for hybrid metallo-dielectric waveguides [69] are depicted in Figure 4.01. Figure 4.01(a) depicts hybrid slot waveguide and Fig. 4.01(b) depicts an hybrid waveguide. The void slot arranged in the former waveguide will give rise to a subwavelength mode confinement due to a combination of plasmon and high-index contrast effects. Owing to the plasmon coupling effect, the modal field diameter is reduced by half in relation with the dielectric slot waveguide counterpart. In addition, due to the presence of the dielectric, the E-field is spread over the low loss dielectric, reducing the amount of E-field in contact with the high-loss metal surface, and therefore, the losses are reduced with respect to the plasmonic MIM counterpart. On the other hand, the hybrid waveguide can be studied as a conventional surface plasmon polariton (SPP) waveguide with a high index cladding. It has been observed that the high-index cladding provides the SPP waveguide with an additional confinement, so that the lateral field extension is diminished significantly.

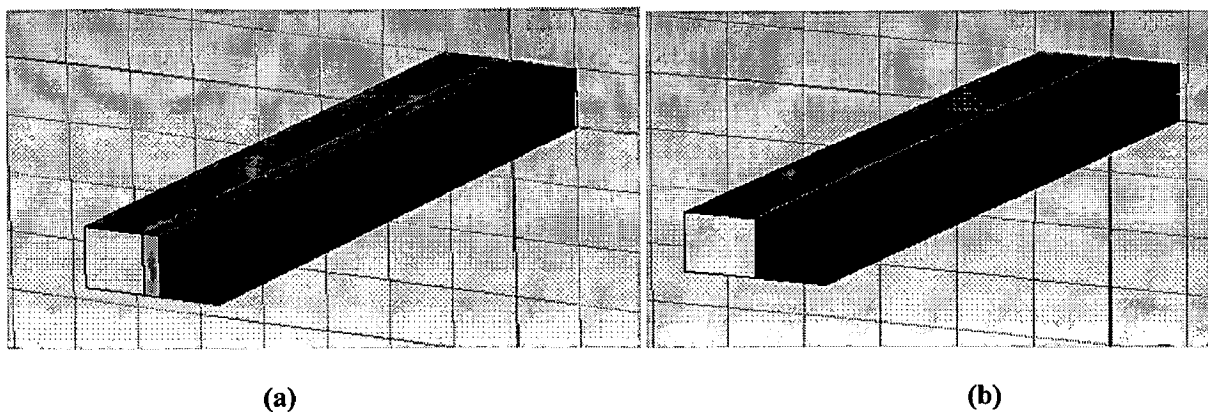


Figure 4.01 Hybrid plasmonic WG (a) Hybrid slot waveguide. (b) Hybrid waveguide

In this chapter too, for cross verification of the simulated results, we will first understand the geometry and results which is given in the literature, and then the simulated design and results will analyzed.

4.2 Simulation results of hybrid Slot WG [69]

In [69], design in Figure 4.02 (a) is used and various field patterns (Figure 4.03 (a) and (b)) and dispersion diagram (Figure 4.03(c)) is shown. In this design, gap width is $\lambda/30$ and gap height is $\lambda/8$.

Reported Design

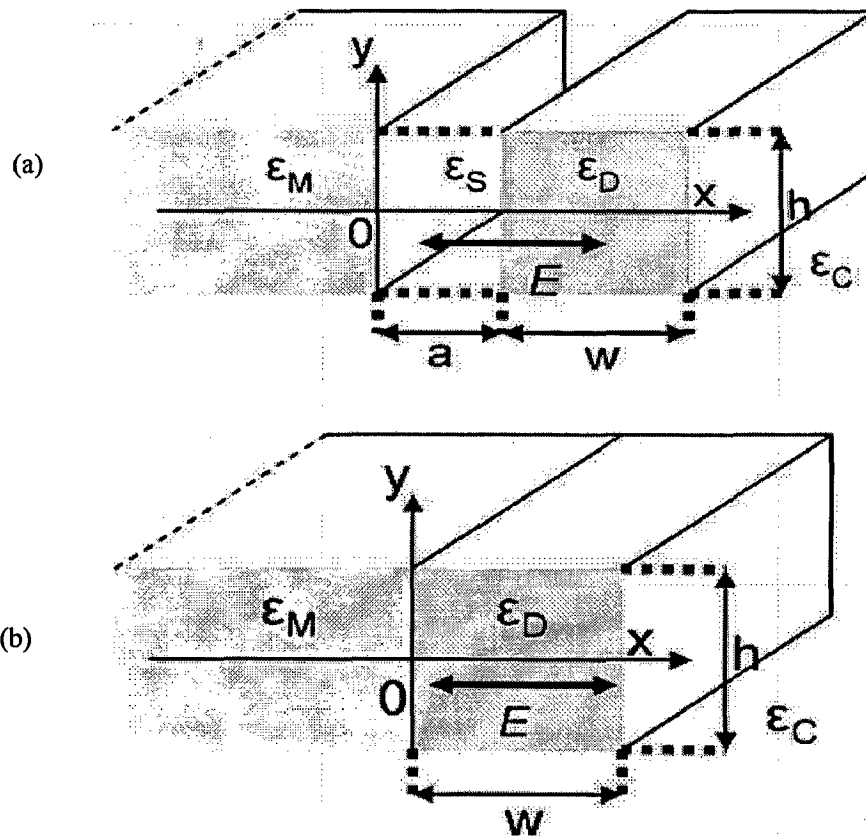


Figure 4.02: Layout of the waveguides proposed [69]. (a) Hybrid slot waveguide. (b) Hybrid waveguide.

Reported Results for Hybrid Slot Waveguide.

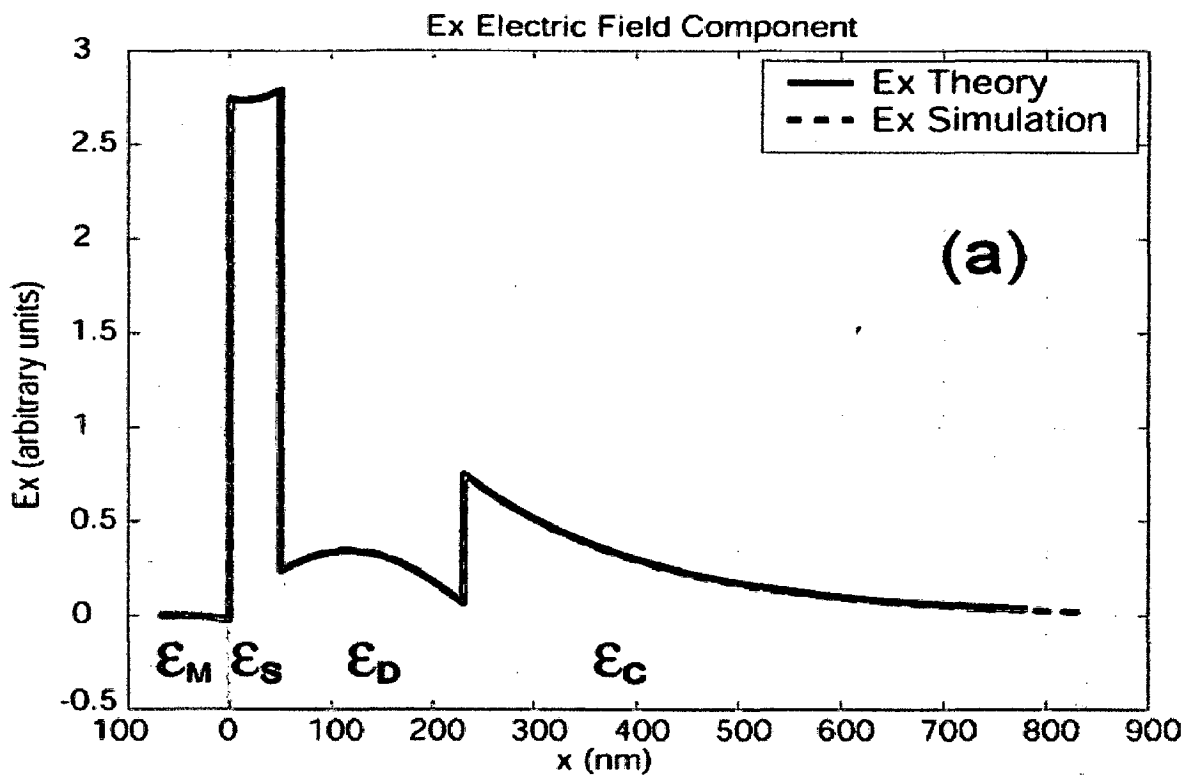


Figure 4.03 (a): These figures represent the E-field distribution with $w = 180$ nm, $a = 50$ nm, $\epsilon_S = \epsilon_C = 1$, $\epsilon_D = 11.9$, $\epsilon_M = -115.8 + j10.33$. (a) Hybrid slot waveguide.

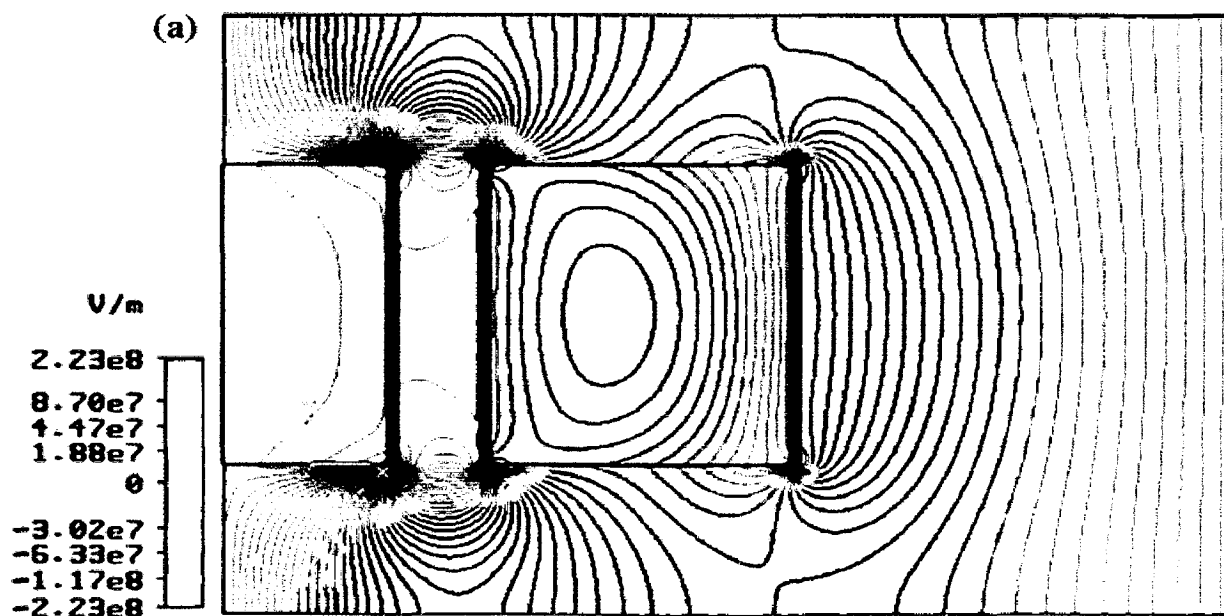
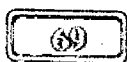


Figure 4.03 (b): Electric field pattern computed for $h = 200$ nm, $a = 50$ nm, $w = 180$ nm at 1550 nm. (a) Hybrid slot waveguide.



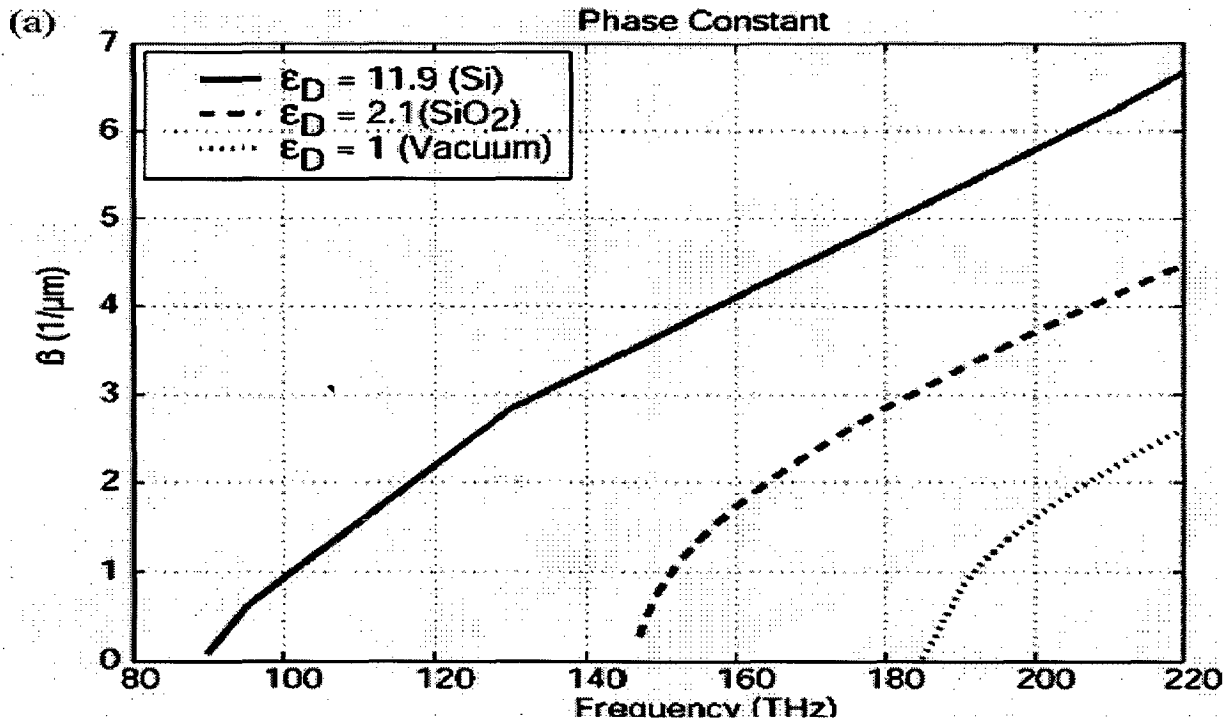


Figure 4.03 (c): Dispersion curves. (a) Hybrid slot waveguide.

Simulated Results for Hybrid slot waveguide

Based on the geometry of [69], design in Figure 4.01(a) is simulated and top and front view (Figure 4.04 (a) and (b)) of the field variation is shown. In Figure 4.04 (a), electric field variation along x axis is drawn where as Figure 4.04 (b) shows the vertical confinement effect on electric field in the slot. Figure 4.04 (c) shows the dispersion curve of the hybrid slot geometry and it matches with that reported in [69] up to certain range.

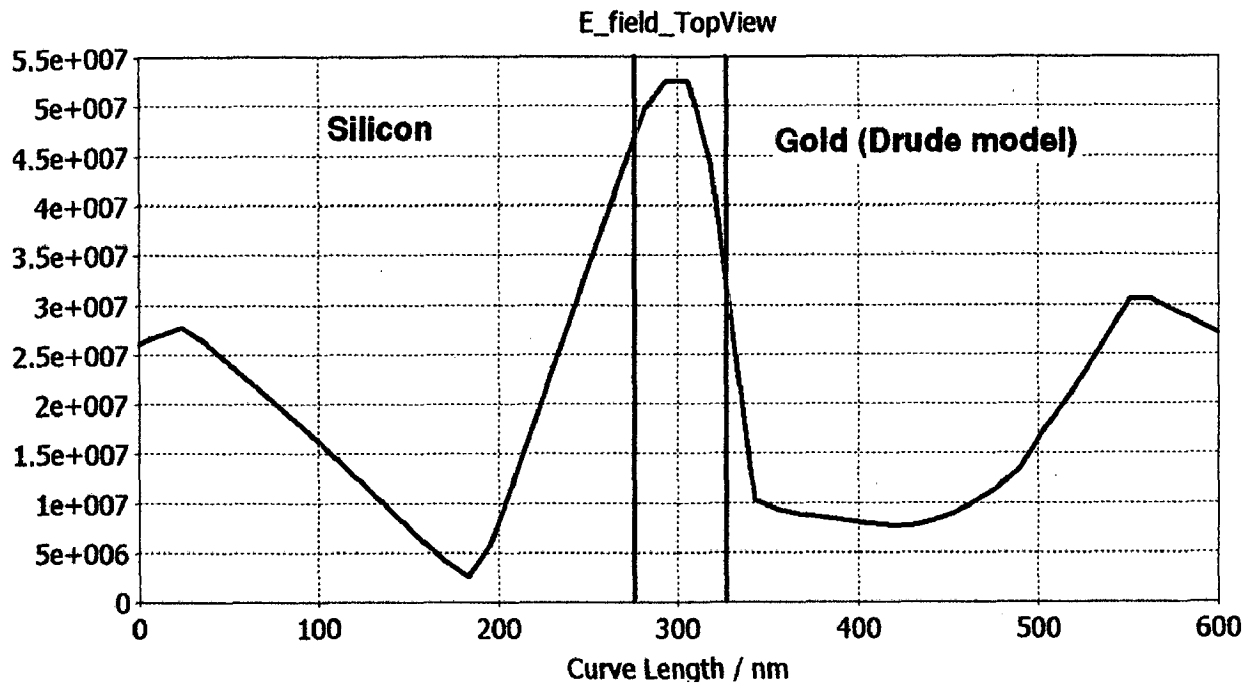


Figure 4.04 (a): Simulated E filed variation along x axis in the hybrid slot structure, Top view of Figure 4.01 (a)

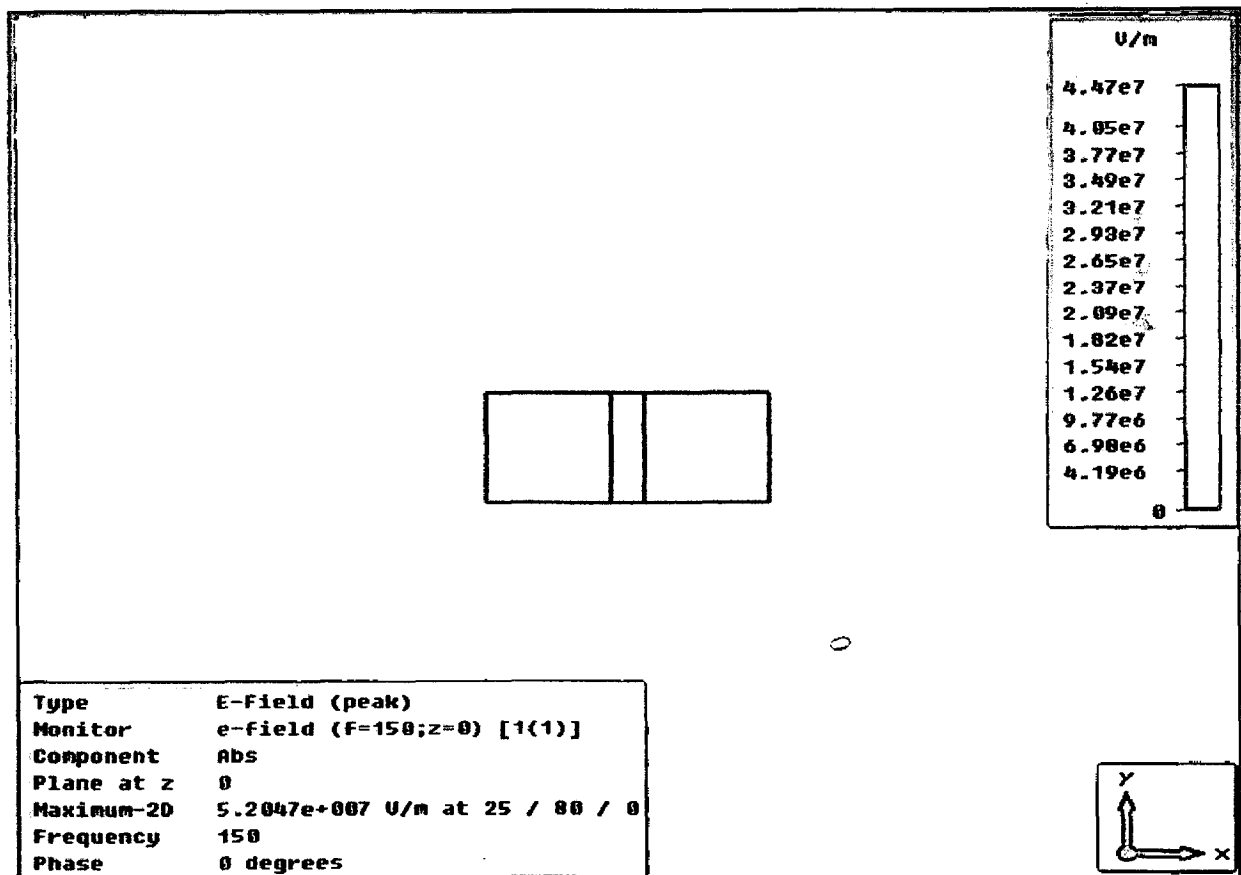


Figure 4.04 (b): Simulated E filed variation in the slot, Front view of Figure 4.01 (a) , (D1/D2/M).

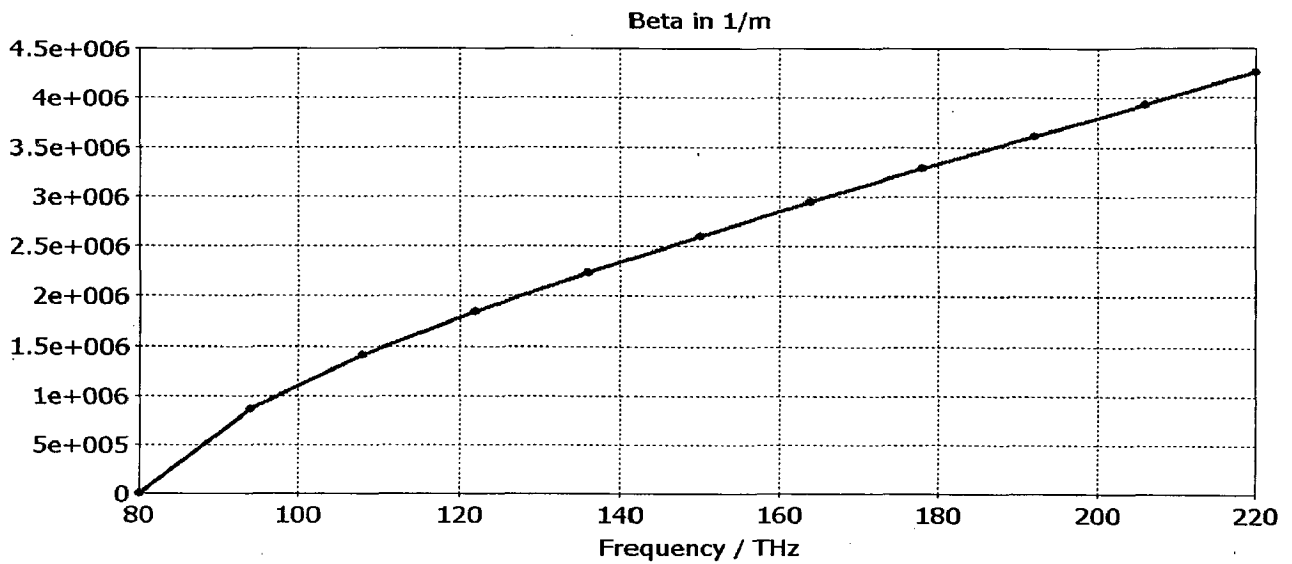


Figure 4.04 (c): Simulated dispersion diagram for hybrid slot WG.

4.3 Simulation results of hybrid WG [69]

In [69], design in Figure 4.02 (b) is used and various field patterns (Figure 4.05 (a) and (b)) and dispersion diagram (Figure 4.05(c)) is shown. In this design gap height is $\lambda/8$.

Reported Results for Hybrid Waveguide.

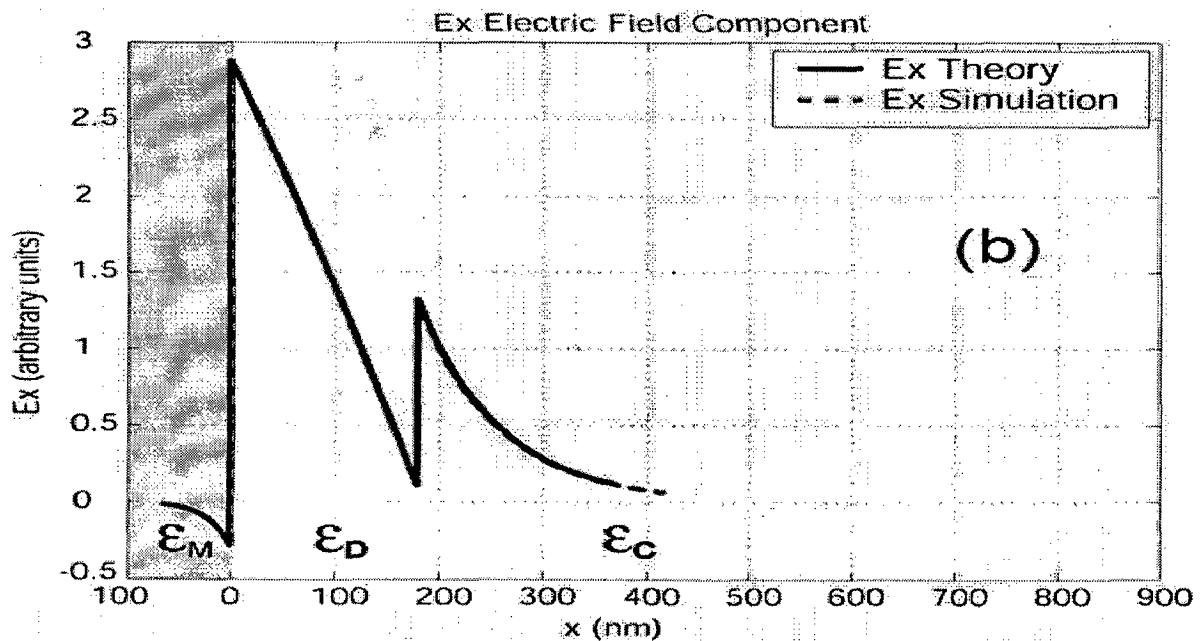


Figure 4.05 (a): These figures represent the E-field distribution with $w = 180$ nm, $a = 50$ nm, $\epsilon_S = \epsilon_C = 1, \epsilon_D = 11.9, \epsilon_M = -115.8 + j10.33$. (a) Hybrid waveguide.

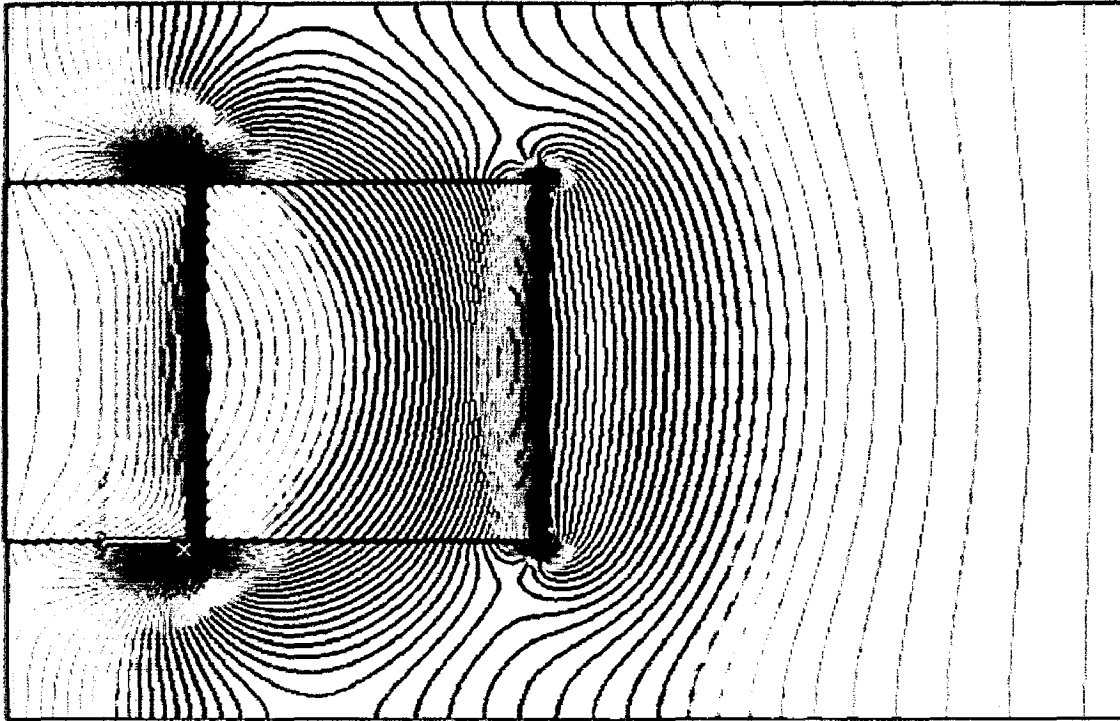


Figure 4.05 (b): Electric field pattern computed for $h = 200$ nm, $a = 50$ nm, $w = 180$ nm at 1550 nm. (a) Hybrid slot waveguide.

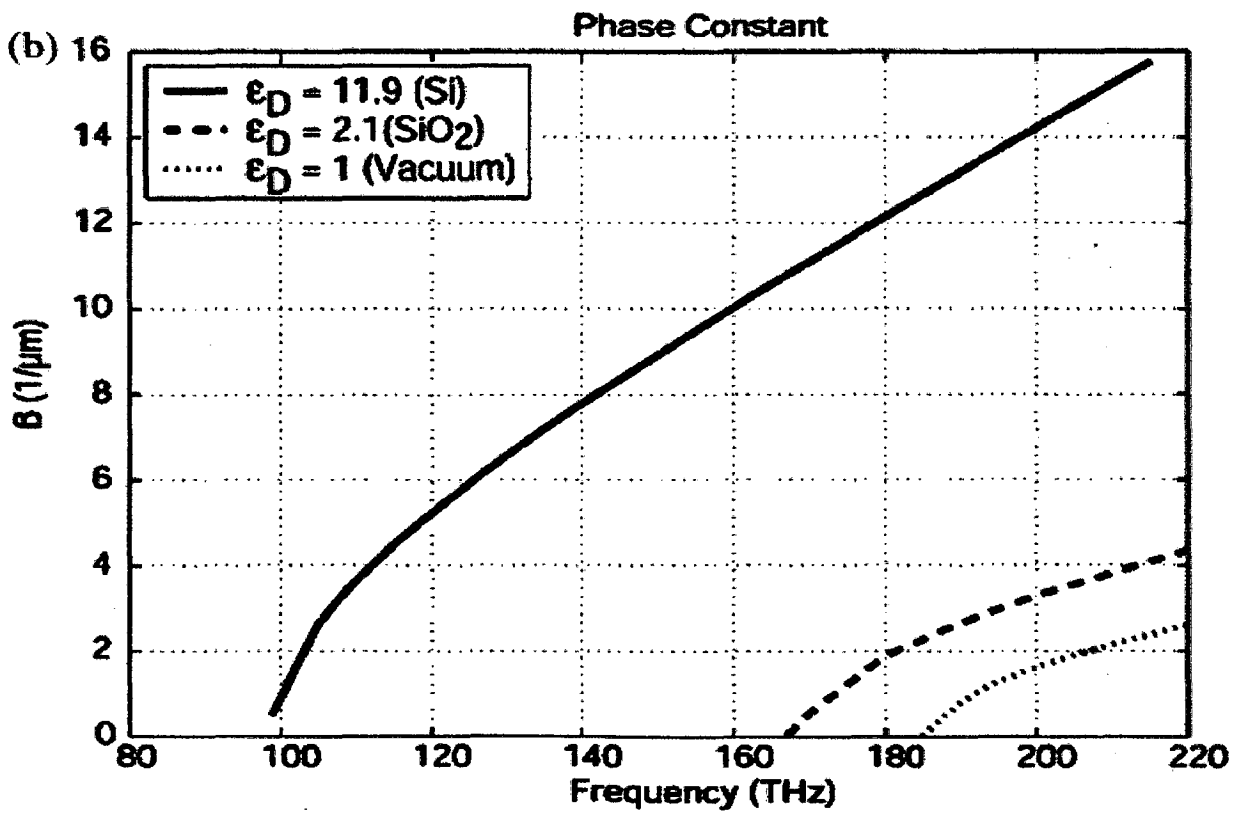


Figure 4.05 (c): Dispersion curves. (a) Hybrid waveguide.

Simulated Results for Hybrid waveguide

Based on the geometry of [69], design in Figure 4.01(b) is simulated and top and front view (Figure 4.06 (a) and (b)) of the field variation is shown. Figure 4.06 (a), traces the electric field variation along x axis where as Figure 4.06 (b) shows the field confinement in dielectric. Figure 4.06 (c) shows the dispersion curve of the hybrid geometry and it matches with that reported in [69] up to certain range.

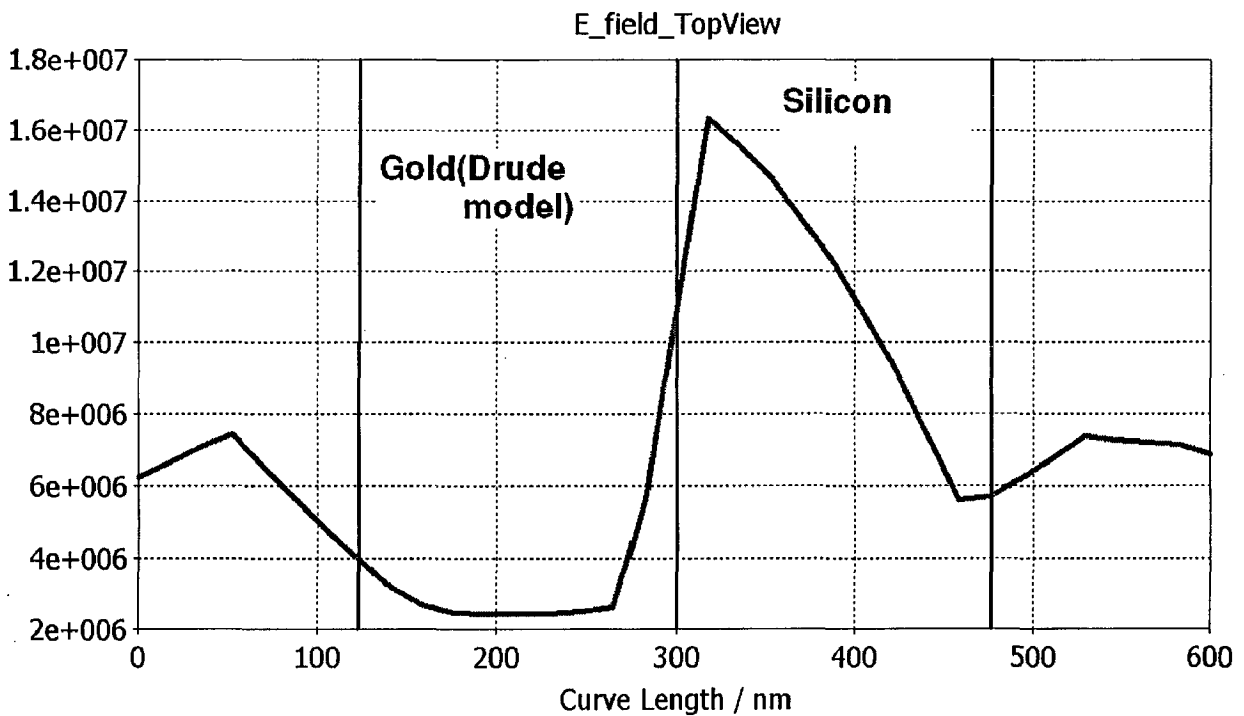


Figure 4.06 (a): Simulated E field variation along x axis in hybrid WG structure, Top view of Figure 4.01 (a)

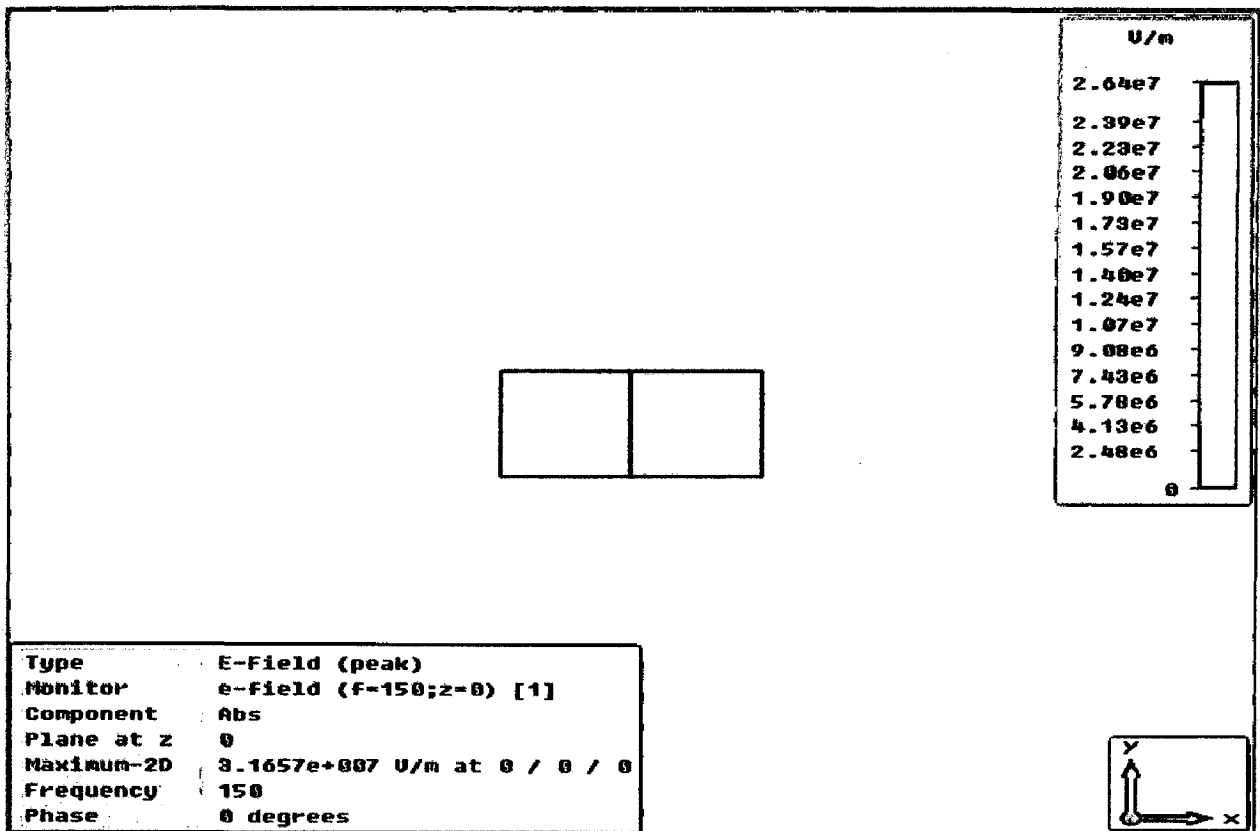


Figure 4.06 (b): Simulated E field variation in the slot, Front view of Figure 4.01 (a), (M/D).

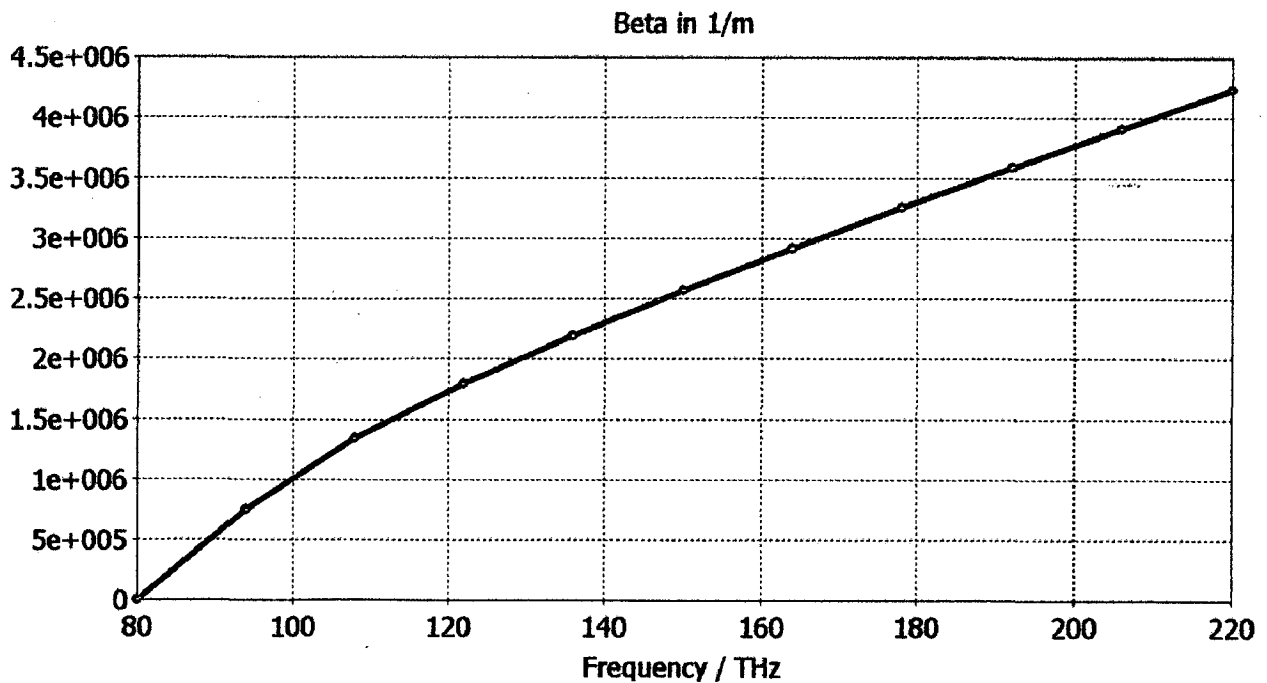


Figure 4.06 (c): Simulated dispersion diagram for hybrid slot WG.

4.4 Conclusion

In this chapter two hybrid plasmonic structures are studied which are reported in [69], namely M/D1/D2 geometry and M/D geometry. Various field configuration and dispersion relation is cross verified with that given in the literature. The simulated results are almost resembling to that reported. Slight variation in the field confinement and dispersion curves is observed, which can be attributed to simulation setting or the modeling of metal at high frequency.

Chapter 6

Conclusions and Future Scope

6.1 Summary and Conclusion of the Work Done

We have seen the thorough design procedure for NRD guide to WR transition. We have developed two transitions, one using H plane WR transition and other using horn antenna. In the H plane transition, position of the WR's determine the power transfer. And in the horn antenna transition, length and width of the flare section along with taper plane and size controls the power coupling between WR and NRD guide. After this, design of SIR based BPF and BSF is studied. SIR gives the flexibility that the spurious response can be placed sufficiently far apart from the fundamental response.

Next we have explored the colorful branch of plasmonics. Plasmonics effect becomes prominent whenever the operating frequency reaches the plasma frequency of the metal. This coincidence result in generation of small length and highly concentrated, waves called surface plasmons. Numerous geometries relating to the plasmonics WG is studied which covers metal dielectric (M/D), metal dielectric metal (M/D/M), different dielectric layers (D1/D2/D3) and hybrid plasmonics WGs. Their respective field patterns and dispersion curves are plotted and cross verified with the existing literature.

6.2 Scope for Further Work

1. The NRD guide to WR H plane transition can be further explored by modeling it with the methods available in existing literature like magnetic dipole moment method, so that the position of WR's can be analytically calculated.
2. In plasmonic slot WG geometries, launching the beams which can excite the SPP's need be studied. In most of the cases, laser beam is used to excite the SPP's but the achieved propagation length is very small. Efficient plasmon launcher need to be investigated.
3. In SPP supporting WG, there exist a tradeoff between propagation length and losses. We need to find an alternative to overcome this tradeoff, such that low loss can be achieved for larger propagation length.

References

- [1] H. H. Meinel, "Millimeter-Wave Technology Advances Since 1985 and Future Trends", IEEE Trans. Microwave Theory Tech., Vol. 39, No. 5, pp. 759-767, May 1991.
- [2] T. Yoneyama and S. Nishida, "Non-Radiative Dielectric Wave-guide for Millimeter Wave Integrated Circuits", IEEE Trans. Microwave Theory Tech., Vol. MTT-29, No. 11, pp. 1188-1192, November 1981.
- [3] S. A. Maier, "Plasmonics - Towards Subwavelength Optical Devices", Current Nanoscience, Vol. 1, No. 1, pp. 17-22, January 2005.
- [4] M. L. Brongersma, "Recent Progress in Plasmonics", OSA / CLEO/QELS, 2008.
- [5] T. Yoneyama and S. Nishida, "Non-Radiative Dielectric Waveguide Circuit Components", International Journal of Infrared and Millimeter Waves, Vol. 4, No. 3, pp. 439-449, 1983.
- [6] D. M. Pozar, "Microwave engineering," New York: John Wiley & Sons, 3rd edition, 2004.
- [7] T. Yoneyama, "Millimeter-wave integrated circuits using non-radiative dielectric waveguide", Electronics and Communications in Japan, Part 2, Vol. 74, No. 2, pp.20-28, 1991.
- [8] S. K. Koul, "Millimeter Wave and Optical Dielectric Integrated Guides and Circuits", John Wiley & Sons, Chapter 6, 1997.
- [9] www.ansoft.com (including antenna kit)
- [10] K. Wu, and L. Han, "Hybrid Integration Technology of Planar Circuits and NRD-Guide for Cost-Effective Microwave and Millimeter-Wave Applications," IEEE Transactions On Microwave Theory And Techniques, Vol. 45, No. 6, pp. 946-954, June 1997.
- [11] C. A. Balanis, "Advanced Engineering Electromagnetics," Wiley, 3rd Edition.
- [12] J.Tang, D. Deslandes and K. Wu, "Spurious Mode Suppressing Technique For Performance Enhancement Of Hybrid Planar/Nrd-Guide Circuits" , IEEE, Microwave Conference(Asia Pacific), pp. 140 – 143, Dec. 2000.
- [13] J. Tang and K. Wu, "Co-Layered Integration and Interconnect of Planar Circuits and Non-Radiative Dielectric Waveguides", IEEE Trans. Microwave Theory Tech., Vol. 48, No. 4, pp. 519-524, Apr. 2000.
- [14] R. E. Collin, "Field Theory of Guide Waves", New York: McGraw-Hill, Chapter 11, pp. 470-473, 1960.
- [15] D. Dawn and M. Sachidanand, "Analysis and Design of stripline to NRD guide transition", Proc. 3rd Microwave Conference(Asia Pacific), Tokyo, pp. 15-18, 1990.
- [16] N. P. Pathak, S. K. Koul, and A. Basu, "A Transition for Hybrid Integration of Suspended Stripline and Non-Radiative Dielectric Guide," Microwave and Optical Technology Letters, Vol. 43, No. 1, pp. 79-82, Oct. 2004.



- [17] N. P. Pathak, "Integration of NRD Guide and Slot Line for Millimeter Wave Indoor Wireless Applications," in Proceeding of WFMN07, Chemnitz, Germany, pp.124-126, 2007.
- [18] T. Shimizu and T. Yoneyama, "NRD-guide and waveguide H-plane transition and its application for lens antenna feeding structure," IEICE Trans. Electron. (Japanese Edition), vol.J89-C, no.5, pp.312-320, May 2006.
- [19] T. Yoneyama, S. Fujita and S. Nishida, "Insulated Nonradiative Dielectric Waveguide for Millimeter-Wave Integrated Circuits", IEEE Transactions on Microwave Theory and Techniques, Vol. MTT-31, No. 12, pp.1002-8, Dec. 1983.
- [20] Y. Cassivi and K. Wu, "Substrate integrated circuits concept applied to the nonradiative dielectric guide", IEE Proceedings- Microwaves, Antennas and Propagation, Vol. 152, No. 6, pp. 424-433, Dec. 2005.
- [21] T. N. Trinh, J.A.G. Malherbe and R. Mittra, "A Metal-To-Dielectric Waveguide Transition With Application To Millimeter-Wave Integrated Circuits", IEEE MTT-S International Microwave symposium Digest, pp. 205-207, May 1980.
- [22] J. A. G. Malherbe, J. H. Cloete and L E. Losch, "A Transition from Rectangular to Nonradiating Dielectric Waveguide", IEEE, IEEE Transactions On Microwave Theory And Techniques, Vol. MTT-33, No. 6, pp. 539-543, June 1985.
- [23] T. Yoneyama and S. Nishida, "Nonradiative Dielectric Waveguide Circuit Components", International Journal of Infrared and Millimeter Waves, Vol. 4, No. 3, pp. 439-449, 1983.
- [24] R. Zia, M. D. Selker, P. B. Catrysse, and M. L. Brongersma, "Geometries and materials for subwavelength surface plasmon modes", Journal of the Optical Society of America A , Vol. 21 Issue 12,, pp. 2442-2446, 2004.
- [25] S. A. Maier, " Plasmonics: The Promise of Highly Integrated Optical Devices", IEEE Journal of Selected Topics in Quantum Electronics, Vol. 12, Issue 6, pp. 1671 – 1677, Nov.-dec. 2006.
- [26] S. A. Maier, " Plasmonics fundamentals and applications", Springer (New York), 2007.
- [27] L. Sweatlock, "Plasmonics: Numerical methods and device applications", Ph.D. dissertation, California Institute of Technology, 2008.
- [28] J. H. Gui, L. Chae, S. J. Kim, and M. Lee, "Surface Plasmon Absorption Characteristics And Nonlinear Optical Properties Of Silver/Copper Codoped Silica Thin Films", Vol.8, Issue 8, pp. 1149-1156, Dec.1997.
- [29] A.D. Rakic, A. B. Djuricic, J. M. Elazar, and M. L. Majewski, "Optical properties of metallic films for vertical-cavity optoelectronic devices", Applied Optics, Vol. 37, Issue 22, pp. 5271-5283, 1998.
- [30] P. B. Johnson and R. W. Christy , " Optical Constants of the Noble Metals", Phys. Rev. B, Vol. 6, Issue 12, pp. 4370-4379, 1972.

- [31] H. J. Hagemann, W. Gudat, and C. Kunz, "Optical constants from the far infrared to the x-ray region: Mg, Al, Cu, Ag, Au, Bi, C, and Al₂O₃," *Journal of the Optical Society of America* Vol. 65, pp. 742, 1975.
- [32] J. Clark, "The Behavior of Metals at Optical Frequencies", Nov. 2004.
- [33] T. Nikolajsen, K. Leosson, I. Salakhutdinov, and S. Bozhevolnyi, "Polymer-based surface-plasmon-polariton stripe waveguides at telecommunication wavelengths," *Appl. Phys. Lett.*, Vol. 82, pp. 668-670, 2003.
- [34] J. Takahara, Y. Suguru, T. Hiroaki, A. Morimoto, and T. Kobayashi, "Guiding of a one-dimensional optical beam with nanometer diameter," *Opt. Lett.*, Vol. 22, pp. 475-477, 1997.
- [35] M. Hochberg, T. B. Jones, C Walker, A. Scherer, "Integrated plasmon and dielectric waveguides", *Optics Express*, Vol. 12, Issue 22, pp. 5481-5486, 2004.
- [36] Degiron and D. R. Smith, "Numerical simulations of long range plasmons", *Opt. Express.*, Vol. 14, issue 4, pp. 1611-25, 2006.
- [37] J. Wen, S. Romanov, and U. Peschel, "Excitation of gap plasmonic waveguides by nano antennas", *OSA / CLEO/QELS 2010*.
- [38] Z. Han, A.Y. Elezzabi and V. Van, "Experimental realization of sub-wavelength plasmonic slot waveguides and couplers on Silicon-on-Insulator", *OSA / CLEO/QELS 2010*.
- [39] P. Berini, "Plasmon-polariton waves guided by thin lossy metal films of finite width: bound modes of symmetric structures," *Phys. Rev. B*, Vol. 61, pp. 10484–10503, 2000.
- [40] N. N. Feng, M. L. Brongersma, and L. D. Negro, "Metal–Dielectric Slot-Waveguide Structures for the Propagation of Surface Plasmon Polaritons at 1.55 μm " ,*IEEE, Journal of quantum electronics*, vol. 43, no. 6, pp.479-485, June 2007.
- [41] G. Veronis and S. Fan, "Modes of Subwavelength Plasmonic Slot Waveguides, Modes of Subwavelength Plasmonic Slot Waveguides", *IEEE Journal of Lightwave Technology*, Vol. 25, No. 9, pp. 2511-2521, Sept 2007.
- [42] E. Berglind, L. Thylen, L. Liu, "Plasmonic/metallic passive waveguides and waveguide components for photonic dense integrated circuits: a feasibility study based on microwave engineering", *IET Optoelectronics*, Vol. 4, Issue. 1, pp. 1–16, 2010.
- [43] S. E. Kocabas, G. Veronis, D. A. B. Miller and S. Fan, "Transmission Line and Equivalent Circuit Models for Plasmonic Waveguide Components", *IEEE, Journal of selected topics in quantum electronics*, Vol. 14, No. 6, pp. 1462-1472, Nov/Dec 2008.
- [44] D. S. L. Gagnon, S. E. Kocabas and D. A. B. Miller, "Characteristic Impedance Model for Plasmonic Metal Slot Waveguides", *IEEE, Journal of selected topics in quantum electronics*, Vol. 14, No. 6, pp. 1473-1478, Nov/Dec 2008.

- [45] H. Sun, A. Chen and L. R. Dalton, "Enhanced Evanescent Confinement in Multiple-Slot Waveguides and Its Application in Biochemical Sensing", IEEE, Photonics Journal, Vol. 1, no. 1, pp. 48-57, June 2009.
- [46] F. Kuroki, H. Ohta, T. Yoneyama, "Transmission characteristics of NRD guide as a transmission medium in THz frequency band", IEEE, Infrared and Millimeter Waves Conference on Terahertz Electronics, vol. 2, pp.331 - 332, Sept. 2005.
- [47] www.cst.com
- [48] www.ansoft.com (including antenna kit)
- [49] www.antennamagus.com
- [50] www.mathworks.com
- [51] www.agilent.com
- [52] R.E. Collin, "Foundations for Microwave Engineering", McGraw-Hill, New York, 1966.
- [53] D. M. Pozar, "Microwave engineering," New York: John Wiley & Sons, 3rd edition, 2004.
- [54] J.D. Kraus, "Antennas", 2nd edition, New York, McGraw-Hill, chapter 07, 1988.
- [55] R.S. Elliott, Antenna Theory and Design, Prentice-Hall, chapter 07, 1981.
- [56] M. Makimoto, S. Yamashita, "Microwave Resonators and Filters for Wireless Communication: Theory, Design and Application, Springer-Verlag, Berlin, Heidelberg, 2001.
- [57] M. Makimoto, S. Yamashita, "Band pass filters using parallel coupled stripline stepped impedance resonators" IEEE Trans. Microw. Theory Tech., vol. 28, No. 12, pp. 1413-1417, Dec. 1980.
- [58] G. L. Matthaei, L. Young, and E. M. T. Jones, *Microwave Filters, Impedance-Matching Networks, and Coupling Structures*, Artech House, Dedham, Mass., 1980. W. tang and J. S. Hong, "Coupled stepped-impedance-resonator band stop filter", IET Microwave Antennas & Propagation, Vol. 4, Issue 9, pp. 1283-1289, 2010.
- [59] H. Liu, L. Sun and Z. Shi "Dual Bandgap Characteristics of Spurline Filters and its Circuit Modeling" Microwave and Optical Technology Letters (MOTL), vol. 49, no. 11, pp. 2805-2807, November 2007.
- [60] R. E. Pearson, "Novel Microstrip Bandstop Filter", IEEE, Electronics Letters, Vol. 13, Issue 19, pp. 561 - 562, Sept.1977.
- [61] R. N. Bates, "Design of microstrip spur-line band-stop filters", IEE Journal on Microwaves, Optics and Acoustics, Vol. 1, No.6, pp. 209 - 214, 1977.
- [62] T. H. Isaac, "Tunable plasmonic structures for terahertz frequencies", Ph.D. dissertation, University of Exeter, November 2009.
- [63] L. Sweatlock, "Plasmonics: Numerical methods and device applications," Ph.D. dissertation, California Institute of Technology, 2008.

- [64] K. Tanaka , M. Tanaka , K. Katayama , D. Miyahara, "Propagation constants of guided waves in surface plasmon polariton gap waveguides excited through an I-shaped aperture" *Science Direct, New concepts for nanophotonics and nano-electronics*, Vol.9, Issue 1, pp. 16-23, January 2008.
- [65] Z. Liu, J. M. Steele, W. Srituravanich, Y. Pikus, C. Sun, and X. Zhang, "Focusing Surface plasmons with a plasmonic lens", *Nano Letters*, Vol. 5, issue 9, pp. 1726–1729, 2005.
- [66] J. Wen, S. Romanov, and U.Peschel, "Excitation of gap plasmonic waveguides by nano antennas", *OSA / CLEO/QELS 2010*.
- [67] Z. Han, A.Y. Elezzabi and V. Van, " Experimental realization of sub-wavelength plasmonic slot waveguides and couplers on Silicon-on-Insulator", *IEEE, Lasers and Electro-Optics (CLEO) and Quantum Electronics and Laser Science Conference (QELS)*, pp. 1 - 2, May 2010.
- [68] Masafumi Fujii, Juerg Leuthold, and Wolfgang Freude, "Dispersion Relation and Loss of Subwavelength Confined Mode of Metal-Dielectric-Gap Optical Waveguides", *IEEE, Photonics technology letters*, vol. 21, no. 6, pp. 362-364, Mar 15, 2009.
- [69] Ruben Salvador, Alejandro Martinez, Carlos Garcia-Meca, Ruben Ortuno and Javier Marti, "Analysis of Hybrid Dielectric Plasmonic Waveguides", *IEEE, Journal of selected topics in quantum electronics*, vol. 14, no. 6, pp. 1496-1501, Nov/Dec 2008.

Appendix A

MATLAB Code for CSIR design of BPF

```
% BPF Using Uniform SIR structure i.e, filter composed of nos. of SIR of same
% design using strip line technology

% This M-code generates the required even and odd mode impedances along
% with the line width and length and spacing between the coupled section of
% the filter. These are verified with that from the ADS. This code is based
% on the chebyshev approximation. This code has been written from the book
% "Microwave resonators and filters for the wireless communication By
% M.Makimoto and S. Yamashita" section 4.1.4.

% Inputs to the code:
% fo_ghz: Covert the center freq into GHz and input only the numeral term and
% not the exponential.
% bw_ghz: Covert the bandwidth into GHz and input only the numeral term
% and not the exponential.
% sys_imp_ohm: Source and load impedances of the system. Normally both are
% taken to be same.
% SB_freq_ghz: Covert the stop band range (Difference between the fo_ghz and the
upper/lower stop band freq) into GHz and input only the numeral term
% and not the exponential.
% SB_attn_db: Attenuation in the stop band of the required filter in db.
% spurious_freq_multiplier: Spurious resonance frequency interms of fo_ghz.
% For ex if Spurious resonance frequency=2.5*fo_ghz then spurious_freq_multiplier is 2.5.
% PB_ripple_db: pass band ripple loss in dB.
% epsilon: relative permittivity of the substarte on which this filter
% will be simulated and fabricated
% ht_sub_mm: This code generates the physical prm for the stripline technology,therefore
this parameters should be the distance between the
% 2 gnd parallel plates in mm.

% Output:
% Odd and even mode impedances along with the length, width and spacing
% between them, for the coupled line section in the filter. This code can
% be used for the microstrip line or any other technology provided
% epsilon & ht_sub_mm should be given any commercialized value and code
% oputput-only ODD & EVEN MODE IMPEDANCES be used in ADS in order to
% get the physical prm. Other outputs of this code in that case SHOULD BE
% DISCARDED.

function [] =
sir_bpf(fo_ghz,bw_ghz,sys_imp_ohm,SB_freq_ghz,SB_attn_db,spurious_freq_multiplier,PB
_ripple_db,epsilon, ht_sub_mm)
clc;
```

```

fo_rad=2*pi*fo_ghz;
bw_rad=2*pi*bw_ghz;
las=SB_attn_db;
lar=PB_ripple_db;
fsu=fo_ghz+SB_freq_ghz; % Upper stop band cut off freq
fsl=fo_ghz-SB_freq_ghz; % Lower stop band cut off freq
bw_rel=2*(bw_ghz/fo_ghz) % Relative bandwidth of the BPF

% Transformation of Upper & Lower SB cut off freq 'fsu & fsl' of BPF to
% corresponding freqs in LPF
fsu_lpf=(fsu*fsu-fo_ghz*fo_ghz)/(fsu*bw_ghz);
fsl_lpf=(fsl*fsl-fo_ghz*fo_ghz)/(fsl*bw_ghz);

% Order calculation of the BPF
n_actual=acosh(sqrt(((10^(0.1*las))-1)/((10^(0.1*lar))-1)))/acosh(fsu_lpf);
order=ceil(n_actual)
% These many no. of SIR will be present in the filter excluding the I/O section.

% Element values for Chebyshev lowpass prototype filters
bt=log(coth(lar/17.37));
y=sinh(bt/(2*order));

for i=1:order
    a(i)=sin((2*i-1)*pi/(2*order));
    b(i)=y*y+(sin(i*pi/order))*(sin(i*pi/order));
end;

g_0=1;
g(1)=2*a(1)/y;
for i=2:order
    g(i)=4*a(i-1)*a(i)/(b(i-1)*g(i-1));
end;

if rem(order,2)==0
    g_last=(coth(bt/4))*(coth(bt/4));
else
    g_last=1;
end;

% Insertion loss @ the center freq
sum_g=0;
for i=1:order
    sum_g=g(i)+sum_g;
end;
lo_insert_db=4.434*sum_g/bw_rel

rz_actual=(tan(pi/(2*spurious_freq_multiplier)))^2;
rz=floor(rz_actual*10)/10

```

```

z2=sys_imp_ohm % Parallel coupled section is realized by z2 section
z1=(z2/rz)
theta=atan(sqrt(rz));
bo=2*theta/z2; % admittance slope parameters of the resonator

% Admittance inverter prm
j_norm_0=((bo*bw_rel/(sys_imp_ohm*g_0*g(1)))^(1/2))*sys_imp_ohm;
j_norm_last=((bo*bw_rel/(sys_imp_ohm*g_last*g(order)))^(1/2))*sys_imp_ohm;

for i=1:order-1
j_norm(i)=(bo*bw_rel/((g(i)*g(i+1)))^(1/2))*sys_imp_ohm;
end;

% Even mode impedances
zoe_0=sys_imp_ohm*((1+(j_norm_0)*csc(theta)+j_norm_0^2)/(1-(j_norm_0*cot(theta))^2))
zoe_last=sys_imp_ohm*((1+(j_norm_last)*csc(theta)+j_norm_0^2)/(1-
(j_norm_last*cot(theta))^2))

for i=1:order-1
zoe(i)=sys_imp_ohm*((1+(j_norm(i))*csc(theta)+j_norm(i)^2)/(1-(j_norm(i)*cot(theta))^2))
end;

% Odd mode impedances
zoo_0=sys_imp_ohm*((1-(j_norm_0)*csc(theta)+j_norm_0^2)/(1-(j_norm_0*cot(theta))^2))
zoo_last=sys_imp_ohm*((1-(j_norm_last)*csc(theta)+j_norm_0^2)/(1-
(j_norm_last*cot(theta))^2))

for i=1:order-1
zoo(i)=sys_imp_ohm*((1-(j_norm(i))*csc(theta)+j_norm(i)^2)/(1-(j_norm(i)*cot(theta))^2))
end;

% Line lengths of z1 & z2 sections in mm units
l1_mm=theta*300/(2*pi*sqrt(epsilon)*fo_ghz)
delta_l_mm=ht_sub_mm*log(2)/pi
% CAUTION: We cannot write simply log2 as it is an defined fun in matlab.
l2_mm=l1_mm-delta_l_mm
total_l_mm=2*(l1_mm+l2_mm)

% Width of the single
ws_z1=(30*pi/(z1*sqrt(epsilon))-(2*log(2)/pi))*ht_sub_mm
ws_z2=(30*pi/(z2*sqrt(epsilon))-(2*log(2)/pi))*ht_sub_mm

% Width of coupled lines
% Temporary variables required for width
temple_0=30*pi/(zoe_0*sqrt(epsilon))-(log(2)/pi);
temple_last=30*pi/(zoe_last*sqrt(epsilon))-(log(2)/pi);
for i=1:order-1
temple(i)=30*pi/(zoe(i)*sqrt(epsilon))-(log(2)/pi);

```

```

end;

templo_0=30*pi/(zoo_0*sqrt(epsilon))-(log(2)/pi);
templo_last=30*pi/(zoo_last*sqrt(epsilon))-(log(2)/pi);
for i=1:order-1
templo(i)=30*pi/(zoo(i)*sqrt(epsilon))-(log(2)/pi);
end;

% Width of coupled lines
wc_0=(temple_0-log(1+exp(pi*(temple_0-templo_0)))/pi)*ht_sub_mm
wc_last=(temple_last-log(1+exp(pi*(temple_last-templo_last)))/pi)*ht_sub_mm
for i=1:order-1
wc(i)=(temple(i)-log(1+exp(pi*(temple(i)-templo(i))))/pi)*ht_sub_mm
end;

% Spacing between the coupled lines
s_0=((log((1+exp(pi*(temple_0-templo_0)))/(1-exp(pi*(temple_0-
templo_0)))))/pi)*ht_sub_mm
s_last=((log((1+exp(pi*(temple_last-templo_last)))/(1-exp(pi*(temple_last-
templo_last)))))/pi)*ht_sub_mm
for i=1:order-1
s(i)=((log((1+exp(pi*(temple(i)-templo(i))))/(1-exp(pi*(temple(i)-
templo(i)))))/pi)*ht_sub_mm
end;

```

Appendix B

Dispersion diagram of SPP

```
function [] = sp_wavevector(e_high,e_static,wp,tau,ep_die)
clc
close all
f=0.001:0.001:1;
e_drude=e_high-((e_static-
e_high)*power(wp*1e15,2))./(power(2*pi*f*1e15,2)+i*tau*2*pi*f*1e30);
ksp=2*pi*f*1e15.*sqrt((e_drude*ep_die)./(e_drude+ep_die))/3e8;
ko=2*pi*f*1e15./3e8;
lamda=3e8./(f*1e15)
%*****
sp_del=1./imag(ksp);
sp_del_norm=sp_del.*f*1e15/3e8;
%*****
kz=sqrt((ep_die.*power(ko,2))-power(ksp,2));
lsp=1./abs(kz);
lsp_norm=(lamda-lsp)/lamda;
%*****
plot(real(ksp),f, 'r')
hold on
plot(imag(ksp),f, '-.b')
hold on
plot(ko,f)
grid on
figure, semilogy(f,sp_del_norm)
grid on
figure, semilogy(f,lsp_norm)
grid on
```

Appendix C

1. Drude Model for Au and Ag

The parameters reported in the following table are for several fits which we perform by non-linear least squares fit to the data [62] for Au and Ag, using the Drude model extended to a four-parameter fit by inclusion of ϵ_{high} and ϵ_{static} as fit parameters.

Table: Extended (four-parameter) Drude model permittivity of metals. Parameterizations are optimized for use at 1550 nm (infrared) or near 700 nm (visible).

Material	Model	ϵ_{high}	ϵ_{static}	ω_p [rad/s]	γ [rad/s]
Silver	IR	6.79	7.14	2.00e+16	1.00e+14
Silver	Vis	3.95	60.64	1.77e+15	1.00e+14
Gold	IR	9.25	10.74	1.03e+16	1.25e+14
Gold	Vis	10.21	47.31	2.33e+15	1.25e+14
Gold	Compromise	9.54	10.54	1.35e+16	1.25e+14

$$\epsilon_{\text{ExtendedDrude}}(\omega) = \epsilon_{\text{high}} - \frac{(\epsilon_{\text{static}} - \epsilon_{\text{high}}) \omega_p^2}{(\omega^2 + i\omega\gamma)} \quad (1)$$

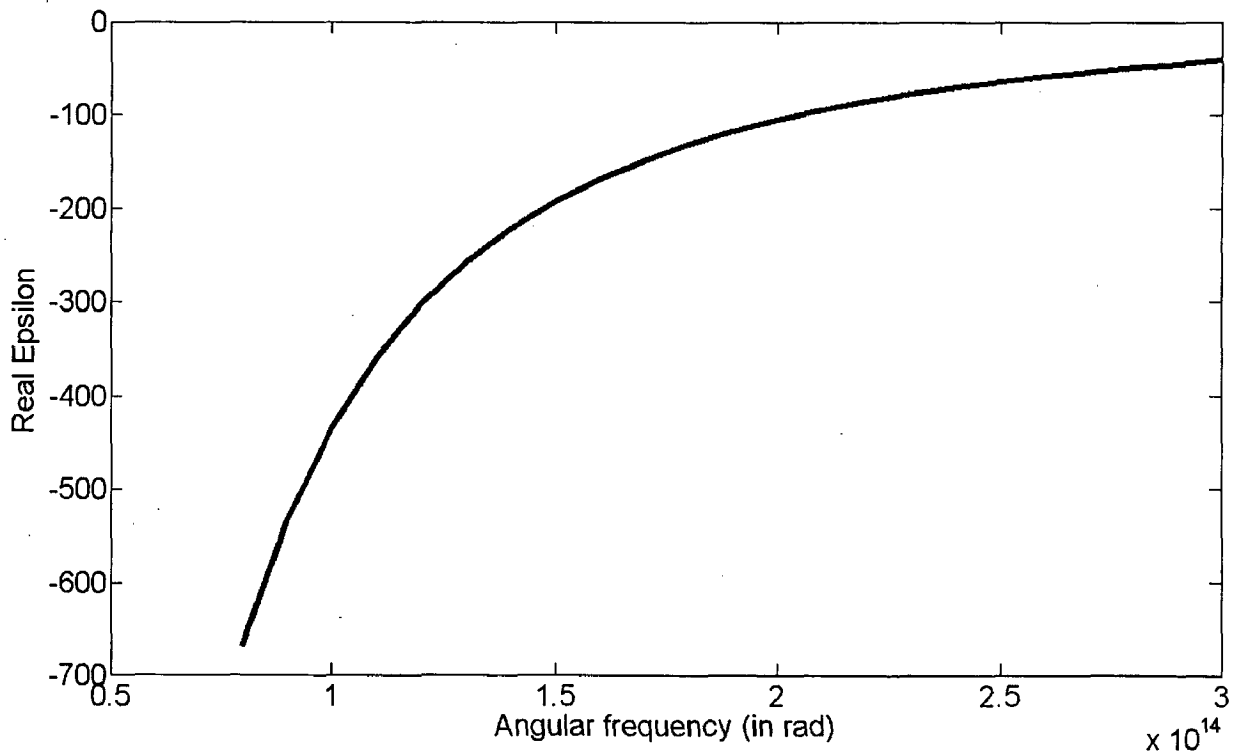


Figure C.1: Drude model real permittivity of gold (Au) using (1).

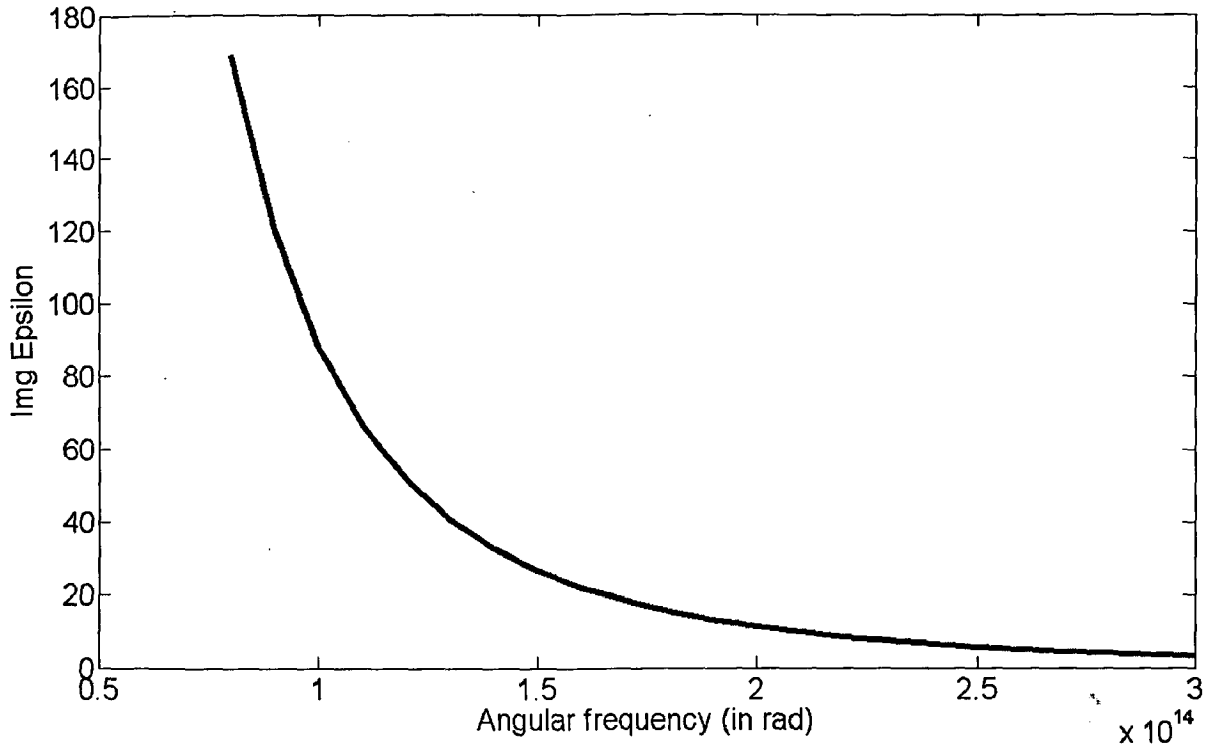


Figure C.1: Drude model imaginary permittivity of gold (Au) using (1).

2. Lorentz-Drude Model of Metals

The parameters reported in the [29] are for several fits which we perform by non-linear least squares fit to the data for metals including Au, Ag, Al, and Cu, which are all free electron metals with potential utility in plasmonics, and Cr which is sometimes used in both simulation and experiment as a specifically plasmon-suppressing media using the lorentz drude model extended to a four-parameter fit by inclusion of ϵ_{high} and ϵ_{static} as fit parameters.

$$\epsilon_{\text{ExtendedDrude}}(\omega) = 1 - (f_0 * \omega_{p,0}^2 / (\omega^2 + i\omega \gamma)) + \sum_{j=1}^{j_{\text{max}}} (f_j * \omega_{p,j}^2 / (\omega_j^2 - \omega^2 - i\omega \gamma_j))$$